

Thermophoresis in Colloidal Suspensions



Jérôme Burelbach

Department of Physics
University of Cambridge

This dissertation is submitted for the degree of
Doctor of Philosophy

Corpus Christi College

December 2017

Abstract

Title: Thermophoresis in Colloidal Suspensions

Author: Jérôme Burelbach

This dissertation examines the motion of colloids in a temperature gradient, a non-equilibrium phenomenon also known as thermophoresis. Chapter 1 gives an introduction to the existing applications and basic concepts of thermophoresis and outlines some of the experimental and theoretical challenges that serve as a motivation for this PhD project. In Chapter 2, a general theoretical description for thermophoresis is formulated using the theory of non-equilibrium thermodynamics. The colloidal flux is split up into an interfacial single-colloid contribution and a bulk contribution, followed by a determination of transport coefficients based on Onsager's reciprocal relations. It is further shown how the phenomenological expression of the thermophoretic flux can be recovered when the fluid is at steady-state. The results issuing from this description are then discussed and compared to other existing approaches, some of which are shown to neglect the hydrodynamic character of colloidal thermophoresis. Chapter 3 is dedicated to the validation of the introduced theoretical framework by means of computer simulations, using a simulation technique known as multi-particle collision dynamics. More specifically, the dependence of the thermophoretic force on different system parameters is examined and deviations from the theoretical prediction are explained by an advective distortion of interfacial fluid properties at the colloidal surface. Chapter 4 presents steady-state measurements of functionalised colloids in a temperature gradient, showing how the addition of molecular surface groups increases the experimental complexity of thermophoretic motion. The relaxation process behind this steady-state is also studied, to determine how the relaxation speed depends on the applied temperature gradient. In chapter 5, a general conclusion is drawn from the presented work and its implications are briefly discussed in relation to the current state of knowledge. Finally, the discussion is closed with an outlook on remaining challenges in understanding colloidal motion that could be the subject of future research.

Declaration

This dissertation is the result of my own work and includes nothing which is the outcome of work done in collaboration except as declared in the Preface and specified in the text. It is not substantially the same as any that I have submitted, or, is being concurrently submitted for a degree or diploma or other qualification at the University of Cambridge or any other University or similar institution except as declared in the Preface and specified in the text. I further state that no substantial part of my dissertation has already been submitted, or, is being concurrently submitted for any such degree, diploma or other qualification at the University of Cambridge or any other University or similar institution except as declared in the Preface and specified in the text. This dissertation contains fewer than 60,000 words including appendices, bibliography, footnotes, tables and equations. I note that:

The theory presented in chapter 2 has been developed in collaboration with Daan Frenkel and Ignacio Pagonabarraga and has recently been submitted for publication [14].

In chapter 3, all simulation results are my own work and are in preparation for publication [13]. The simulation technique based on multi-particle collision dynamics was first implemented in MATLAB by David B. Brückner as part of his Master degree, in a research project proposed by Daan Frenkel and Erika Eiser. The code was developed under my guidance and I re-implemented it in C++ to improve its performance. Figures 3.1, 3.6, 3.7 and 5.1 were created by David Brückner.

I performed and analysed all experiments presented in chapter 4. The colloids used in these experiments were synthesised by Yang Lan and coated by Mykolas Zupkauskas. Emma Talbot introduced me to the use of sapphire windows and silicone spacers for the fabrication of the sample cells. Figure 4.1 was kindly provided by Erika Eiser.

Jérôme Burelbach
December 2017

Acknowledgements

I have had a wonderful time doing my PhD at Cambridge and I would therefore like to give my heartfelt thanks to everyone who helped turning it into such an exciting and stimulating experience that I will never forget.

First and foremost, I would like to thank my supervisor Erika Eiser for giving me this incredible opportunity, for supporting me throughout the whole process and for having faith in my abilities and ideas. I could not have wished for a more constructive and kinder supervisor or a more welcoming research group. I will thoroughly miss all members of the Eiser group who have all been a huge support. I am also greatly indebted to the Winton Programme for the Physics of Sustainability for funding this PhD project.

Secondly, I would like to thank Daan Frenkel for all the time he has spent discussing this extremely challenging subject with me. My discussions with Daan have been the most stimulating ones during my PhD and many of my theoretical advances would not have been possible without him. I especially want to thank Daan for his persistence and patience, especially at times when our opinions on certain matters diverged.

I am also thankful to everyone who helped me during my PhD, either by direct collaboration or by providing useful advice and introducing me to experimental methods. On that note, I would like to thank David Brückner, Ignacio Pagonabarraga, Mykolas Zupkauskas, Robin Lamboll, Yang Lan, Alessio Caciagli, Darshana Joshi, Emma Talbot, Yuriy Kotar and the group of Sharon Glotzer. Special thanks also go to David Brückner, David King and Erika Eiser for proofreading this dissertation.

Last but not least, I would like to say thank you to my whole family, who have always stood behind me no matter which path I chose to take in life. None of this would have been possible without them. In particular, I would like to dedicate this work to my mother and my brother.

Contents

1	General Introduction	1
1.1	Motivation	2
1.2	Basic Definitions and Orders of Magnitude	3
1.3	To the Hot or to the Cold?	5
2	Theory	9
2.1	Non-Equilibrium Thermodynamics	10
2.2	Dynamic Length and Time Scale Separation in Colloidal Suspensions	13
2.3	Interfacial Thermophoresis and the Hydrodynamic Approach	17
2.3.1	The Interfacial Force Density	19
2.3.2	Determination of the Interfacial Driving Force: Onsager's Reciprocal Relations	22
2.4	Bulk Thermophoresis and the Microscopic Approach	27
2.5	The Thermophoretic Flux	30
2.6	Discussion and Comparison	36
2.7	Conclusion	39
3	Simulation	41
3.1	Multi-Particle Collision Dynamics	42
3.1.1	Introduction to the Simulation Technique	42
3.1.2	Implementation	45
3.2	The Simulated System	46
3.3	Forces on a Colloid inside an MPC fluid	51
3.4	Validity of ITE: the Péclet Number	56
3.5	Force Measurements	58
3.5.1	Measurement Technique	58
3.5.2	Finite Size Effects	60
3.5.3	Linearity in the Temperature Gradient	62

3.5.4	Dependence on Colloidal Radius and Interfacial Width	62
3.5.5	Influence of Potential Strength and Steepness	64
3.6	Conclusion	68
4	Experiment	69
4.1	Experimental Technique	69
4.1.1	Materials and Methods	69
4.1.2	Steady-State Measurements	71
4.2	Steady-State Measurement Results	75
4.3	Thermophoretic Relaxation to Steady-State	79
4.4	Conclusion	84
5	General Conclusion and Outlook	87
	Bibliography	97

Chapter 1

General Introduction

How do micron-sized particles move inside a liquid when subjected to a temperature gradient? Simple question, not so simple answer. This phenomenon is known as thermophoresis and can be seen as the counterpart of the Ludwig-Soret effect in fluid mixtures, which was first observed by Carl Ludwig and Charles Soret in 1856 and 1879 respectively [53, 82].

Since its discovery, thermophoresis has been studied experimentally in various systems, from charged particles in aqueous electrolyte solutions [72, 29, 41, 10, 28, 24, 70, 69] to long-chain polymers in polar or non-polar solvents [78, 96, 26, 11], revealing a large number of interesting applications. The key feature of thermophoresis is that it is governed by system-specific interactions that may be tuned such that different species of particles migrate into opposite directions. The thermophoretic effect has been found to be a promising technique for the segregation or accumulation of biomolecules [27]. Experimental evidence suggests that the thermophoretic velocity is insensitive to particle size, making it the ideal candidate for the fractionation of small particles [46], as opposed to dielectrophoresis or magnetophoresis, where the velocity scales with the square of the particle radius [71]. Moreover, thermophoresis combined with convection has been used as a focussing technique to achieve strong accumulation of DNA [11], indicating that it might have played a key role as an initiator of biochemical reactions that allowed the formation of life [5]. Thermophoresis in living matter is also of particular interest in pharmaceutical research as it is believed to contribute to diffusive processes such as membrane transport or drug delivery inside porous tissues [73]. It has further been shown to be responsible for the compositional grading in the Earth's petroleum reservoirs and the isotope fractionation in silicate melts [35, 25].

The aforementioned examples show that thermophoresis is omnipresent in our everyday life. This can be explained by the fact that no system is ever in a perfect thermodynamic equilibrium, be it deep down in the ocean, high up in the Earth's atmosphere, or somewhere inside the human body. Whereas other transport phenomena rely on the generation of electric

or magnetic fields, thermophoresis only requires a weak temperature difference across a confined geometry, making it a simple and feasible technique for particle separation.

1.1 Motivation

Despite these advances, studying thermophoresis remains a challenging task, both experimentally and theoretically. This particularly applies to colloidal suspensions, where the physical mechanisms behind thermophoresis are rooted in the mesoscopic nature of colloidal motion. Thermophoresis in colloidal suspensions is mainly driven by hydrodynamic stresses resulting from the specific interaction of the colloids with the surrounding medium. Due to the dynamic length and time separation between the colloids and the fluid molecules, the action of thermodynamic forces produces interfacial fluid flows that cannot be explained by purely thermodynamic considerations. These interactions are further influenced by a wide range of parameters [71], including intensive variables of the system such as temperature, salinity, pH and solvent expansivity, as well as single-colloid properties like shape and surface coating [90]. In experiments, it is often difficult to precisely control all these parameters, which is however necessary to make an accurate prediction for the sign and strength of the thermophoretic effect. Moreover, colloids can also be perturbed by external forces, resulting in undesirable effects such as large-scale convection or colloidal aggregation that inhibit the direct measurement of thermophoretic motion. The discrepancy between different experimental observations has further sparked a debate in recent literature about the applicability of different thermodynamic and hydrodynamic theories to colloidal thermophoresis [24, 90, 68, 76, 91, 21, 33], suggesting that a complete and consistent theoretical description is yet to be formulated.

The disagreement between authors on many theoretical and experimental aspects of thermophoresis suggests that this phenomenon requires further research. In this dissertation, I will therefore address some of these issues by carefully identifying their causes and by providing clear answers to some of the related questions, using well-founded physical arguments that specifically apply to colloidal suspensions. For this purpose, I will first give a brief introduction to the phenomenological concept and current understanding of thermophoresis based on recent findings. I will then introduce a most general theoretical framework for the motion of colloids based on Onsager's theory of Non-Equilibrium Thermodynamics, by making use of the length and time scale separation occurring in colloidal suspensions. The resulting expressions for the particle fluxes allow me to draw firm conclusions for some of the trends that are currently still under debate. In a second step, I will test the validity of my theoretical predictions by means of computer simulation, by measuring the thermophoretic force exerted

on a single colloid. Finally, I will present experimental results on thermophoresis in dilute suspensions of functionalised colloids, which suggest that molecular surface groups lead to an intricate change of thermodynamic and hydrodynamic surface properties.

1.2 Basic Definitions and Orders of Magnitude

A colloidal suspension is a mixture in which microscopically dispersed insoluble particles are suspended throughout a fluid. This fluid can be a pure liquid, a liquid mixture, or a liquid containing small soluble species of negligible size compared to the dispersed particles. In this work, the dispersed particles will be referred to as the 'colloids', whereas the pure liquid and soluble species will be called 'solvent' and 'solute', respectively.

In the absence of external forces, the diffusive transport of colloids in suspensions is quantified by a phenomenological expression for the net particle flux [71]

$$\mathbf{J} = -D\nabla c - cD_T\nabla T, \quad (1.1)$$

where D is the Fickian diffusion coefficient, c is the colloidal concentration, D_T is the thermal diffusion coefficient and ∇T is the gradient in temperature T . The first term in eq. (1.1) represents the effect of Fickian diffusion in a concentration gradient, whereas the second term accounts for the contribution to the flux induced by a temperature gradient. The thermal diffusion coefficient D_T can be interpreted as the coupling coefficient between the particle flux and the temperature gradient. By using the relation $\mathbf{J} = c\mathbf{v}$ to write each term of the flux as a product of the local concentration c and an effective drift velocity \mathbf{v} , it can be seen that thermophoretic motion can be described in terms of a drift velocity \mathbf{v}_T given by

$$\mathbf{v}_T = -D_T\nabla T. \quad (1.2)$$

As I will show in Chapter 2, it is useful to relate this drift velocity to an effective thermophoretic force \mathbf{F}_T via

$$\mathbf{F}_T = \xi\mathbf{v}_T = -\xi D_T\nabla T, \quad (1.3)$$

where ξ is the friction coefficient of a colloid. However, thermophoresis is a force-free transport phenomenon that cannot simply be interpreted as resulting from a force \mathbf{F}_T that directly acts on the colloid. Instead, the thermophoretic force \mathbf{F}_T should be thought of as the force that needs to be exerted on the colloid to cancel out its thermophoretic drift velocity.

In dilute suspensions, measuring the average drift speed of single colloids in a temperature gradient hence allows the determination of the thermal diffusion coefficient. This can in principle be achieved by single-particle tracking where the position of a colloid is recorded at a fixed frame rate [17]. However, thermophoretic drifts might not be directly measurable over short time scales as colloids also undergo random Brownian motion. In colloidal suspensions, the magnitude of D_T is usually found to lie in a rather narrow range with an upper bound given by $D_T \lesssim 10 \mu\text{m}^2\text{s}^{-1}\text{K}^{-1}$ [71]. A maximal temperature difference of around 100 K in aqueous suspensions is usually applied across samples that have a minimal width of $\sim 100 \mu\text{m}$ to avoid hydrodynamic edge effects, yielding a maximal temperature gradient of about $\sim 1 \text{K}\mu\text{m}^{-1}$. In view of eq. (1.2), typical values of thermophoretic speeds are thus rather weak, lying in the range of nanometres to micrometres per second. It is therefore instructive to compare the square of the corresponding mean displacement $\langle x_i(t) \rangle^2 = v_T^2 t^2$ to the mean square displacement resulting from the random Brownian motion of a single colloid at uniform temperature, given by $\langle x_i(t)^2 \rangle_T = 2Dt$ [30]. Thermophoretic drifts can hence only be clearly distinguished from Brownian motion when $\langle x_i(t) \rangle^2 \gg \langle x_i(t)^2 \rangle_T$, yielding the criterion

$$t_{drift} \gg \frac{2D}{v_T^2}, \quad (1.4)$$

where t_{drift} is the time scale above which the drift becomes observable. The diffusion coefficient D can be measured independently by analysing Brownian motion at uniform temperature, taking values of about $1 \mu\text{m}^2\text{s}^{-1}$ for micron-sized colloids [48]. It follows from the above criterion that colloids should be tracked over several minutes to obtain an accurate measure of the thermal diffusion coefficient. This is however not easy to achieve in denser colloidal suspensions where SPT might fail to distinguish between different trajectories. Furthermore, the gradual build-up of a concentration gradient induces a diffusive flux that may bias the direct measurement of thermophoretic drifts depending on which tracking scheme is used.

Alternatively, other experimental techniques rely on the observation of the steady-state distribution of colloids in a closed cell, which is reached when $\mathbf{J} = 0$:

$$\nabla c = -c \frac{D_T}{D} \nabla T = -c S_T \nabla T. \quad (1.5)$$

A schematic depiction of such a steady-state profile is shown in fig. 1.1. The ratio $S_T = D_T/D$ is called the Soret coefficient and is widely used to quantify the relative strength of thermophoresis to Fickian diffusion. Eq. (1.5) thus shows that the Soret coefficient S_T can be determined from the colloidal concentration profile at steady-state. The previously stated

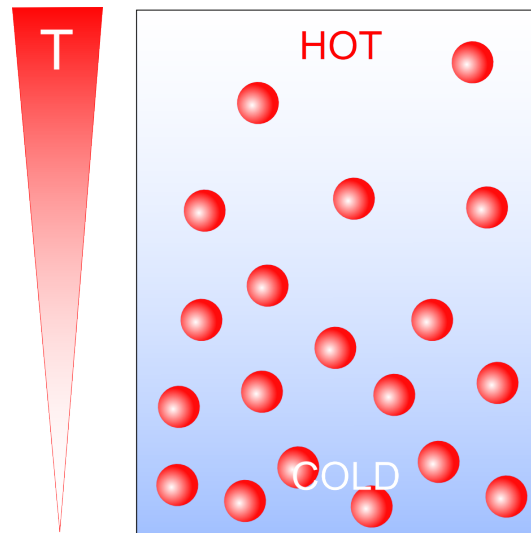


Figure 1.1: Steady-state concentration profile of colloids in a temperature gradient. The concentration gradient has been chosen to be opposite to the temperature gradient in this figure, corresponding to a thermophobic behaviour of the colloids.

values of D_T and D further imply that the magnitude of the Soret coefficient for colloids is expected to be of the order $\sim 1 \text{ K}^{-1}$. The advantage of determining S_T from the colloidal steady-state is that it does not require a direct observation of colloidal motion, meaning that it does not rely on an experimental distinction between thermophoretic motion and Fickian diffusion.

1.3 To the Hot or to the Cold?

From the definition of the Soret coefficient, it can be seen that colloids move to lower temperatures if $S_T > 0$ and to higher temperatures otherwise. In practice, predicting the sign of S_T is however not trivial at all. Experimental studies [72, 29, 41, 10, 28, 24, 70, 69, 78, 96, 26, 11] have clearly shown that thermophoresis does not follow a simple trend due to its high sensitivity to multiple system parameters. These observations strongly suggest that thermophoretic motion results from a complex interplay between different contributions induced by the temperature gradient. A comprehensive review of the most prominent theoretical models for thermophoresis has been published by Würger [90], providing quantitative explanations for some of the observed trends. However, most theories only make correct predictions for S_T in a limited range of certain parameters, suggesting that they might be incomplete or too simplified for practical purposes. The majority of these models [24, 68, 76, 91, 63] predict a

thermophobic behaviour of the colloids ($S_T > 0$), which generally agrees with experimental results [28, 24, 69, 15], but not under all experimental conditions [29, 41, 10, 77].

For instance, Piazza et al. have found that the sign of S_T changes at a specific critical temperature T_* in aqueous suspensions of functionalised polystyrene (PS) and micelles, fitting it with the empirical formula

$$S_T(T) = S_T^\infty \left[1 - \exp\left(\frac{T_* - T}{T_0}\right) \right], \quad (1.6)$$

where S_T^∞ , T_* and T_0 are system-specific parameters [41]. They noticed that the temperature dependence of S_T closely mirrors the one of the thermal expansivity of the solvent and that T_* often coincides with the temperature where the solvent density is maximal. Würger [89] has proposed that this correlation could be traced back to a close relation between thermal expansion and the thermodiffusive separation of dissociated salt in a temperature gradient. The accumulation of ions and counterions on opposite sides of the system leads to the build-up of a thermoelectric field that exerts an electric force on the charged colloids. The sign and strength of this thermoelectric field are set by the interaction between the ions and water molecules, which in turn depends on the thermal properties of water. The temperature dependence of these thermal properties is therefore transmitted to the thermoelectric field, to an extent that the field can change sign when the temperature crosses a certain critical value.

For dilute suspensions, Piazza's measurements also suggest that S_T scales linearly with particle radius R and that it increases with the square of the Debye screening length λ [10, 69]. These scalings are supported by a theoretical model for thermophoresis of a single colloid developed by Piazza and Parola [68], similar to an earlier hydrodynamic approach by Ruckenstein [76] based on the application of Debye-Hückel theory in thin boundary layers. This hydrodynamic approach has further been generalised by Würger to additionally account for thermoelectric fields and diffusio-phoretic contributions [90]. As the diffusion coefficient of a single colloid is proportional to the particle radius, this approach indeed makes D_T and v_T independent of particle size. However, for similar PS suspensions, Braun et al. have found that S_T is proportional to the square of the particle radius and that it rises linearly with the Debye length [28, 29, 24]. Their results are in turn well fitted by a single-colloid model proposed by Dhont [24, 23], whose dominant contribution is based on the minimisation of an excess free energy.

In response to the ongoing debate about these parameter dependences, in particular the one concerning the colloidal radius, one of my key aims is to derive a most general theory for colloidal thermophoresis. In the following chapter, I will therefore first give a detailed introduction to the theoretical background of thermophoresis, followed by a rigorous derivation of my theoretical results. I will then use these results to provide a

quantitative explanation for the discrepancy between these predicted scalings and show that Dhont's dominant contribution should not be appropriate for the description of colloidal thermophoresis.

Chapter 2

Theory

Although different models have already been proposed for colloidal thermophoresis, a complete theoretical description is still lacking. However, as the name suggests, the consensus is that thermophoresis is a phoretic phenomenon: the thermal motion of a colloid is mainly driven by local hydrodynamic stresses in the surrounding liquid, confined in a region close to the particle surface, often referred to as the interfacial layer.

The difficulty in describing colloidal thermophoresis with a unique theoretical model is twofold. First, colloidal masses and sizes are much bigger than those of solvent molecules, but they are small enough for the onset of Brownian motion. Secondly, thermophoresis is a non-equilibrium phenomenon [18], meaning that a formulation based on local equilibrium thermodynamics only applies when fluid advection and temperature variations can be neglected on the colloidal scale. Most theoretical models [24, 90, 68, 76] describe thermophoresis as driven by a gradient in surface tension or excess chemical potential, usually adopting either a purely hydrodynamic or thermodynamic viewpoint. In analogy to molecular thermodiffusion [92, 93], a thermodynamic approach relates the Soret coefficient to the excess enthalpy [91] or a gradient in thermodynamic potential [21], but it neglects dissipation via local fluid flows, thus restricting its validity to particles that are small compared to the interaction range. This dissipative character is correctly incorporated in a hydrodynamic approach [68, 33] that describes the fluid as a continuous medium subjected to stresses due to colloid-fluid interactions. However, hydrodynamic descriptions are usually formulated in a single-particle picture that ignores collective effects and Brownian motion.

So far, these approaches have mostly been discussed independently in literature due to a lack of common ground, although they are not mutually exclusive. This has led to a general confusion and a disagreement about which thermophoretic contributions should be considered in a thermodynamic or hydrodynamic picture. Here, I will show that the length and time scale separation in colloidal suspensions can be used to clarify this matter. I will

derive system-specific relations between different transport coefficients that describe the coupling of thermodynamic forces to the colloidal flux. My starting point is the theory of Non-Equilibrium Thermodynamics (NET), in which the temperature gradient is treated as a first order perturbation from equilibrium. NET has only received little attention in the discussion of colloidal thermophoresis, even though it provides a most general framework for thermal motion in multi-component systems.

2.1 Non-Equilibrium Thermodynamics

The theory of NET is based on the laws of thermodynamics, stating that the evolution of all components in a system is governed by its rate of entropy production. A key requirement for NET is that the system is at Local Thermodynamic Equilibrium (LTE), meaning that it can be partitioned into small volume elements, each of which may be assumed in thermodynamic equilibrium. This condition is usually satisfied for moderate temperature gradients in the absence of large-scale advection [28, 18].

Let us consider a continuous thermodynamic system at LTE, in the absence of chemical reactions. The system consists of N components, each with a corresponding number density n_k and a chemical potential μ_k . From the resulting balance equations for heat, mass and internal energy, it can be shown that the rate of entropy production σ_s inside a volume element takes the following form [18]:

$$\sigma_s = \mathbf{J}_q \nabla \frac{1}{T} + \sum_k \mathbf{J}_k \left\{ -\nabla \frac{\mu_k}{T} + \frac{1}{T} \mathbf{F}_k \right\} - \frac{1}{T} \Gamma : \nabla \mathbf{u}, \quad (2.1)$$

where Γ is the viscous stress tensor and \mathbf{u} is the centre of mass velocity of the volume element. The net particle flux of component k relative to \mathbf{u} is defined by

$$\mathbf{J}_k = n_k (\mathbf{v}_k - \mathbf{u}) \quad (2.2)$$

and satisfies $\sum_k m_k \mathbf{J}_k = 0$, where m_k is the corresponding particle mass. The total heat flux \mathbf{J}_q accounts for both heat conduction and heat diffusion and the body force \mathbf{F}_k includes external forces as well as internal forces whose range exceeds the typical LTE scale (*e.g.* thermoelectric forces). A more convenient form of eq. (2.1) can be obtained by rewriting $\nabla \frac{\mu_k}{T}$ as

$$\nabla \frac{\mu_k}{T} = \bar{H}_k \nabla \frac{1}{T} + \frac{1}{T} \nabla_T \mu_k, \quad (2.3)$$

where the subscript T indicates that the gradient is evaluated at constant temperature. The partial molar enthalpy \bar{H}_k of component k is defined as

$$\bar{H}_k = -T^2 \frac{\partial}{\partial T} \left(\frac{\mu_k}{T} \right)_{P, n_j}. \quad (2.4)$$

With eq. (2.3), the rate of entropy production can thus be expressed as

$$\sigma_s = \mathbf{J}'_q \nabla \frac{1}{T} + \frac{1}{T} \sum_k \mathbf{J}_k \{ -\nabla_T \mu_k + \mathbf{F}_k \} - \frac{1}{T} \Gamma : \nabla \mathbf{u}, \quad (2.5)$$

where the 'modified' heat flux \mathbf{J}'_q is related to \mathbf{J}_q via

$$\mathbf{J}'_q = \mathbf{J}_q - \sum_k \bar{H}_k \mathbf{J}_k. \quad (2.6)$$

Eq. (2.5) shows that entropy can be produced by two vectorial fluxes \mathbf{J}'_q and \mathbf{J}_k ; and one tensorial flux related to the fluid flow gradient $\nabla \mathbf{u}$. Onsager's theory of NET postulates linear constitutive relations between the vectorial fluxes and thermodynamic forces, of the form

$$\mathbf{J}_i = L_{iq} \nabla \frac{1}{T} + \frac{1}{T} \sum_k L_{ik} \{ -\nabla_T \mu_k + \mathbf{F}_k \}, \quad (2.7)$$

$$\mathbf{J}'_q = L_{qq} \nabla \frac{1}{T} + \frac{1}{T} \sum_k L_{qk} \{ -\nabla_T \mu_k + \mathbf{F}_k \}, \quad (2.8)$$

The scalar coefficients L are known as the Onsager transport coefficients. The flux induced by a body force \mathbf{F}_i is more commonly written as

$$\mathbf{J}_i = \frac{n_i}{\xi_i} \mathbf{F}_i, \quad (2.9)$$

where ξ_i is the friction coefficient of a particle of component i . As a result, ξ_i and L_{ii} are related by

$$L_{ii} = \frac{n_i T}{\xi_i}. \quad (2.10)$$

An important feature of Onsager's theory, also known as the reciprocal relations, is that the cross-coefficients are symmetric, so that [65, 66]

$$L_{ik} = L_{ki} \quad \text{and} \quad L_{iq} = L_{qi}. \quad (2.11)$$

It is crucial to note that these relations hold in any chosen basis of thermodynamic forces, meaning that relations similar to eqs. (2.7), (2.8) and (2.11) could also have been formulated based on the initial form of the entropy production given by eq. (2.1). Although the Curie symmetry principle forbids coupling between tensorial forces and vectorial fluxes in a homogeneous isotropic medium, a local hydrodynamic coupling between shear flows and vectorial forces can occur inside the interfacial fluid layer around a colloid.

The thermodynamic forces acting on volume element at LTE are further related via the Gibbs-Duhem equation [18]

$$dP = s dT + \sum_k n_k d\mu_k, \quad (2.12)$$

where s is the entropy density and P is the total pressure of the volume element. In the presence of thermodynamic gradients, the Gibbs-Duhem equation can hence be interpreted as a balance equation for the forces acting on a volume element. In order to write this equation in terms of the same thermodynamic forces as the Onsager fluxes, we split the differential of the chemical potential up into

$$d\mu_k = -\bar{S}_k dT + d_T \mu_k, \quad (2.13)$$

where the partial molar entropy \bar{S}_k is defined as

$$\bar{S}_k = - \left(\frac{\partial \mu_k}{\partial T} \right)_{P, n_j}. \quad (2.14)$$

As a result, the Gibbs-Duhem equation can now be rewritten as

$$dP = s' dT + \sum_k n_k d_T \mu_k, \quad (2.15)$$

where the 'modified' entropy density s' is given by

$$s' = s - \sum_k n_k \bar{S}_k. \quad (2.16)$$

It is crucial to notice the delicate difference between the entropy densities s' and s . The change from s to s' is analogous to the transition from \mathbf{J}_q to \mathbf{J}'_q , which naturally arises when the basis of thermodynamic forces is changed from $(\nabla \frac{1}{T}, \nabla \mu_k)$ to the linearly independent set $(\nabla \frac{1}{T}, \nabla_T \mu_k)$. A discussion of entropy and heat flux is therefore only meaningful if these quantities are clearly specified within the chosen basis. More generally, the modified density x' related to the density x of an extensive thermodynamic variable X can be defined as

$$x' = x - \sum_k n_k \bar{X}_k, \quad (2.17)$$

where \bar{X}_k is the corresponding partial molar property.

Finally, we note that in an N -component system, the Onsager flux given by eq. (2.7) carries a much large number of variables than the phenomenological expression given by eq. 1.1, with $(1 + N)N/2$ independent transport coefficients and $N - 1$ independent thermodynamic forces. This suggests that an introduction of specific assumptions is required to achieve a hydrodynamic description of thermophoresis in terms of a reduced number of independent variables.

2.2 Dynamic Length and Time Scale Separation in Colloidal Suspensions

Onsager's theory provides general expressions for the particle and heat fluxes, but it makes no attempt to determine the relevant transport coefficients L in specific thermodynamic systems. Here, I construct a framework that allows the formulation of system-specific relation between these coefficients for thermophoresis in colloidal suspensions. The system of interest is a closed suspension at LTE, subjected to a constant and uniform temperature gradient by keeping opposite sides of the system in contact with thermostats at different temperatures. The colloids are dispersed in a fluid that mainly consists of solvent molecules, but that can additionally contain small solutes of negligible size (*e.g.* ions). In the following, the index $i = 0$ is reserved for the solvent. The colloidal concentration and flux are denoted by c and \mathbf{J} respectively, and the index $i = 1$ is used to refer to other quantities of the colloidal component.

My theoretical framework is based on the dynamic length and time scale separation in colloidal suspensions [69, 9]. The length scale separation refers to the difference in size and concentration between the colloids and fluid particles, whereas the time scale separation occurs between the (longer) time it takes the colloid to move a distance equal to its own diameter and the (shorter) time needed for the fluid flows to establish themselves. More specifically, the framework relies on the following set of assumptions:

1. The colloids are much larger/heavier than fluid particles
2. The component densities satisfy $c \ll n_{k \neq 0,1} \ll n_0$
3. The solvent is incompressible

4. The Reynolds number of the fluid is much smaller than one ($Re \ll 1$)
5. Fluid mass diffusion dominates over fluid advection and colloidal motion (the Péclet number of the fluid is much smaller than one)

These assumptions form the basis of the hydrodynamic approach to thermophoresis. In particular, assumptions 1 and 2 allow the use of the continuum approximation. The fluid may thus be treated as a continuous medium and the incompressibility of the solvent leads to a rapid momentum relaxation in the system. Further, the presence of a large bulk reservoir of pure fluid allows the introduction of an effective bulk fluid pressure P_s^b , which can be defined via eq. (2.15) as the pressure resulting from thermodynamic forces inside a volume element of pure fluid (hereafter referred to as fluid element):

$$dP_s^b = s_s'^b dT + \sum_{k \neq 1} n_k^b d\mu_k, \quad (2.18)$$

where $s_s'^b$ is the modified entropy density of the pure bulk fluid and n_k^b is the corresponding bulk concentration of fluid component k . From eq. (2.18), the osmotic pressure Π of the colloids can be unambiguously defined as the difference between the total pressure and the bulk fluid pressure inside the volume element:

$$\Pi = P - P_s^b \quad (2.19)$$

For visual aid, the components and corresponding pressures inside a volume element at LTE are displayed in fig. 2.1.

For colloids, a departure from the ideal state occurs due to specific interactions with the surrounding components. The colloidal chemical potential can then more generally be written as $\mu_1 = \mu_{id} + \mu_{exc}$, where μ_{id} is the ideal chemical potential. The excess chemical potential μ_{exc} accounts for a specific colloid-fluid interaction, denoted by μ_{cs} ; and for a collective contribution μ_{cc} due to excluded volume effects or specific pair-interactions between colloids. According to assumptions 1 and 5, the fluid responds to these interactions with a rapid relaxation to a local equilibrium distribution around the colloids that remains unperturbed by colloidal motion or advection. At uniform temperature, this allows the formulation of a 'reduced' description [85, 34], in which the colloid-fluid interaction μ_{cs} is treated as a local interfacial layer around the colloid, separated out from the bulk. Inside the interfacial layer, the local thermodynamic properties of the fluid differ from those of the bulk fluid, which in turn barely feels the presence of the colloids. As the introduction of a colloid necessarily leads to the build-up of an interfacial layer, μ_{cs} is equal to the surface energy of the created interface:

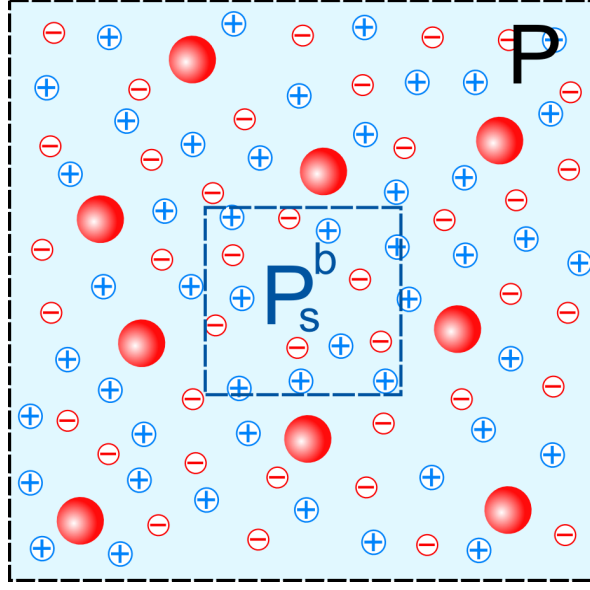


Figure 2.1: A volume element of the colloidal suspension at LTE, containing colloids (red spheres) and fluid. The fluid is made of solvent (continuous light blue background) and solutes (f. ex. ions and counterions). The dashed blue square shows an element of pure fluid with a corresponding bulk fluid pressure P_s^b . The interfacial layers around the colloids are not shown here.

$$\mu_{cs} = A_c \left(\frac{\partial G}{\partial A} \right)_{P,T,N_{k \neq 1}} = A_c \gamma_{cs}, \quad (2.20)$$

where G is the Gibbs free energy, γ_{cs} is the interfacial tension and A_c is the constant surface area of a colloid. The change in surface energy can further be related to interfacial excess properties of the fluid via the Gibbs adsorption equation [61]

$$-d\mu_{cs} = -A_c d\gamma_{cs} = S_\phi dT + \sum_{k \neq 1} N_k^\phi d_T \mu_k, \quad (2.21)$$

where N_k^ϕ is the excess number of fluid particles of component k and S_ϕ is the interfacial excess entropy. The Gibbs adsorption equation shows that S_ϕ and N_k^ϕ can be interpreted as the partial molar properties of the colloidal component if the interfacial chemical potential μ_{cs} changes in response to the thermodynamic forces dT and $d_T \mu_k$. In addition, a collective contribution μ_{cc} may arise from the interaction between overlapping layers. From this description, it follows that the colloidal chemical potential can be expressed as a sum of two separate terms:

$$\mu_1 = \mu_{cs} + \mu_c, \quad (2.22)$$

where $\mu_c = \mu_{id} + \mu_{cc}$ is the 'bulk' chemical potential of the colloidal component, accounting for colloidal pair-interactions and for the ideal part of the chemical potential. To make progress in the description of thermophoresis, we shall extend this superposition principle to the colloidal flux, by writing

$$\mathbf{J} = \mathbf{J}_{cs} + \mathbf{J}_c. \quad (2.23)$$

Due to the hydrodynamic character of the Onsager transport coefficients, the separation into an interfacial single-colloid contribution \mathbf{J}_{cs} and a bulk contribution \mathbf{J}_c is only useful if the fluid flows induced by these fluxes can also be treated as decoupled from each other. This indeed applies to fluids at low Reynolds number since the Navier-Stokes equation is linear when $Re \ll 1$, allowing the use of the superposition principle of fluid flows. By separating out the direct contribution from the colloidal chemical potential ($i = 1$) in eq. (2.7), \mathbf{J}_c and \mathbf{J}_{cs} can now be written as two decoupled Onsager fluxes, respectively given by

$$\mathbf{J}_c = L_{1q}^c \nabla \frac{1}{T} - \frac{L_{11}}{T} \nabla_T \mu_c + \frac{1}{T} \sum_{k \neq 1} L_{1k}^c \{-\nabla_T \mu_k + \mathbf{F}_k\} \quad (2.24)$$

and

$$\mathbf{J}_{cs} = L_{1q}^{cs} \nabla \frac{1}{T} + \frac{L_{11}}{T} (-\nabla_T \mu_{cs} + \mathbf{F}_1) + \frac{1}{T} \sum_{k \neq 1} L_{1k}^{cs} \{-\nabla_T \mu_k + \mathbf{F}_k\}, \quad (2.25)$$

where each term in $L_{1q} = L_{1q}^{cs} + L_{1q}^c$ and $L_{1k} = L_{1k}^{cs} + L_{1k}^c$ separately satisfies Onsager's reciprocal relation.

In general, the body force \mathbf{F}_k on component k may consist of an external body force $\mathbf{F}_{k,\text{ext}}$, such as gravity, and an internal body force $\mathbf{F}_{k,\text{int}}$, resulting from a thermoelectric field inside the system. As this work is meant to focus on the motion of colloids in a temperature gradient, I will ignore external forces in the following theoretical considerations. However, external forces can easily be included by noticing that they couple to the colloidal flux via the same Onsager coefficients L_{1k} as the corresponding chemical potential gradients $\nabla_T \mu_k$ and thermoelectric forces $\mathbf{F}_{k,\text{int}}$. By setting $\mathbf{F}_{k,\text{ext}} = 0$ and $\mathbf{F}_k = \mathbf{F}_{k,\text{int}}$, the condition of charge neutrality implies that equal and opposite body forces are exerted on the colloid and its interfacial layer, giving

$$\mathbf{F}_1 + \sum_{k \neq 1} N_k^\phi \mathbf{F}_k = 0. \quad (2.26)$$

Combining this result with eq. (2.21) at uniform temperature, we obtain the relation

$$-\nabla_T \mu_{cs} + \mathbf{F}_1 = - \sum_{k \neq 1} N_k^\phi \{ -\nabla_T \mu_k + \mathbf{F}_k \}. \quad (2.27)$$

For the treatment of interfacial thermophoresis, it is useful to eliminate the term $-\nabla_T \mu_{cs} + \mathbf{F}_1$ with eq. (2.27), allowing us to express eq. (2.25) in the alternative form

$$\mathbf{J}_{cs} = \frac{L_{11}}{T} \left(-Q_{1q}^{cs} \frac{\nabla T}{T} + \sum_{k \neq 1} N_{1k}^{cs} \{ -\nabla_T \mu_k + \mathbf{F}_k \} \right), \quad (2.28)$$

where the interfacial transport coefficients Q_{1q}^{cs} and N_{1k}^{cs} are given by

$$Q_{1q}^{cs} = L_{1q}^{cs}/L_{11}, \quad (2.29)$$

$$N_{1k}^{cs} = L_{1k}^{cs}/L_{11} - N_k^\phi. \quad (2.30)$$

A carefully chosen set of assumptions that specifically applies to colloidal suspensions has thus lead us to a framework in which the separate evaluation of \mathbf{J}_{cs} and \mathbf{J}_c is well justified. As a result, the interfacial contribution \mathbf{J}_{cs} can now be discussed within a hydrodynamic single-colloid picture.

2.3 Interfacial Thermophoresis and the Hydrodynamic Approach

The hydrodynamic single-colloid picture is concerned with the interfacial stresses that thermodynamic bulk gradients produce inside the fluid around a single colloid. It is well known that a thermodynamic gradient across an interfacial layer gives rise to a fluid flow in one direction and a corresponding phoretic drift of the colloid in the opposite direction [4] (Fig. 2.2). In the absence of a temperature gradient, a radially symmetric distribution of fluid around the colloid is maintained by a local balance between a body force density \mathbf{f}_s and a gradient in fluid pressure P_s , such that $\mathbf{f}_s - \nabla P_s = 0$. A temperature gradient then breaks this balance and sets the colloid and fluid into motion. A steady-state drift velocity \mathbf{v} is reached when the total force on the colloid is zero and the resulting colloidal flux can then be written as

$$\mathbf{J}_{cs} = c\mathbf{v} = \frac{c}{\xi} \mathbf{F}_{cs}, \quad (2.31)$$

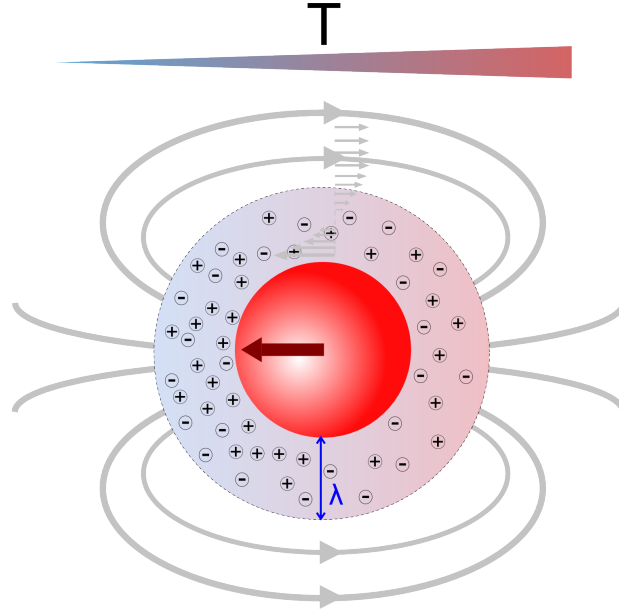


Figure 2.2: Schematic depiction of hydrodynamic stresses caused by a temperature gradient inside an interfacial (electric double) layer around a charged colloid. The gradient in excess pressure induces an interfacial fluid flow close to the colloidal surface (grey lines). In response, the colloid moves in the opposite direction (dark red arrow).

where ξ is the friction coefficient of the colloid. In view of eq. (2.28), the interfacial driving force \mathbf{F}_{cs} is given by

$$\mathbf{F}_{cs} = -Q_{1q}^{cs} \frac{\nabla T}{T} + \sum_{k \neq 1} N_{1k}^{cs} \{-\nabla_T \mu_k + \mathbf{F}_k\}. \quad (2.32)$$

Although the 'interfacial heat of transport' Q_{1q}^{cs} has commonly been identified as the driving force behind interfacial thermophoresis, the contribution related to N_{1k}^{cs} has often been overlooked. This is rather surprising, as it is the latter contribution that can give rise to the well-known effect of diffusiophoresis at uniform temperature. Based on Onsager's reciprocal relations, I will show that Q_{1q}^{cs} and N_{1k}^{cs} can respectively be determined from the interfacial transport of heat and fluid particles that arises when a stationary colloid is subjected to a uniform bulk flow in a fluid kept at constant temperature and chemical potential. The corresponding interfacial excess densities of the fluid must however be defined carefully before these transport coefficients can be computed. For this purpose, I first consider the momentum balance equation of the fluid, which is governed by the Navier-Stokes equation

$$\vec{\mathcal{F}} + \eta \nabla^2 \mathbf{u}_s = 0, \quad (2.33)$$

where $\vec{\mathcal{F}} = \mathbf{f}_s - \nabla P_s$ is the net force density acting on the fluid element, \mathbf{u}_s is the local centre of mass velocity of the fluid element and η is the fluid viscosity. The inertia term has been neglected in eq. (2.33) due to the assumption of small Reynolds number. Here, I first derive a general expression for the interfacial force density $\vec{\mathcal{F}}_\phi$ that drives phoretic motion. In recent literature [90, 68, 23], different expressions have only been given in the case where the excess fluid inside the layer is described by Poisson-Boltzmann theory, suggesting that a general expression of $\vec{\mathcal{F}}_\phi$ for non-ideal fluids is still lacking.

2.3.1 The Interfacial Force Density

Let us consider a stationary colloid whose surface is in contact with a large bulk reservoir of fluid made of solvent molecules and small solutes. The solvent is pictured as an incompressible, polarisable medium. I denote a fluid property x with an index b to refer to its value in the bulk and write it as $x(\mathbf{r})$ to refer to its local value at a position \mathbf{r} from the colloidal centre. The interfacial layer around the colloid results from a specific interaction between the colloid and fluid component k , characterised by a potential $\phi_k(\mathbf{r})$ that tends to zero in the bulk. Interfacial excess densities will therefore be denoted by an index ϕ . Close to the colloidal surface, a fluid component k can hence be subjected to a local conservative body force $-\nabla_T \phi_k(\mathbf{r})$ and an internal body force \mathbf{F}_k induced by the temperature gradient in the bulk. The body force density in a local fluid element is thus given by

$$\mathbf{f}_s(\mathbf{r}) = - \sum_{k \neq 1} n_k(\mathbf{r}) (\nabla_T \phi_k(\mathbf{r}) - \mathbf{F}_k) + \mathbf{p}(\mathbf{r}) \nabla \mathbf{E}(\mathbf{r}), \quad (2.34)$$

where the last term accounts for the electric force due to the solvent polarisation $\mathbf{p}(\mathbf{r})$ in the non-uniform electric field $\mathbf{E}(\mathbf{r})$ of the colloid. Assuming that the fluid element is at LTE, the Gibbs-Duhem equation can further be used to relate the gradient in fluid pressure $P_s(\mathbf{r})$ across the element to the local thermodynamic gradients [18]:

$$\nabla P_s(\mathbf{r}) = s'_s(\mathbf{r}) \nabla T + \sum_{k \neq 1} n_k(\mathbf{r}) \nabla_T \mu_k(\mathbf{r}) + \mathbf{p}(\mathbf{r}) \nabla \mathbf{E}(\mathbf{r}), \quad (2.35)$$

where

$$s'_s(\mathbf{r}) = s_s(\mathbf{r}) - \sum_{k \neq 1} n_k(\mathbf{r}) \bar{s}_k. \quad (2.36)$$

In view of eqs. (2.34) and (2.35), it should be noted that the potential $\phi_k(\mathbf{r})$ created by the colloid is treated as an external field at this stage, so that the fluid chemical potentials $\mu_k(\mathbf{r})$

only account for internal interactions between fluid components. The local force density $\vec{\mathcal{F}}(\mathbf{r})$ on a fluid element thus equals

$$\vec{\mathcal{F}}(\mathbf{r}) = \mathbf{f}_s(\mathbf{r}) - \nabla P_s(\mathbf{r}) = -s'_s(\mathbf{r})\nabla T - \sum_{k \neq 1} n_k(\mathbf{r}) \{ \nabla_T (\mu_k(\mathbf{r}) + \phi_k(\mathbf{r})) - \mathbf{F}_k \}. \quad (2.37)$$

Due to the gradient in $\phi_k(\mathbf{r})$, the force density given by eq. (2.37) cannot yet be related back to the thermodynamic forces that appear in eq. (2.28). However, this problem can be solved by extending the condition of thermodynamic equilibrium to the scale of the entire interfacial layer. In a homogeneous system at uniform temperature, the radially symmetric equilibrium structure of the interfacial layer around a colloid is determined by the condition of zero force density

$$\vec{\mathcal{F}}(r) = - \sum_{k \neq 1} n_k(r) \nabla_T (\mu_k(r) + \phi_k(r)) = 0, \quad (2.38)$$

which is satisfied if $\nabla_T (\mu_k(r) + \phi_k(r)) = 0$. Integration from the colloidal surface into the bulk of the suspension then directly yields the chemical equilibrium condition

$$\mu_k(r) + \phi_k(r) = \mu_k^b, \quad (2.39)$$

where μ_k^b is the chemical potential of component k in the bulk of the suspension. In a non-equilibrium system, μ_k^b can more generally be understood as the value of the chemical potential far away from the colloidal surface, along the isotherm of the considered fluid element. Eq. (2.39) is supposed to remain valid if the interfacial layer is at thermodynamic equilibrium. This crucial assumption, which shall henceforth be referred to as Interfacial Thermodynamic Equilibrium (ITE), allows us to redefine the fluid chemical potential μ_k by including the potential ϕ_k as an internal interaction in the fluid equation of state:

$$\mu_k \equiv \mu_k(r) + \phi_k(r) = \mu_k^b, \quad (2.40)$$

so that the 'bulk' index b of μ_k can simply be omitted. As $(\partial \phi_k / \partial T)_{P, n_j} = 0$, the partial molar entropy \bar{S}_k remains unaffected by this redefinition, but the potential $\phi_k(r)$ now directly contributes to the local fluid enthalpy density $h_s(r)$. From the standard thermodynamic relations $Ts_s = h_s - \sum_{k \neq 1} n_k \mu_k$ and $T\bar{S}_k = \bar{H}_k - \mu_k$, it is then easily verified that an enthalpy-entropy compensation of the form

$$Ts'_s(r) = h'_s(r) \quad (2.41)$$

holds between the modified densities $s'_s(r)$ and $h'_s(r)$. With eq. (2.40), the force density given by eq. (2.37) can now be written as

$$\vec{\mathcal{F}}(r) = -h'_s(r) \frac{\nabla T}{T} + \sum_{k \neq 1} n_k(r) \{-\nabla_T \mu_k + \mathbf{F}_k\}. \quad (2.42)$$

where $h'_s(r)$ and $n_k(r)$ only depend on the radial distance r from the colloidal centre. In the absence of an interfacial layer, the same fluid element will be subjected to a bulk force density given by

$$\vec{\mathcal{F}}_b = -h_s^{lb} \frac{\nabla T}{T} + \sum_{k \neq 1} n_k^b \{-\nabla_T \mu_k + \mathbf{F}_k\}. \quad (2.43)$$

As interfacial thermophoresis is only concerned with the motion induced by the part of $\vec{\mathcal{F}}$ that directly stems from the specific colloid-fluid interaction, we have to subtract this bulk force density from eq. (2.42), giving

$$\vec{\mathcal{F}}_\phi(r) = \vec{\mathcal{F}}(r) - \vec{\mathcal{F}}_b = -q_\phi(r) \frac{\nabla T}{T} + \sum_{k \neq 1} n_k^\phi(r) \{-\nabla_T \mu_k + \mathbf{F}_k\} \quad (2.44)$$

with

$$q_\phi(r) = h_\phi(r) = h'_s(r) - h_s^{lb}, \quad (2.45)$$

$$n_k^\phi(r) = n_k(r) - n_k^b, \quad (2.46)$$

where $q_\phi(r)$ is the interfacial heat density and $n_k^\phi(r)$ is the interfacial excess (number) density of fluid component k . As I will show more explicitly in the section on bulk thermophoresis, a non-zero value of $\vec{\mathcal{F}}_b$ is an indicator of collective effects due to the presence of multiple colloids inside the system. For a single colloid in an infinitely large bulk fluid, the fluid must be force-free in the absence of external forces, such that $\vec{\mathcal{F}}_b = 0$, implying that $h_s^{lb} = 0$. Eq. (2.45) reduces to $q_\phi(r) = h'_s(r)$ in this case, meaning that the interfacial heat density is simply equal to the modified enthalpy density of the fluid.

With eq. (2.44), I have derived a most general expression for the interfacial force density resulting from the specific colloid-fluid interaction. This result specifically relies on the assumption of ITE and shows that thermodynamic forces couple to the interfacial excess densities of the fluid, which are now unambiguously defined by eqs. (2.45) and (2.46). Finally, it must be noted that eq. (2.44) and (2.45) ignore heat conduction through the colloid. Internal heat flows through the colloid must however be treated with care as they modify the local temperature profile around the colloid if its thermal conductivity σ_c differs

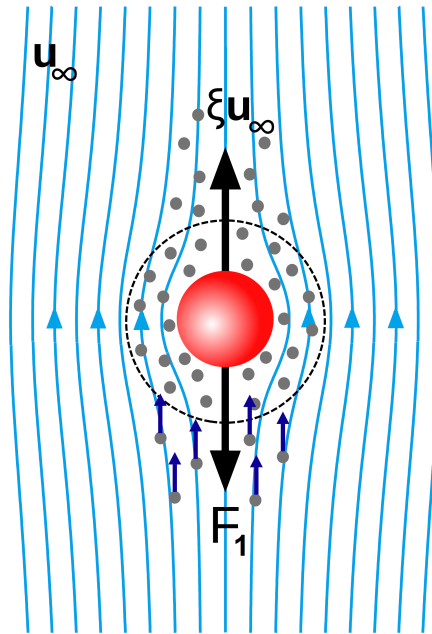


Figure 2.3: As the fluid streams past the stationary colloid (light blue lines), it carries heat/fluid particles out of the interfacial layer. The thermodynamic equilibrium inside the layer is then restored by an instantaneous absorption of heat/fluid particles from the bulk (dark blue arrows). Overall, this combined process leads to a flux of heat/fluid particles in the bulk. The depicted fluid flows are based on [7].

from the conductivity σ_s of the fluid [90]. To preserve the condition of ITE, the resulting local temperature gradient must then be assumed to be reasonably weak and approximately uniform over the layer. This issue will be given further attention in my second chapter on the simulation of thermophoresis.

2.3.2 Determination of the Interfacial Driving Force: Onsager's Reciprocal Relations

Based on momentum conservation, the thermophoretic drift is usually directly determined from eq. (2.33) using the expression of the interfacial force density of the fluid inside a temperature gradient. However, these hydrodynamic arguments have so far only been successfully applied in the limiting cases where the interaction range is either very small or very large compared to the colloidal size [33, 62]. Here, I propose an alternative approach based on Onsager's reciprocal relations that applies to any case, irrespective of the interaction range. The strength of these relations, as given by eq. (2.11), lies in the prediction that the colloidal flux couples to gradients in temperature and fluid chemical potential in the same way as heat and fluid fluxes couple to an external force on the colloid. Instead of

using momentum conservation arguments in a force-free system subjected to thermodynamic gradients, these transport coefficients can hence be determined by computing the heat and fluid fluxes in the absence of thermodynamic gradients when an external force is applied to the colloid.

To obtain a general hydrodynamic expression for Q_{1q}^{cs} or N_{1k}^{cs} , we consider a single colloid of radius R inside an infinitely large fluid at uniform temperature and chemical potential. The fluid is moving at a uniform flow velocity $\mathbf{u}_\infty = u_\infty \hat{\mathbf{y}}$ in the bulk and the colloid is kept at rest by an applied force $\mathbf{F}_1 = -\xi \mathbf{u}_\infty$. The fluid streams through the interfacial layer and carries an excess of heat and fluid particles into the bulk. As the interfacial layer is assumed to remain in a thermodynamic equilibrium around the colloid, the excess carried out of the layer is balanced by an absorption of an equal amount of heat/fluid particles from the bulk fluid. This interfacial balance, which is represented in fig. 2.3, results in the following heat and particle fluxes:

$$\mathbf{J}'_{q,V} = \int_R^\infty q_\phi(r) \mathbf{u}_s(\mathbf{r}) dV \quad (2.47)$$

$$\mathbf{J}_{k,V} = \int_R^\infty n_k^\phi(r) (\mathbf{u}_s(\mathbf{r}) - \mathbf{u}_\infty) dV, \quad (2.48)$$

where \mathbf{u}_s is the fluid flow velocity. In view of eq. (2.2), particle fluxes are computed with respect to the bulk velocity \mathbf{u}_∞ , which has therefore been subtracted from the flow velocity in eq. (2.48). It is worth noting that eqs. (2.47) and (2.48) are the integrated heat and particle fluxes, meaning that the fluxes have been integrated over the volume V of the system. Based on Onsager's reciprocal relations (2.11), these fluxes can equivalently be expressed as

$$\mathbf{J}'_{q,V} = V \frac{L_{q1}^{cs}}{T} \mathbf{F}_1 = -\frac{L_{q1}^{cs}}{L_{11}} \mathbf{u}_\infty = -\frac{L_{1q}^{cs}}{L_{11}} \mathbf{u}_\infty = -Q_{1q}^{cs} \mathbf{u}_\infty, \quad (2.49)$$

$$\mathbf{J}_{k,V} = V \frac{L_{k1}^{cs}}{T} \mathbf{F}_1 = -\frac{L_{k1}^{cs}}{L_{11}} \mathbf{u}_\infty = -\frac{L_{1k}^{cs}}{L_{11}} \mathbf{u}_\infty = -\left(N_{1k}^{cs} + N_k^\phi\right) \mathbf{u}_\infty. \quad (2.50)$$

More generally, let us denote the interfacial excess densities $q_\phi(r)$ and $n_k^\phi(r)$ by $x_\phi(r)$ and the corresponding interfacial transport coefficients Q_{1q}^{cs} and N_{1k}^{cs} by X_{cs} . By respectively combining eqs. (2.47) and (2.48) with eqs. (2.49) and (2.50), we obtain

$$X_{cs} \mathbf{u}_\infty = -\int_R^\infty x_\phi(r) \mathbf{u}_s(\mathbf{r}) dV. \quad (2.51)$$

Due to the circular symmetry around the direction $\hat{\mathbf{y}}$ of the bulk flow, only the y -component of \mathbf{u}_s contributes to the volume integral. Furthermore, as the interfacial excess density $x_\phi(r)$ only depends on radial distance, the angular integration in eq. (2.51) can be carried out separately over \mathbf{u}_s , so that we can write

$$X_{cs}u_\infty = - \int_R^\infty x_\phi(r) \langle \mathbf{u}_s(\mathbf{r}) \hat{\mathbf{y}} \rangle 4\pi r^2 dr, \quad (2.52)$$

with an orientational average $\langle \mathbf{u}_s(\mathbf{r}) \hat{\mathbf{y}} \rangle$ defined by

$$\langle \mathbf{u}_s(\mathbf{r}) \hat{\mathbf{y}} \rangle = \frac{1}{2} \int_0^\pi u_y(r, \theta) \sin \theta d\theta, \quad (2.53)$$

where $u_y(r, \theta)$ is the y -component of \mathbf{u}_s and θ is the angle with respect the bulk flow direction ($\mathbf{r}\hat{\mathbf{y}} = \cos \theta$). The solution for the fluid flow velocity \mathbf{u}_s around a spherical particle is known for both stick and slip boundary conditions [6, 52]. In the spherical basis $(\hat{\mathbf{r}}, \hat{\boldsymbol{\theta}})$, the coordinates of \mathbf{u}_s are given by

$$u_r = u_\infty \cos \theta \left[1 - 2 \left(\frac{3}{4} - a \right) \frac{R}{r} + 2 \left(\frac{1}{4} - a \right) \left(\frac{R}{r} \right)^3 \right] \quad (2.54)$$

$$u_\theta = -u_\infty \sin \theta \left[1 - \left(\frac{3}{4} - a \right) \frac{R}{r} - \left(\frac{1}{4} - a \right) \left(\frac{R}{r} \right)^3 \right], \quad (2.55)$$

where the parameter a takes the value $a = 0$ for stick and $a = 1/4$ for slip. The orientational average can thus be evaluated in a straightforward manner (see appendix A), yielding

$$X_{cs} = - \int_R^\infty x_\phi(r) \left(1 - b \frac{R}{r} \right) 4\pi r^2 dr, \quad (2.56)$$

where the parameter b takes the value $b = 1$ for stick and $b = 2/3$ for slip.

With eq. (2.56), I have derived a general hydrodynamic form for the interfacial transport coefficient X_{cs} based on Onsager's reciprocal relations. Eq. (2.56) can now be used to compute the interfacial driving force \mathbf{F}_{cs} as defined by eq. (2.32). As the thermodynamic bulk gradients ∇T and $\nabla_T \mu_k$ are uniform over the layer, the hydrodynamic form can be directly applied to the interfacial force density $\vec{\mathcal{F}}_\phi(r)$, giving

$$\mathbf{F}_{cs} = - \int_R^\infty \vec{\mathcal{F}}_\phi(r) \left(1 - b \frac{R}{r} \right) 4\pi r^2 dr, \quad (2.57)$$

which, by changing variables, can alternatively be expressed as

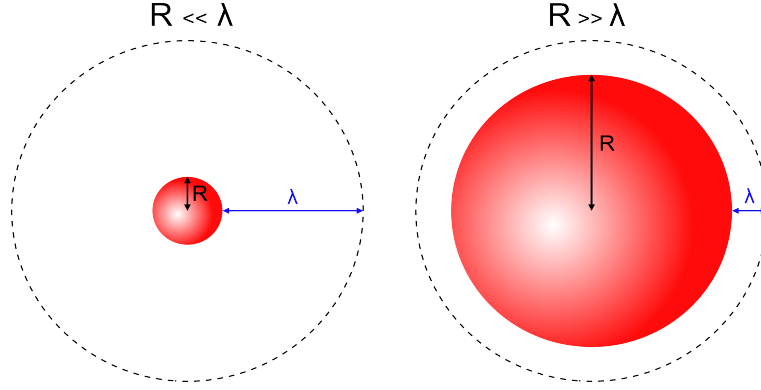


Figure 2.4: Schematic depiction of the Hückel limit ($R \ll \lambda$) and the boundary layer approximation ($R \gg \lambda$)

$$\mathbf{F}_{CS} = -4\pi \int_0^\infty \vec{\mathcal{F}}_\phi(z) [z^2 + (2-b)Rz + (1-b)R^2] dz. \quad (2.58)$$

where $z = r - R$ is the radial distance from the colloidal surface. For the following considerations, it is convenient to introduce a characteristic length scale λ that defines the 'thickness' of the interfacial layer. Of particular interest are the limiting cases of 'large layers' ($R \ll \lambda$) and 'thin layers' ($R \gg \lambda$), which are respectively known as the Hückel limit [62] and the boundary layer approximation [90] (fig. 2.4).

In the Hückel limit, the particle size is negligible ($R/r \rightarrow 0$) and eq. (2.57) reduces to a volume integral over the layer. Further, heat conduction through the colloid can be ignored, so that the identity $q_\phi = h_\phi$ remains valid. We obtain

$$\mathbf{F}_{CS} = - \int_R^\infty \vec{\mathcal{F}}_\phi(r) 4\pi r^2 dr = H_\phi \frac{\nabla T}{T} - \sum_{k \neq 1} N_k^\phi \{-\nabla_T \mu_k + \mathbf{F}_k\}, \quad R \ll \lambda, \quad (2.59)$$

where N_k^ϕ is the interfacial excess number of fluid component k and H_ϕ is the interfacial excess enthalpy. In the Hückel limit, \mathbf{F}_{CS} is independent of the boundary condition at the colloidal surface and the interfacial Onsager coefficients, as defined by eqs. (2.29) and (2.30), reduce to

$$L_{1q}^{CS} = -H_\phi L_{11}, \quad (2.60)$$

$$L_{1k}^{CS} = 0. \quad (2.61)$$

Noting that $H_\phi = TS_\phi$, eqs. (2.21) and (2.27) can further be used to rewrite eq. (2.59) in the alternative form

$$\mathbf{F}_{cs} = -\nabla\mu_{cs} + \mathbf{F}_1, \quad R \ll \lambda. \quad (2.62)$$

This result shows that the Hückel limit corresponds to an effective 'thermodynamic' treatment of colloidal motion, driven by a gradient in surface energy $-\nabla\mu_{cs}$.

As the Hückel limit is restricted to particles that are small compared to the layer thickness, it is not expected to hold for colloidal thermophoresis. Colloids usually have diameters that largely exceed the interaction range and should therefore be considered in the boundary layer approximation $R \gg \lambda$, where the heat flux through the colloid must also be taken into account. In this limit, the interfacial heat density is therefore no longer equal to the interfacial enthalpy density h_ϕ but can be related to h_ϕ via $q_\phi = Ch_\phi$ where the factor $C = 3/(2 + \sigma_c/\sigma_s)$ is set by the ratio between σ_c and σ_s [90, 37]. To first order in $z/R \ll 1$, eq. (2.58) reduces to:

$$\begin{aligned} \mathbf{F}_{cs} &= -4\pi \int_0^\infty \vec{\mathcal{F}}_\phi(z) [(2-b)Rz + (1-b)R^2] dz, \quad R \gg \lambda \\ &= \begin{cases} -4\pi R \int_0^\infty z \vec{\mathcal{F}}_\phi(z) dz & \text{for stick} \\ -\frac{1}{3} \times 4\pi R^2 \int_0^\infty \vec{\mathcal{F}}_\phi(z) dz - \frac{4}{3} \times 4\pi R \int_0^\infty z \vec{\mathcal{F}}_\phi(z) dz & \text{for slip,} \end{cases} \end{aligned} \quad (2.63)$$

where it should again be noted that $-4\pi R^2 \int \vec{\mathcal{F}}_\phi(z) dz = -\nabla\mu_{cs} + \mathbf{F}_1$.

Interestingly, the expression for a stick boundary in eq. (2.63) coincides with the expression first derived by Derjaguin, who based his derivation on Onsager reciprocity by considering isothermal fluid flow through a porous medium [20, 4]. An important feature of the boundary layer approximation is that, although thermophoretic motion is still *induced* by a gradient in surface energy μ_{cs} , the force \mathbf{F}_{cs} that *drives* thermophoresis can no longer just be written as $-\nabla\mu_{cs} + \mathbf{F}_1$. In view of eqs. (2.29) and (2.30), we notice that this hydrodynamic aspect of colloidal thermophoresis is characterised by non-zero cross-coefficients L_{1k}^{cs} and a value of $-Q_{cs}^*$ that differs from the interfacial excess enthalpy H_ϕ . From the form of the integral in eq. (2.57), it can also be seen that the thermodynamic limit ($R/r \rightarrow 0$) constitutes an upper bound for \mathbf{F}_{cs} . As a result, we conclude that the presence of a solid surface leads to dissipative effects that tend to inhibit thermophoretic motion.

In this section, I have constructed a general hydrodynamic theory for interfacial thermophoresis, showing that Onsager's reciprocal relations can be used to derive explicit expressions for the interfacial transport coefficients that determine the corresponding single-

particle contribution \mathbf{J}_{cs} to the colloidal flux, as defined by eq. (2.28). Hence, what still remains to be considered is the bulk contribution \mathbf{J}_c that represents the effect of Brownian motion and collective effects when multiple colloids are inside the system.

2.4 Bulk Thermophoresis and the Microscopic Approach

Bulk thermophoresis is usually described using a microscopic approach that relies on a clear separation of colloid-fluid interactions from colloidal pair-interactions. To justify the validity of such an approach, let us first consider the Gibbs-Duhem equation for a volume element (containing colloids and fluid) at LTE:

$$\nabla P = s' \nabla T + \sum_k n_k \nabla_T \mu_k. \quad (2.64)$$

The incompressible solvent allows a rapid momentum relaxation in the system, leading to a net momentum balance $\nabla P = \mathbf{f}_{\text{ext}}$, where \mathbf{f}_{ext} is the external body force density. As the imposed temperature gradient and \mathbf{f}_{ext} are independent, it follows that

$$T s' = h' = 0, \quad (2.65)$$

so that the total entropy (or enthalpy) density is the sum of the partial entropy (or enthalpy) densities: $s = \sum_k n_k \bar{s}$. Further, eq. (2.64) can now be rewritten as

$$c \nabla_T \mu_1 + \sum_{k \neq 1} n_k \nabla_T \mu_k = \mathbf{f}_{\text{ext}}, \quad (2.66)$$

where the colloidal component ($i = 1$) has been separated out. In order to obtain a balance equation for the bulk of the suspension, we need to make eq. (2.66) independent of the specific colloid-fluid interaction, which can be achieved by using eq. (2.21). The applicability of the Gibbs adsorption equation is therefore crucial to arrive at separate balance equation for the bulk of the suspension, as it relies on the existence of an interfacial layer that can simply be 'subtracted'. By using eq. (2.21) to eliminate the interfacial term $c \nabla_T \mu_{cs}$ in eq. (2.66), we get

$$c \nabla_T \mu_c + \sum_{k \neq 1} n_k^B \nabla_T \mu_k = \mathbf{f}_{\text{ext}}, \quad (2.67)$$

where $n_k^B = n_k - c N_k^\phi$ is the number of bulk fluid particles per volume. As every colloid occupies a volume $V_c = \frac{4}{3} \pi R^3$ of the volume element, n_k^B is related to the bulk density n_k^b of the pure fluid via $n_k^B = n_k^b (1 - \varphi)$, where $\varphi = c V_c$ is the colloidal volume fraction.

The balance equation given by eq. (2.67) is independent of the specific colloid-fluid interaction and therefore justifies the formulation of a separate microscopic approach that only considers the mutual interaction between colloids in a heat bath. A most general starting point for such a microscopic description is the generalised Fokker-Planck equation [75]

$$\begin{aligned} \frac{\partial \mathcal{P}_N}{\partial t} + \sum_i \mathbf{v}_i \nabla_i \mathcal{P}_N + \sum_{ij} \frac{\mathbf{F}_{ij}}{m} \frac{\partial \mathcal{P}_N}{\partial \mathbf{v}_i} \\ = \sum_{ij} \frac{\partial}{\partial \mathbf{v}_j} \left[\alpha_{ij} \left(\mathbf{v}_j \mathcal{P}_N + \frac{k_B T_j}{m} \frac{\partial \mathcal{P}_N}{\partial \mathbf{v}_j} \right) + \beta_{ij} \mathcal{P}_N \frac{\nabla_j T}{T_j} \right], \end{aligned} \quad (2.68)$$

where \mathcal{P}_N is the N-particle probability distribution of the colloids. The indices i and j run over all colloids inside the volume element, so that \mathbf{F}_{ij} represents the force that colloid j exerts on colloid i . The coefficients α_{ij} and β_{ij} are microscopic Onsager coefficients for the transport of momentum and heat due to hydrodynamic interactions between colloids i and j . In the absence of external forces, when $\mathbf{f}_{\text{ext}} = 0$ and $\nabla P = 0$, it has been shown that the N-particle Smoluchowski equation can be recovered from eq. (2.68) [64], yielding the result $\mathbf{J}_c = -\nabla \Pi / \xi$, where Π is the osmotic pressure of the colloids [21, 22]. The friction coefficient is given by $\xi = 6\pi b \eta R / K(\varphi)$, where the mobility factor $K(\varphi)$ accounts for hydrodynamic interactions at finite volume fraction [8]. However, as this result is obtained by neglecting β_{ij} , a more general form is instead given by

$$\mathbf{J}_c = \frac{cT}{\xi} \beta_{cc}(\varphi) \nabla \frac{1}{T} - \frac{1}{\xi} \nabla \Pi. \quad (2.69)$$

where $\beta_{cc}(\varphi)$ is a 'collective' heat coefficient. Although the evaluation of β_{cc} is beyond the scope of this work, it is clear that this quantity vanishes when the volume fraction goes to zero, which occurs in the single-colloid limit or in the case where the colloids are point-like. Eq. (2.69) can be rearranged into the same form as eq. (2.24) by making use of eq. (2.19). Due to uniformity of the total pressure ($\nabla P = 0$), it can be seen from eq. (2.19) that the osmotic pressure gradient $\nabla \Pi$ is related to the gradient in bulk fluid pressure ∇P_s^b via

$$\nabla \Pi = -\nabla P_s^b. \quad (2.70)$$

Based on eq. (2.18), the bulk fluid pressure gradient ∇P_s^b can be expressed as

$$\nabla P_s^b = s_s^b \nabla T + \sum_{k \neq 1} n_k^b \nabla_T \mu_k = h_s^b \frac{\nabla T}{T} + \sum_{k \neq 1} n_k^b \nabla_T \mu_k. \quad (2.71)$$

Due to the condition of charge neutrality, the internal body force density in the bulk fluid must vanish, such that $\sum_{k \neq 1} n_k^b \mathbf{F}_k = 0$. Using this result, eq. (2.71) can alternatively be written as

$$\nabla P_s^b = h_s^{lb} \frac{\nabla T}{T} + \sum_{k \neq 1} n_k^b \{ \nabla_T \mu_k - \mathbf{F}_k \}, \quad (2.72)$$

which is equivalent to eq. (2.43). Eq. (2.72) shows that $\vec{\mathcal{F}}_b = -\nabla P_s^b = \nabla \Pi$, confirming my previous statement that a non-zero value of $\vec{\mathcal{F}}_b$ stems from collective effects or Brownian motion inside a system where the colloidal concentration is non-zero. Combining eqs. (2.72), (2.69) and (2.67), the flux \mathbf{J}_c thus takes the form

$$\mathbf{J}_c = L_{11} \left(\beta_{cc} - \frac{h_s^{lb}}{c} \right) \nabla \frac{1}{T} - \frac{L_{11}}{T} \nabla_T \mu_c - \frac{L_{11}}{T} \sum_{k \neq 1} V_c n_k^b \{ -\nabla_T \mu_k + \mathbf{F}_k \} \quad (2.73)$$

and a comparison to eq. (2.24) yields the following Onsager coefficients for bulk thermophoresis:

$$L_{1q}^c = \left(\beta_{cc} - \frac{h_s^{lb}}{c} \right) L_{11}, \quad (2.74)$$

$$L_{1k}^c = -V_c n_k^b L_{11}. \quad (2.75)$$

$$(2.76)$$

In analogy to eq. (2.31), we can further define an effective driving force \mathbf{F}_c behind bulk thermophoresis via $\mathbf{J}_c = \frac{c}{\xi} \mathbf{F}_c$, such that

$$\mathbf{F}_c = -Q_{1q}^c \frac{\nabla T}{T} - \nabla_T \mu_c + \sum_{k \neq 1} N_{1k}^c \{ -\nabla_T \mu_k + \mathbf{F}_k \}, \quad (2.77)$$

where the bulk transport coefficients Q_{1q}^c and N_{1k}^c are given by

$$Q_{1q}^c = \beta_{cc} - \frac{h_s^{lb}}{c}, \quad (2.78)$$

$$N_{1k}^c = -V_c n_k^b. \quad (2.79)$$

Although eqs. (2.78) and (2.79) have been derived from a microscopic approach using the notion of osmotic pressure, it is important to note that these transport quantities could

also have been obtained from Onsager's reciprocal relations. A crucial implication of this is that eqs. (2.78) and (2.79) are expected to remain valid even in the presence of external forces when $\nabla P \neq 0$. Indeed, N_{1k}^c simply corresponds to the number of fluid particles that need to be displaced in the bulk when a colloid of volume V_c moves into a volume element at uniform temperature and chemical potential. Similarly, it can be seen that the term h_s^{lb} in Q_{1q}^c corresponds to the heat transported by a uniform fluid flow \mathbf{u}_∞ through a field of mutually interacting colloids. It now becomes clear that the coefficient β_{cc} must account for heat dissipation due to hydrodynamic interactions. These dissipative effects can best be understood by writing the flow velocity as $\mathbf{u}_s(\mathbf{r}) = \mathbf{u}_\infty + \delta\mathbf{u}(\mathbf{r})$, where the contribution $\delta\mathbf{u}(\mathbf{r})$ accounts for the flow engendered by every single colloid and for hydrodynamic interactions between colloids. The coefficient β_{cc} must therefore account for the heat transport $h_s^{lb} \delta\mathbf{u}$ resulting from a non-uniformity in the flow due to the colloids. Furthermore, the transport of heat out of the interfacial layer of one colloid can also be modified by the fluid flows induced by all other colloids. This raises the fundamental question why the total colloidal flux is not directly determined from the reciprocal relations, but instead split up into an interfacial contribution and a bulk contribution that are evaluated separately using different approaches. The reason is that the fluid flow field $\mathbf{u}_s(\mathbf{r})$ required in the reciprocal argument cannot be determined in a straightforward manner if there are multiple colloids in the system. The separation of \mathbf{J} into \mathbf{J}_{cs} and \mathbf{J}_{cc} thus allows us to describe colloidal thermophoresis as a superposition of an interfacial single-particle phenomenon and a bulk effect in the regime where the cross-coupling between \mathbf{J}_{cs} and \mathbf{J}_c is weak, namely at low colloidal concentrations. As a result, the only coefficient that remains unknown in this description is the collective heat coefficient β_{cc} , which represents the dissipative character of bulk thermophoresis at higher concentrations.

2.5 The Thermophoretic Flux

We can now combine the bulk contribution \mathbf{J}_c with the interfacial contribution \mathbf{J}_{cs} to obtain an expression for the total colloidal flux $\mathbf{J} = \mathbf{J}_{cs} + \mathbf{J}_{cc}$. Collecting all derived Onsager relations, given by eqs. (2.29), (2.30), (2.74) and (2.75), we get

$$\mathbf{J} = \mathbf{J}_{cs} + \mathbf{J}_c = L_{iq} \nabla \frac{1}{T} + \frac{1}{T} \sum_k L_{ik} \{ -\nabla_T \mu_k + \mathbf{F}_k \}, \quad (2.80)$$

where the corresponding Onsager coefficients can be identified as

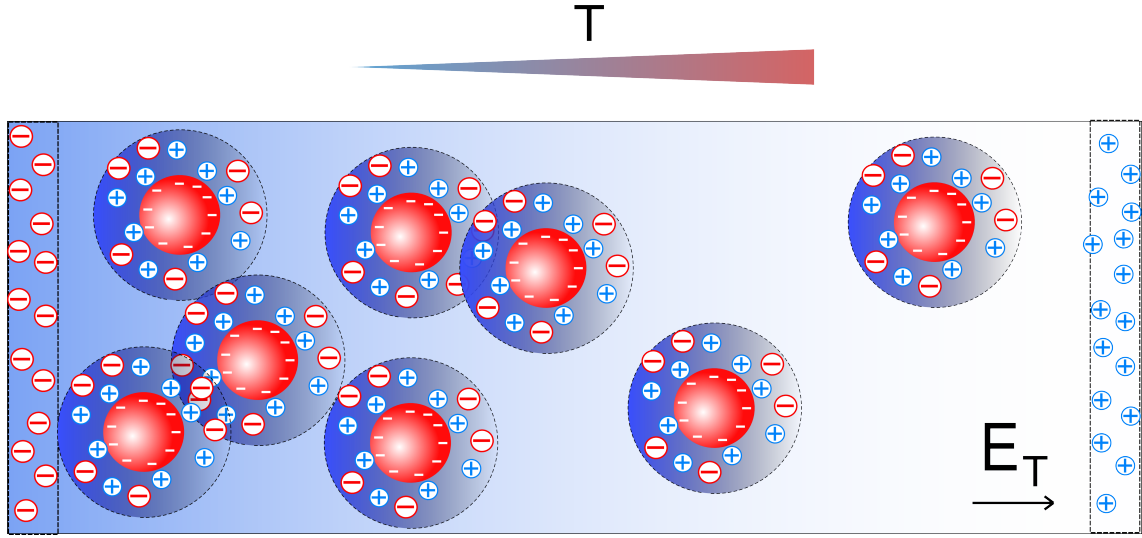


Figure 2.5: Charged colloids dispersed in a bulk fluid at steady-state in a temperature gradient. The bulk fluid is made of solvent (*e.g.* water) and ionic solutes (*e.g.* ions and counterions). The chemical potential gradients of the bulk fluid (light blue gradient in the background) couple to the fluid excess inside the layers around the colloids and the thermophoretic separation of ions and counterions in the bulk leads to the build-up of a thermoelectric field $\mathbf{E}_T = -V_T \nabla T / T$. The resulting interfacial forces on the colloid are all taken into account in the evaluation of \mathbf{J}_{cs} . Brownian motion and pair-interactions resulting from overlapping layers further give rise to an additional bulk contribution \mathbf{J}_c , which is closely related to the osmotic pressure gradient. The dimensions of colloid and system are not to scale, as the system should actually contain a much larger number of colloids.

$$L_{11} = \frac{cT}{\xi}, \quad (2.81)$$

$$L_{1q} = L_{1q}^{cs} + L_{1q}^c = \left(Q_{1q}^{cs} + \beta_{cc} - \frac{h_s^b}{c} \right) L_{11}, \quad (2.82)$$

$$L_{1k \neq 1} = L_{1k}^{cs} + L_{1k}^c = \left(N_{1k}^{cs} + N_k^\phi - V_c n_k^b \right) L_{11}. \quad (2.83)$$

A reduction to the phenomenological expression of the thermophoretic flux given by eq. (1.1) can now be achieved by making use of the assumptions introduced in section 2.2. Due to the length and time scale separation between the colloid and the fluid, which marks the transition from the micron-scale of the colloid to the nano- or even picometer-scale of the fluid, the bulk fluid is expected to relax to steady-state much faster than the colloids. In milli- or centimeter-sized systems, it is therefore reasonable to assume that the bulk fluid reaches steady-state before the colloids move over a considerable distance compared to

the system size. For visual aid, a schematic depiction of charged colloids dispersed in a bulk fluid at steady-state inside a temperature gradient is shown in fig. 2.5. A noticeable delay of this relaxation might however occur in larger systems, in which case the reduced form given by eq. (1.1) will only hold in the long-time regime of the experiment. To obtain explicit, time-independent expressions for the diffusion coefficient D and the thermal diffusion coefficient D_T , we shall assume that the relaxation of the bulk fluid to steady-state happens instantaneously. This steady-state could in principle be perturbed by the bulk flux \mathbf{J}_c of colloids, which must be balanced by an opposite flux \mathbf{J}_k^b of bulk fluid, such that

$$m_1 \mathbf{J}_c = - \sum_{k \neq 1} m_k \mathbf{J}_k^b, \quad (2.84)$$

where m_1 is the mass of a colloid. Due to assumption 2 stated in section 2.2, this effect can however be ignored as eq. (2.67) shows that the corresponding force on a particle of fluid component k is expected to be about c/n_k times smaller than the thermodynamic force $-\nabla_T \mu_c$. In dilute suspensions ($c \ll n_{k \neq 1}$), it is therefore also reasonable to assume that the bulk motion of colloids leaves the steady-state of the bulk fluid unperturbed. The incompressibility of the solvent ($k = 0$) further implies that $n_0^\phi = 0$, meaning that there is no coupling between \mathbf{J}_{cs} and $\nabla \mu_0$. Based on eq. (1.5), the steady-state distribution of the fluid components ($k \neq 1$) in the bulk is described by $\nabla n_k^b = -n_k^b S_T^k \nabla T$, where S_T^k is the Soret coefficient of fluid component k . The chemical potential gradients $\nabla_T \mu_k$ and thermoelectric forces \mathbf{F}_k in eq. (2.80) can hence be written as

$$\nabla_T \mu_k = \sum_{j \neq 0} \left(\frac{\partial \mu_k}{\partial n_j^b} \right)_{P,T} \nabla n_j^b = -\nabla T \sum_{j \neq 0,1} n_j^b S_T^j \frac{\partial \mu_k}{\partial n_j^b} + \nabla c \frac{\partial \mu_k}{\partial c} \quad (2.85)$$

and

$$\mathbf{F}_k = -z_k V_T \frac{\nabla T}{T}, \quad (2.86)$$

where z_k is the valence of a particle of component k . The thermoelectric potential V_T is fixed by the steady-state of the ionic solutes [58]. To simplify the notation, let us introduce the net transport coefficients $Q_{1q} = L_{1q}/L_{11}$ and $N_{1k} = L_{1k}/L_{11}$, such that

$$Q_{1q} = Q_{1q}^{cs} + \beta_{cc} - \frac{h_s^{ib}}{c}, \quad (2.87)$$

$$N_{1k} = \begin{cases} 1 & \text{if } k = 1 \\ N_{1k}^{cs} + N_k^\phi - V_c n_k^b & \text{if } k \neq 1. \end{cases} \quad (2.88)$$

By substituting eqs. (2.85) and (2.86) into eq. (2.80), the colloidal flux finally takes the form

$$\mathbf{J} = -D\nabla c - cD_T\nabla T, \quad (2.89)$$

where the diffusion coefficient D and the thermal diffusion coefficient D_T of the colloid are respectively given by

$$\xi D = c \sum_k N_{1k} \frac{\partial \mu_k}{\partial c} = \frac{\partial \Pi}{\partial c} + c \sum_{k \neq 1} N_{1k}^{cs} \frac{\partial \mu_k}{\partial c}. \quad (2.90)$$

$$\xi D_T = \frac{Q_{1q}}{T} - \sum_k N_{1k} \left\{ \sum_{j \neq 0,1} n_j^b S_T^j \frac{\partial \mu_k}{\partial n_j^b} - \frac{z_k V_T}{T} \right\}. \quad (2.91)$$

From eqs. (2.91) and (2.90), it can be seen that the Soret coefficient of the colloids $S_T = D_T/D$ is independent of the friction coefficient ξ . The Soret coefficient is therefore insensitive to hydrodynamic interactions due to collective colloidal motion, but might nonetheless depend on bulk fluid flows through the collective heat coefficient $\beta_{cc}(\varphi)$ contained in Q_{1q} . For a separate interpretation of interfacial and bulk thermophoresis, the thermal diffusion coefficient can be split up into $D_T = D_T^{cs} + D_T^c$, where each term represents the thermal diffusion coefficient of the corresponding flux contribution. From the expressions of \mathbf{J}_{cs} and \mathbf{J}_c as given by eqs. (2.28) and (2.69), these can readily be identified as

$$\xi D_T^{cs} = \frac{Q_{1q}^{cs}}{T} - \sum_{k \neq 0,1} N_{1k}^{cs} \left\{ \sum_{j \neq 0,1} n_j^b S_T^j \frac{\partial \mu_k}{\partial n_j^b} - \frac{z_k V_T}{T} \right\}, \quad (2.92)$$

$$\xi D_T^c = \frac{\beta_{cc}}{T} + \frac{1}{c} \frac{\partial \Pi}{\partial T}. \quad (2.93)$$

In general, we note that both D_T^{cs} and D_T^c depend on the Soret coefficients S_T^j of the fluid components, meaning that the signs of D_T^{cs} and D_T^c do not only depend on whether the specific interactions of the colloids are attractive or repulsive. In the special case where the colloids are point-like ($V_c = 0$) and ideal (no specific interactions), we have $\beta_{cc} = 0$, $N_{1k} = \delta_{1k}$ and $n_k^b \partial \mu_c / \partial n_k^b = \delta_{1k} k_B T$, where δ_{1k} is the Kronecker delta. The Einstein relation

$$\xi D = k_B T \quad (2.94)$$

is then directly recovered from eq. (2.90). As the ideal osmotic pressure is just $\Pi = ck_B T$, the corresponding ideal contribution to the thermal diffusion coefficient is given by

$$\xi D_T = k_B. \quad (2.95)$$

In dilute suspensions, colloidal motion is mainly driven by interfacial thermophoresis and the single-colloid limit is therefore of particular interest. For a single colloid, the Einstein relation $\xi D = k_B T$ holds and the thermal diffusion coefficient takes the simple form

$$D_T = D_T^{cs} + \frac{k_B}{\xi}. \quad (2.96)$$

The ideal contribution k_B/ξ is usually multiple orders of magnitude weaker than D_T^{cs} and is therefore often neglected [71]. Within the single-colloid limit, let us now consider the special case where the fluid only consists of solvent. The Soret coefficient of a colloid is then just given by

$$S_T = \frac{Q_{1q}^{cs}}{k_B T^2} + \frac{1}{T}. \quad (2.97)$$

In fact, this result is also commonly used to describe ionic thermophoresis due to hydration [1], by treating the ionic solute as a dilute gas of non-interacting, charged particles surrounded by hydration shells. The steady-state of the ionic solute j in the bulk fluid is thus governed by

$$\nabla n_j^b + n_j^b S_T^j \nabla T = 0 \quad (2.98)$$

with an ionic Soret coefficient

$$S_T^j = \frac{Q_{jq} + z_j V_T}{k_B T^2} + \frac{1}{T}. \quad (2.99)$$

In analogy to eq. (2.56), the interfacial heat of transport Q_{jq} of the ion can be related to the interfacial excess enthalpy density $h_\phi^j(r)$ of the surrounding water molecules via [1]

$$Q_{jq} = - \int_{R_j}^{\infty} h_{\phi}^j(r) \left(1 - b_j \frac{R}{r}\right) 4\pi r^2 dr, \quad (2.100)$$

which in the Hückel limit reduces to $Q_{jq} = -H_{\phi}^j$, where the interfacial excess enthalpy H_{ϕ}^j of the hydration shell around the ion is also known as the enthalpy of solvation. The term $z_j V_T$ in eq. (2.99) accounts for the thermoelectric force that directly acts on the ion. It should be noted that small ions do not necessarily satisfy assumptions 1 and 5 in section 2.2, so that deviations from eq. (2.100) should be expected due to distortions of the hydration shell. An explicit expression for V_T can further be obtained by multiplying eq. (2.98) by z_j and summing over all ionic solutes ($j \neq 0, 1$), giving

$$V_T = - \frac{\sum_j n_j^b z_j Q_{jq}}{\sum_j n_j^b z_j^2}, \quad (2.101)$$

where the condition of charge neutrality $\sum_j z_j n_j^b = 0$ has also been used. Remembering that the solvent is incompressible and that the solutes have negligible sizes, the partial derivatives of the solute chemical potentials in eq. (2.93) reduce to $n_j^b \partial \mu_k / \partial n_j^b = \delta_{kj} k_B T$. By substituting eq. (2.99) into eq. (2.92), the thermal diffusion coefficient D_T^{cs} of a charged colloid becomes

$$\xi T D_T^{cs} = Q_{1q}^{cs} - \sum_{k \neq 0,1} N_{1k}^{cs} (Q_{kq} + k_B T) \quad (2.102)$$

$$= - \int_R^{\infty} \left[q_{\phi}(r) - \sum_{k \neq 0,1} n_k^{\phi}(r) (Q_{kq} + k_B T) \right] \left(1 - b \frac{R}{r}\right) 4\pi r^2 dr \quad (2.103)$$

$$= - \int_R^{\infty} q_{\phi}^*(r) \left(1 - b \frac{R}{r}\right) 4\pi r^2 dr \quad (2.104)$$

In dilute aqueous suspensions, the thermal diffusion coefficient D_T^{cs} of charged colloids can hence be evaluated using the hydrodynamic form given by eq. (2.56), by replacing the interfacial heat density q_{ϕ} with the density q_{ϕ}^* , which also accounts for the heat transport due to hydration and Brownian motion of ions inside the interfacial layer of a colloid. The evaluation of D_T^{cs} does therefore not require an explicit determination of the thermoelectric potential V_T .

With a complete theoretical description of colloidal thermophoresis at hand, we are finally able to examine the validity of the theoretical approaches proposed by Würger [90] and Dhont [24] for a charged colloid in an aqueous electrolyte solution, which have yielded

different dependences of the Soret coefficient S_T on the colloidal radius R and interfacial width λ .

2.6 Discussion and Comparison

Würger's theoretical model for interfacial thermophoresis is based on a derived expression for the interfacial force density at the surface of a charged colloid [90, 62]. The colloidal surface is screened by the ionic solute, leading to the formation of an electric double layer [19] (fig. 2.2). The ions are treated as a dilute gas of non-interacting, point-like particles surrounded by hydration shells, with corresponding densities

$$n_k(\mathbf{r}) = n_k^b \exp\left(-\frac{\phi_k(\mathbf{r})}{k_B T}\right) \quad (2.105)$$

around the colloid. The pressure gradient is directly evaluated from the ionic solute pressure $P_s(\mathbf{r})$, given by

$$P_s(\mathbf{r}) = \sum_{k \neq 0,1} n_k(\mathbf{r}) k_B T \quad (2.106)$$

and the body force density acting on the fluid element reads

$$\mathbf{f}_s(\mathbf{r}) = - \sum_{k \neq 0,1} n_k(\mathbf{r}) (\nabla \phi_k(\mathbf{r}) - \mathbf{F}_k) - \frac{1}{2} \varepsilon_T \varepsilon E^2(\mathbf{r}) \frac{\nabla T}{T}, \quad (2.107)$$

where \mathbf{F}_k is the thermoelectric force, ε is the electric permittivity and $\varepsilon_T = \partial \ln \varepsilon / \partial \ln T$. The last term in eq. (2.107) corresponds to the interfacial excess enthalpy density of the polarised solvent (*e.g.* water) in the local electric field \mathbf{E} of the colloid [51] and should therefore be interpreted as a contribution to the pressure gradient rather than the body force density. As the net force density is defined by $\vec{\mathcal{F}} = \mathbf{f}_s - \nabla P_s$, Würger's interfacial force density takes the form

$$\begin{aligned} \vec{\mathcal{F}}_\phi(r) = \vec{\mathcal{F}} - \vec{\mathcal{F}}_b &= - \sum_{k \neq 0,1} \left(n_k(r) \phi_k(r) + n_k^\phi(r) k_B T \right) \frac{\nabla T}{T} - \frac{1}{2} \varepsilon_T \varepsilon E^2(r) \frac{\nabla T}{T} \\ &+ \sum_{k \neq 0,1} n_k^\phi(r) (-\nabla_T \mu_k + \mathbf{F}_k), \end{aligned} \quad (2.108)$$

where $\nabla_T \mu_k = k_B T \nabla \ln n_k^b$ for a non-interacting, point-like gas. Using the relation $h_s = P_s + u_{\text{int}}$, where u_{int} is the internal energy density, the total enthalpy density of the ionic solutes at the colloidal surface and in the bulk can be expressed as

$$h_s(r) = P_s(r) + \sum_{k \neq 0,1} n_k(r) \left(\phi_k(r) + \frac{3}{2} k_B T + \bar{H}_k^0 \right), \quad (2.109)$$

$$h_s^b = P_s^b + \sum_{k \neq 0,1} n_k^b \left(\frac{3}{2} k_B T + \bar{H}_k^0 \right), \quad (2.110)$$

where the term \bar{H}_k^0 accounts for ionic hydration. As the partial molar enthalpy of solute k is just $\bar{H}_k = \frac{3}{2} k_B T + \bar{H}_k^0$ (see appendix B), the interfacial enthalpy density $h_\phi(r)$ of the ionic gas around the colloid becomes

$$h_\phi(r) = h'_s(r) - h_s^{b'} = \left(h_s(r) - \sum_{k \neq 0,1} n_k(r) \bar{H}_k \right) - \left(h_s^b - \sum_{k \neq 0,1} n_k^b \bar{H}_k \right) \quad (2.111)$$

$$= \sum_{k \neq 0,1} \left(n_k(r) \phi_k(r) + n_k^\phi(r) k_B T \right). \quad (2.112)$$

With eq. (2.112), eq. (2.108) can be written in the same form as eq. (2.44), proving that Würger's result is in agreement with my more general expression for the interfacial force density. With eq. (2.56), Würger then determines the interfacial driving force \mathbf{F}_{cs} in the boundary layer approximation ($R \gg \lambda$) by computing the fluid slip velocity when a temperature gradient is applied across the interfacial layer (derivation given in appendix C). Although this approach is inherently different from my derivation based on reciprocal arguments, Würger's final result coincides with my expression for colloids with a stick boundary condition, given by

$$\mathbf{F}_{cs} = -4\pi R \int_0^\infty z \vec{\mathcal{F}}_\phi(z) dz. \quad (2.113)$$

Whether considering an ideal or non-ideal fluid, it is clear that any additional size-dependence in $\vec{\mathcal{F}}_\phi(z)$ would have to stem from a direct dependence of $\phi(z)$ on R . However, the potential $\phi(z)$ is generally independent of colloidal size in the limit $R \gg \lambda$ where the shape of the colloid does not matter [91]. As the interfacial force on the colloid simply reduces to the thermophoretic force $\mathbf{F}_T = -\xi D_T \nabla T$ when the bulk fluid is at steady-state, it directly follows from eq. (2.113) that $\mathbf{F}_T \propto R$. In view of the Einstein relation $\xi D = k_B T$, the corresponding Soret coefficient of the colloid, given by $S_T = D_T/D = -\mathbf{F}_T/(k_B T \nabla T)$, hence also satisfies the linear scaling relation $S_T \propto R$. In fact, the linearity in R for a stick boundary holds irrespective of the size ratio between colloid and layer when $\vec{\mathcal{F}}_\phi$ is independent of R . This can be seen by setting $b = 1$ in eq. (2.58), giving

$$\mathbf{F}_{cs} = -4\pi \int_0^\infty z^2 \vec{\mathcal{F}}_\phi(z) dz - 4\pi R \int_0^\infty z \vec{\mathcal{F}}_\phi(z) dz, \quad (2.114)$$

where the first term just represents a constant offset in a plot of \mathbf{F}_{cs} vs R . As the stick boundary condition is believed to be a good approximation for colloids under most experimental conditions, the Soret coefficient should be observed to increase linearly with colloidal radius. Nonetheless, it is worth noting that a more complex quadratic behaviour in R may occur when there is slippage at the colloidal surface, as evidenced by eq. (2.58).

Similar to other authors [32, 12, 88, 21], Dhont's approach to interfacial thermophoresis is based on a minimal model where the interfacial force is derived from a gradient in a certain thermodynamic potential U_T^{cs} associated with the colloid. This potential is determined by treating the colloid as a charging capacitor undergoing a Gibbs adsorption process at uniform temperature and pressure [24]

$$U_T^{cs} = - \sum_{k \neq 1} \int N_k^\phi (d\mu_k)_T = \mu_{cs}, \quad (2.115)$$

so that U_T^{cs} coincides with the interfacial chemical potential μ_{cs} . The corresponding colloidal flux is then given by:

$$\mathbf{J} = -\frac{c}{\xi} \nabla \mu_{cs} - \frac{1}{\xi} \nabla \Pi. \quad (2.116)$$

First of all, it is worth noting that the above form does not account for a thermoelectric force \mathbf{F}_1 , showing that the thermoelectric effect cannot simply be derived from a minimal model. Eq. (2.116) contains the appropriate form for \mathbf{J}_c with the neglect of $\beta_{cc}(\varphi)$. A comparison to eq. (2.62) shows that Dhont's capacitor model evaluates \mathbf{J}_{cs} in the Hückel limit, which should however not apply to colloidal thermophoresis as it only holds when $R \ll \lambda$. Dhont nonetheless applies this model to the colloidal regime $R \gg \lambda$ where $\phi(r)$ is independent of R , obtaining an interfacial driving force given by:

$$\mathbf{F}_{cs} = - \int_R^\infty \vec{\mathcal{F}}_\phi(z) dV = -4\pi R^2 \int_R^\infty \vec{\mathcal{F}}_\phi(z) dz. \quad (2.117)$$

Using the same scaling arguments as for eq. (2.113), this capacitor model leads us to the flawed conclusion that the Soret coefficient is directly proportional to the surface area of the colloid $S_T \propto R^2$. The general problem with minimal models is that they are purely based on the minimisation of a thermodynamic potential. The form of this potential then automatically imposes certain relations for the Onsager coefficients that should actually be determined based on hydrodynamic and reciprocal arguments, as shown in the previous sections. It is

therefore clear that such minimal models cannot properly account for the hydrodynamic character of colloidal thermophoresis.

2.7 Conclusion

In this chapter, I have introduced a well-founded framework for colloidal thermophoresis based on the length and time scale separation in colloidal suspensions, which allows a separate evaluation of the interfacial and bulk contribution to the colloidal flux. I have shown how a hydrodynamic theory based on Onsager's reciprocal relations can be used to derive explicit expressions for the transport coefficients that govern interfacial thermophoresis. A careful analysis of these expressions has proven that colloidal thermophoresis cannot solely be explained by the thermodynamic treatment proposed by Dhont, but that it has a hydrodynamic character related to irreversible fluid flows in thin boundary layers. The recovery of existing limiting cases further shows that my theoretical work draws a clear connection between hydrodynamic and thermodynamic approaches within the theory of NET.

However, my results also suggest that interfacial thermophoresis is not only set by the sign and strength of the interaction between the colloid and the fluid, but that it also depends on the steady-state of the bulk fluid, leading to a complex interplay of different effects when the fluid is made of multiple ionic and non-ionic components. To examine the validity of the underlying hydrodynamic approach, it is more instructive to consider a single colloid suspended in a one-component fluid. In the following chapter, I will therefore study such a system using computer simulations. In particular, the range of validity of my theoretical model and the parameter-dependence of the thermophoretic force will be explored.

Chapter 3

Simulation

As I have shown in the theoretical section, the sign and strength of interfacial thermophoresis are related to the specific interaction between the colloid and the fluid, resulting in the build-up of an interfacial layer around the colloid. These interactions are often hard to control in experiments, making a direct comparison to theory difficult. Simulations therefore provide a promising alternative for testing theoretical predictions as they allow a very fine and controlled tuning of interactions and transport coefficients. Choosing the appropriate level of coarse graining for these simulations is however not always straightforward [81].

Due to the hydrodynamic character of thermophoresis, the chosen simulation technique must be able to reproduce fluid flows. Although Molecular Dynamics (MD) has previously been used to simulate non-equilibrium motion in a temperature gradient [86, 36], the reproduction of fluid flows based on MD is computationally expensive as it relies on the microscopic resolution of intermolecular interactions in a system containing up to a million fluid particles. A far more coarse-grained approach can be achieved by abandoning the molecular description of the fluid and simulating the effect of colloid-fluid interactions implicitly via a generalised Langevin equation [31, 40, 16]. Langevin Dynamics (LD) thus requires an analytic expression of the net force on the colloid as an input to solve the corresponding equation of motion, implying that it cannot be used to test my theoretical prediction for the thermophoretic force.

For colloids, it is instead more convenient to adopt a hybrid mesoscale-molecular dynamics scheme known as Multi-Particle Collision Dynamics (MPC) [59], which reproduces hydrodynamic flows and thermal fluctuations on a mesoscopic scale without explicitly resolving the molecular dynamics of the fluid. So far, most existing MPC simulations of thermophoresis have been performed by modelling both the specific and collisional interaction between the colloid and the fluid with Lennard-Jones potentials, corresponding to a slip boundary condition at the colloidal surface [54, 57, 55]. Although both stick and slip

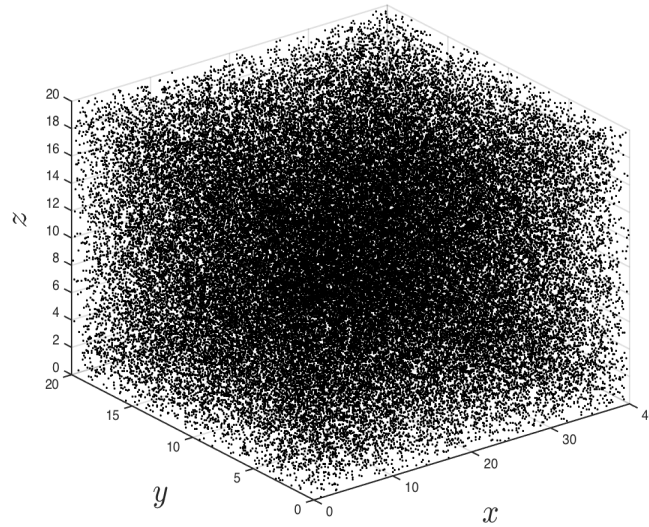


Figure 3.1: Snapshot of simulation box filled with point-like MPC fluid particles.

surfaces have been considered elsewhere [94, 95], these studies focussed on the interplay between thermophoretic drifts and interfacial flows without relating the physical cause of these drifts to an underlying theoretical model. However, an effective use of the thermophoretic effect in soft matter and biological systems relies on an accurate prediction of its sign and strength. Here, I bridge this gap by relating my simulation results to the theoretical model for interfacial thermophoresis developed in the previous chapter. I will present accurate measurements of the thermophoretic force acting on a single colloid, which are found to be well described by my theoretical prediction. The colloid is modelled as a fixed solid sphere in a temperature gradient, interacting with the MPC fluid via a polynomial potential that decays with radial distance from the surface. The application of a stick or slip boundary condition at the surface allows an on and off switching of the shear force, a component that has mostly been overlooked in existing MPC simulations of thermophoresis. I start this chapter with an introduction to MPC, followed by a detailed description of the simulated system.

3.1 Multi-Particle Collision Dynamics

3.1.1 Introduction to the Simulation Technique

MPC is situated in between MD and LD on the coarse-graining scale, thus reducing the computational costs while preserving a mesoscopic description of hydrodynamic fluid flows.

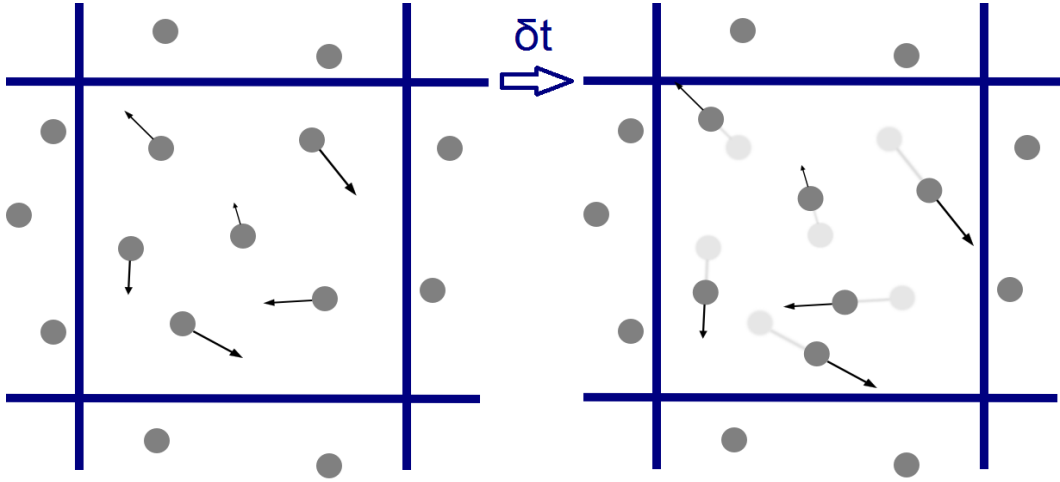


Figure 3.2: Schematic diagram of the streaming step in a unit cell. The black arrows represent the instantaneous particle velocities.

MPC is particularly well suited for the simulation of thermophoresis because it reproduces thermal fluctuations and allows a straightforward implementation of temperature inhomogeneities in the system [56]. The molecular complexity of the fluid is reduced by introducing ideal fluid particles that carry the same energy and momentum as the non-ideal fluid, but whose collisions and interactions are no longer resolved explicitly. A random distribution of such MPC particles in a simulation box is shown in fig 3.1. The MPC fluid follows the ideal gas equation of state $P = nk_B T$ and its motion is simulated by performing alternating streaming and collision steps. In the streaming step (fig. 3.2), the fluid particles of mass m follow ballistic trajectories for a discrete time δt :

$$\mathbf{r}_i(t + \delta t) = \mathbf{r}_i(t) + \mathbf{v}_i(t)\delta t, \quad (3.1)$$

where $\mathbf{r}_i(t)$ and $\mathbf{v}_i(t)$ are the position and velocity of fluid particle i at time t . The collision step allows the transfer of energy and momentum between fluid particles based on a coarse-grained rotation procedure that neglects the molecular structure of the fluid (fig. 3.3). The system is first split into a randomly positioned but regularly spaced lattice of cubic cells, each of length a . In each cell, particle velocities are then updated corresponding to a rotation through a constant angle α about a randomly chosen axis [3]:

$$\mathbf{v}_i(t + \delta t) = \mathbf{v}_{\text{CM}}(t) + \mathcal{R}(\alpha)[\mathbf{v}_i(t) - \mathbf{v}_{\text{CM}}(t)], \quad (3.2)$$

where $\mathcal{R}(\alpha)$ is the rotation operator. The centre of mass velocity of the considered cell \mathbf{v}_{CM} corresponds to the local fluid flow velocity \mathbf{u}_s . In view of eq. (3.2), it is the thermal velocity $\mathbf{v}_{\text{th}} = \mathbf{v}_i - \mathbf{v}_{\text{CM}}$ that is rotated around the randomly chosen axis. This axis is specified by a corresponding unit vector \mathbf{R} , with components [3]

$$R_x = \cos \varphi \sqrt{1 - \rho^2}, \quad R_y = \sin \varphi \sqrt{1 - \rho^2}, \quad R_z = \rho \quad (3.3)$$

where $\varphi = 2\pi R_1$, $\rho = 2R_2 - 1$, and R_1 and R_2 are uncorrelated random numbers drawn from a uniform distribution in the interval $[0,1]$. As the rotation only affects the component \mathbf{v}_{\perp} of \mathbf{v}_{th} perpendicular to \mathbf{R} , the rotated thermal velocity can be written as $\mathbf{v}'_{\text{th}} = \mathbf{v}_{\alpha} + \mathbf{v}_{\parallel}$, where \mathbf{v}_{\parallel} is the component of \mathbf{v}_{th} parallel to \mathbf{R} . The rotated component \mathbf{v}_{α} can then straightforwardly be calculated from

$$\mathbf{v}_{\alpha} = \mathbf{v}_{\perp} \cos \alpha + (\mathbf{v}_{\perp} \times \mathbf{R}) \sin \alpha \quad (3.4)$$

where $\mathbf{v}_{\perp} \times \mathbf{R}$ designates the corresponding vector product.

By construction, the algorithm conserves energy and momentum and correctly reproduces Navier-Stokes dynamics on length scales larger than a [59], but it does not obey the principle of Galilean Invariance if the same lattice of unit cells is used for each collision step. The reason is that, for a fixed lattice, fluid particles in the same cell repeatedly collide with each other rather than with other particles in neighbouring cells, resulting in local correlations that mark the breakdown of molecular chaos. However, the chaos assumption can be restored by shifting the lattice through a random vector with coordinates in the range $[-a/2, a/2]$ before each collision step [42, 43, 50].

Simulation units are simplified by setting $m = 1$, $a = 1$, $k_B = 1$ and $T_0 = 1$, where T_0 is a standard reference value for the system temperature. Time and speed are thus given in units of $(ma^2/k_B T_0)^{1/2}$ and $(k_B T_0/m)^{1/2}$ respectively [80]. In my simulations, I have used the standard MPC parameter values $\alpha = 120^\circ$, $\delta t = 0.1$ and an average number of $M = 7$ particles per cell, as this choice has been shown to reproduce liquid-like behaviour of the MPC fluid [38]. Analytical expressions for the fluid transport coefficients can further be derived based on these MPC properties [44, 84, 45], with an expression for the self-diffusion coefficient D_s of the fluid given by

$$D_s = \frac{k_B T \delta t}{2m} \left[\frac{3n}{(1 - \cos \alpha)(n - 1 + e^{-n})} - 1 \right]. \quad (3.5)$$

Here, T and n are the local temperature and particle density in a cell, which may differ from the global values T_0 and M if the system is inhomogeneous. This theoretical prediction

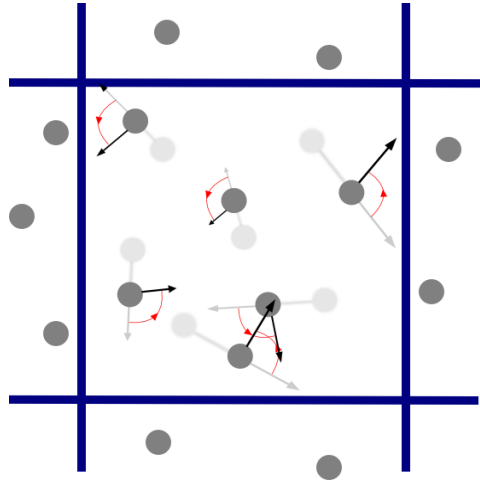


Figure 3.3: Schematic diagram of the collision step in a unit cell. The curved red arrows represent the rotation of the particle velocities.

for D_s has been verified elsewhere using a discrete version of the Green-Kubo relation [42, 44, 74]. As shown in fig. (3.4), the self-diffusion coefficient is rather insensitive to the fluid density for densities larger than 5 particles per cell. With an average number density of $M = 7$ in the system, the value of D_s is therefore expected to remain approximately constant inside flow regions where the local density coincides with or exceeds M .

3.1.2 Implementation

The simulations have been performed on a computer equipped with a Graphics Processing Unit (GPU) and a GNU/Linux operating system. The MPC code has been implemented in C++ and compiled using a standard GNU C++ compiler (g++). The streaming step and collision step are embedded as separate functions in the main function, which performs the step-wise integration over the total simulation time. Boundary conditions are treated carefully with a number of sub-functions within the streaming step. These conditions include collisions with the system boundaries and the colloidal surface as well as streaming into and out of the interfacial layer. The random numbers required in the collision step are generated by planting a seed at the start of the simulation with the `srand(time(NULL))` command and by using the pre-defined function `rand()` from the standard `<random>` library.

Due to the large number of fluid particles and unit cells, particle coordinates and cell properties are stored in dynamic arrays using the vector class. For the measurements of momentum transfer, temperature, MPC density and fluid flow, data is written to text files in regular time intervals with the output stream class `'ofstream'`. The system parameters and

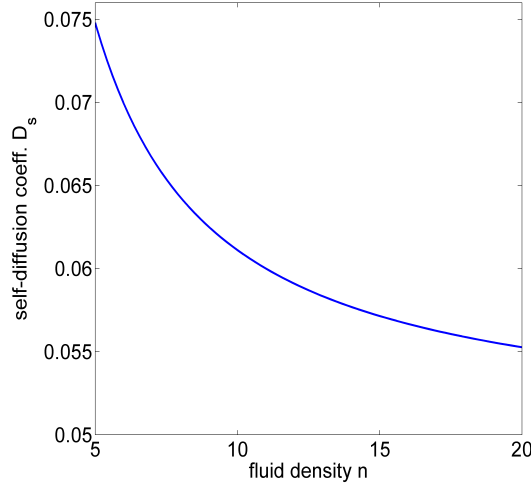


Figure 3.4: Plot of self-diffusion coefficient D_s vs fluid density n based on eq. (3.5), for standard MPC parameter values and $T = T_0$.

final coordinates are also saved and can serve as an input to the code, allowing a continuation of the simulation beyond the standard simulation time.

3.2 The Simulated System

My system consists of a stationary colloidal sphere placed in the middle of a rectangular box of dimensions $L_x \times L_y \times L_z$ containing an MPC fluid (fig. 3.5). A uniform temperature gradient of standard value $\nabla T = 0.01$ is applied along the (positive) x -direction by placing thermostat walls at $x = 0$ and $x = L_x$. The thermostats are treated with a slip boundary condition and are kept at temperatures T_c and T_h respectively, such that the temperature in the centre of the system $T(x = L_x/2)$ coincides with $T_0 = 1$. The temperature profile is given by

$$T(x) = T_c + x\nabla T, \quad (3.6)$$

where $\nabla T = (T_h - T_c)/L_x$. The existing temperature profile inside the fluid can be measured by splitting the system up into unit-slabs along the x -direction and by determining the local temperature of each slab. The temperature T_j of the j^{th} slab containing N_j particles is fixed by the equipartition of energy

$$\frac{3}{2}(N_j - 1)k_B T_j = \sum_{i \in j} \frac{1}{2} m |\mathbf{v}_i - \mathbf{v}_{\text{CM}}|^2, \quad (3.7)$$

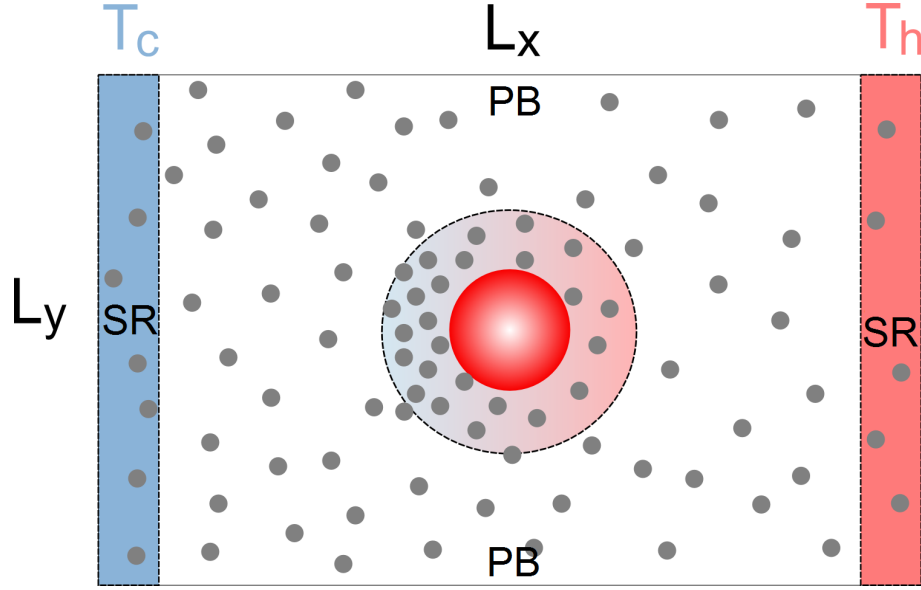


Figure 3.5: Schematic depiction of the simulated system. The colloid (red sphere) is surrounded by the MPC fluid (grey particles). A temperature gradient is maintained by performing thermal velocity rescaling in the unit slabs (blue and red slab), respectively kept at temperatures T_c and T_h . Specular Reflection (SR) is applied at the thermostats (x-direction), whereas Periodic Boundary (PB) conditions are applied in the other two directions.

where three degrees of freedom have been removed to account for the subtraction of the centre of mass velocity from each particle velocity. Different methods for the implementation of temperature inhomogeneities have been tested in recent literature [57]. Here, I employ a robust and physically intuitive technique based on thermal velocity rescaling. The gradient is maintained by rescaling the velocities of the N_{slab} fluid particles inside the unit-slab in contact with the corresponding thermostat, according to [54]:

$$\mathbf{v}'_i = \mathbf{v}_{\text{CM}} + (\mathbf{v}_i - \mathbf{v}_{\text{CM}}) \sqrt{E'/E}, \quad (3.8)$$

where

$$E = \sum_{i \in \text{slab}} \frac{1}{2} m |\mathbf{v}_i - \mathbf{v}_{\text{CM}}|^2 \quad \text{and} \quad E' = \frac{3}{2} (N_{\text{slab}} - 1) k_B T_{c,h}. \quad (3.9)$$

This rescaling hence guarantees that the measurement of T_{slab} based on eq. (3.7) produces $T_{\text{slab}} = T_{c,h}$. Periodic boundary conditions are applied in the y and z- direction. The radius R of the colloidal sphere defines the position of the solid surface with respect to its centre and is given the standard value $R = 4$. Upon collision with the stationary solid surface, a stick

or slip boundary condition is then imposed by respectively applying Bounce-Back (BB) or Specular Reflection (SR) to the coordinates of the fluid particles. For this purpose, the fluid particle is first streamed to the surface of the colloid and its velocity \mathbf{v}_i is then updated to \mathbf{v}'_i according to

$$\mathbf{v}'_i = \begin{cases} -\mathbf{v}_i^\perp - \mathbf{v}_i^\parallel & \text{for stick (BB),} \\ -\mathbf{v}_i^\perp + \mathbf{v}_i^\parallel & \text{for slip (SR),} \end{cases} \quad (3.10)$$

where \mathbf{v}_i^\parallel and \mathbf{v}_i^\perp are the velocity components parallel and perpendicular to the colloidal surface. This updated velocity is then used to stream the particle for the remaining time of the step. Hence, only the perpendicular component of the velocity is reflected with SR, so that a slip boundary condition is equivalent to modelling the colloidal surface as a radial potential wall. However, the total reflection of the particle velocity with BB results in an additional shear force $\mathbf{F}_{i,\text{shear}} = -m \left(\mathbf{v}'_i^\parallel - \mathbf{v}_i^\parallel \right) / \delta t$ on the colloid, showing that a stick boundary condition accounts for the effect of surface roughness that cannot be modelled by a soft or hard radial potential.

As the colloidal radius usually greatly exceeds the thickness of the interfacial layer, the specific colloid-fluid interaction is generally expected to be independent of R . To simulate this interaction, I have therefore used a radial potential $\phi(z)$ that is independent of R , of the form

$$\phi(z) = \varepsilon \left(1 - \frac{z}{\lambda} \right)^q, \quad 0 < z \leq \lambda \quad (3.11)$$

where $z = r - R$ is the radial distance from the surface. The cut-off distance λ defines the width of the interfacial layer, with a standard value of $\lambda = 3$. The parameter ε sets the sign and strength of the potential whereas the positive integer q quantifies its steepness. These parameters take the standard values $\varepsilon = -1$ and $q = 3$ in my simulations, corresponding to an attractive potential that decreases cubically with radial distance. By choosing $q \geq 3$, the interaction is 'well behaved' at the potential boundary, meaning that the potential is zero and its first two derivatives are continuous at $z = \lambda$. For visual aid, a schematic diagram of the colloid and its potential is shown in fig. 3.6, including a table with the standard values of the system parameters. Inside the potential, particle positions and velocities are updated by performing 50 MD steps of length δt_{MD} after each collision step, based on the Velocity-Verlet algorithm

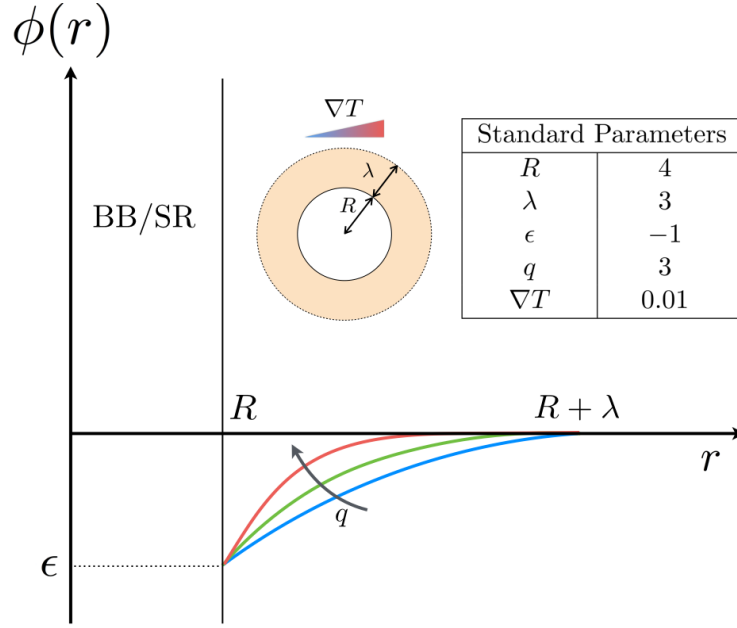


Figure 3.6: Schematic diagram of the colloid and its potential interaction. The table summarises the standard values of the main system parameters.

$$\mathbf{r}_i(t + \delta t_{MD}) = \mathbf{r}_i(t) + \delta t_{MD} \mathbf{v}_i(t) + \frac{\delta t_{MD}^2}{2m} \mathbf{F}_i(\mathbf{r}_i(t)), \quad (3.12)$$

$$\mathbf{v}_i(t + \delta t_{MD}) = \mathbf{v}_i(t) + \frac{\delta t_{MD}}{2m} [\mathbf{F}_i(\mathbf{r}_i(t + \delta t_{MD})) + \mathbf{F}_i(\mathbf{r}_i(t))], \quad (3.13)$$

where $\mathbf{F}_i(\mathbf{r}_i) = -\nabla\phi(\mathbf{r}_i)$. The MD step size $\delta t_{MD} = \delta t/50$ has previously been shown to be a sensible choice for the study of colloidal thermophoresis [67], even when steep Lennard-Jones potentials are used [95]. As the effect of finite system size on fluid flows is mainly determined by the hydrodynamic boundary conditions at the colloidal surface and the system boundaries, the system size is chosen to scale with the colloidal radius R according to $L_y = L_z = \frac{3}{4}L_x = 12R$.

The initialisation of the MPC fluid is performed per cell by splitting the system into a regular cubic lattice of unit cells. To ensure uniform pressure in the bulk of the system, the fluid density n is initialised to its ideal gas steady-state $n(T(x)) \propto T(x)^{-1}$ based on Poisson statistics and rescaled as to obtain a global bulk density equal to $M = 7$ outside the potential. The densities inside the potential are then multiplied by the Boltzmann factor $\exp(-\phi(r)/k_B T(x))$ to build up the corresponding interfacial layer. Initial velocity

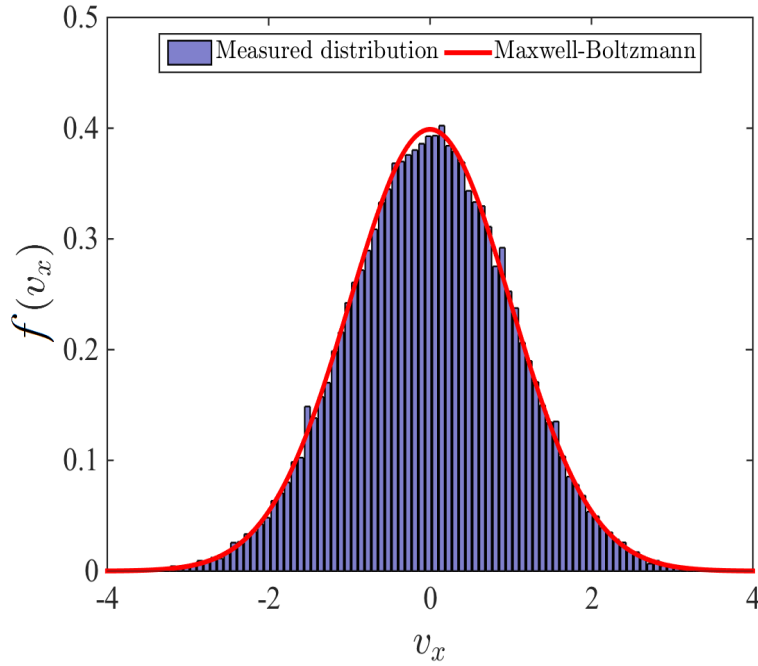


Figure 3.7: Comparison between measured velocity distribution and Maxwell-Boltzmann distribution for the x-component.

components $v_{x,y,z}$ are drawn from a local Maxwell-Boltzmann distribution at temperature $T(x)$:

$$f(v_{x,y,z}) = \left(\frac{m}{2\pi k_B T(x)} \right)^{\frac{1}{2}} \exp \left(-\frac{mv_{x,y,z}^2}{2k_B T(x)} \right). \quad (3.14)$$

The system is then simulated according to MPC dynamics for a total simulation time of $\tau = 2 \times 10^5 \delta t$. The Maxwell-Boltzmann distribution for the thermal velocities remains preserved in the MPC fluid throughout the simulation, as shown in fig. (3.7). Furthermore, the steady-state of the system is verified by measuring the time-averaged temperatures and densities in the cells. The right side of fig. 3.8a shows a measured density histogram of the centred slice along the temperature gradient, averaged around the axis of rotational symmetry (white line). The ideal gas steady-state used for initialisation is displayed on the left side of the axis. The agreement between both sides is particularly good in the bulk, showing that the bulk pressure remains uniform during the simulation. This is also confirmed by figs. 3.8b and 3.8c, which respectively show the averaged density $n_b(x)$ and temperature profile $T(x)$ in the bulk (symbols). The linear temperature profile perfectly overlaps with the theoretical

prediction $T(x) = T_c + x\nabla T$ and the bulk density shows an excellent agreement with the ideal gas equation

$$P_b = n_b(x)k_B T(x). \quad (3.15)$$

To recognise the dependence of $n_b(x)$ on different system parameters, eq. (3.15) needs to be rewritten in an alternative form. The uniform bulk pressure P_b is fixed by the conservation of particle number:

$$\int_0^{L_x} n_b(x) dx = \frac{P_b}{k_B} \int_0^{L_x} \frac{1}{T(x)} dx = \frac{P_b}{k_B \nabla T} \ln \frac{T_h}{T_c} = ML_x. \quad (3.16)$$

In terms of ∇T and $T(L_x/2) = T_0 = 1$, the bulk density $n_b(x)$ can be expressed as

$$n_b(x) = \frac{n_B}{1 + \frac{\nabla T}{T_0} \left(x - \frac{L_x}{2}\right)}, \quad (3.17)$$

where n_B , the central bulk density at $x = L_x/2$, is given by

$$n_B = \frac{ML_x \nabla T}{2T_0 \operatorname{arctanh}\left(\frac{L_x \nabla T}{2T_0}\right)}. \quad (3.18)$$

The interfacial layer of the colloid is hence in contact with a bulk density n_B that tends to zero in the limit where $L_x \nabla T / (2T_0) \rightarrow 1$. However, as the condition $T_c > 0$ implies that $L_x \nabla T / (2T_0)$ cannot exceed unity, varying either L_x or ∇T for our standard parameter choice requires that these parameters do not exceed $L_x = 200$ and $\nabla T = 0.03$. The reduction of n_B with increasing L_x or ∇T must also be taken into account when studying the parameter dependence of the forces on the colloid, which will be shown to scale linearly with n_B .

3.3 Forces on a Colloid inside an MPC fluid

As the thermophoretic force \mathbf{F}_T is the total force acting on the colloid, it can be expressed as the sum of a body force \mathbf{F}_ϕ , deriving from the interaction potential ϕ , and a surface force \mathbf{F}_S , resulting from the collisional interaction with the fluid. The surface force is defined as the integral of the hydrodynamic stress over the colloidal surface and therefore cannot be determined without an explicit expression of the stress tensor. However, the total body force can be determined by noticing that every fluid element exerts a body force $n(\mathbf{r})\nabla\phi(r)$ on the colloid, so that \mathbf{F}_ϕ takes the form of a volume integral over the interfacial layer:

$$\mathbf{F}_\phi = \int_R^\infty n(\mathbf{r})\nabla\phi(r) dV. \quad (3.19)$$

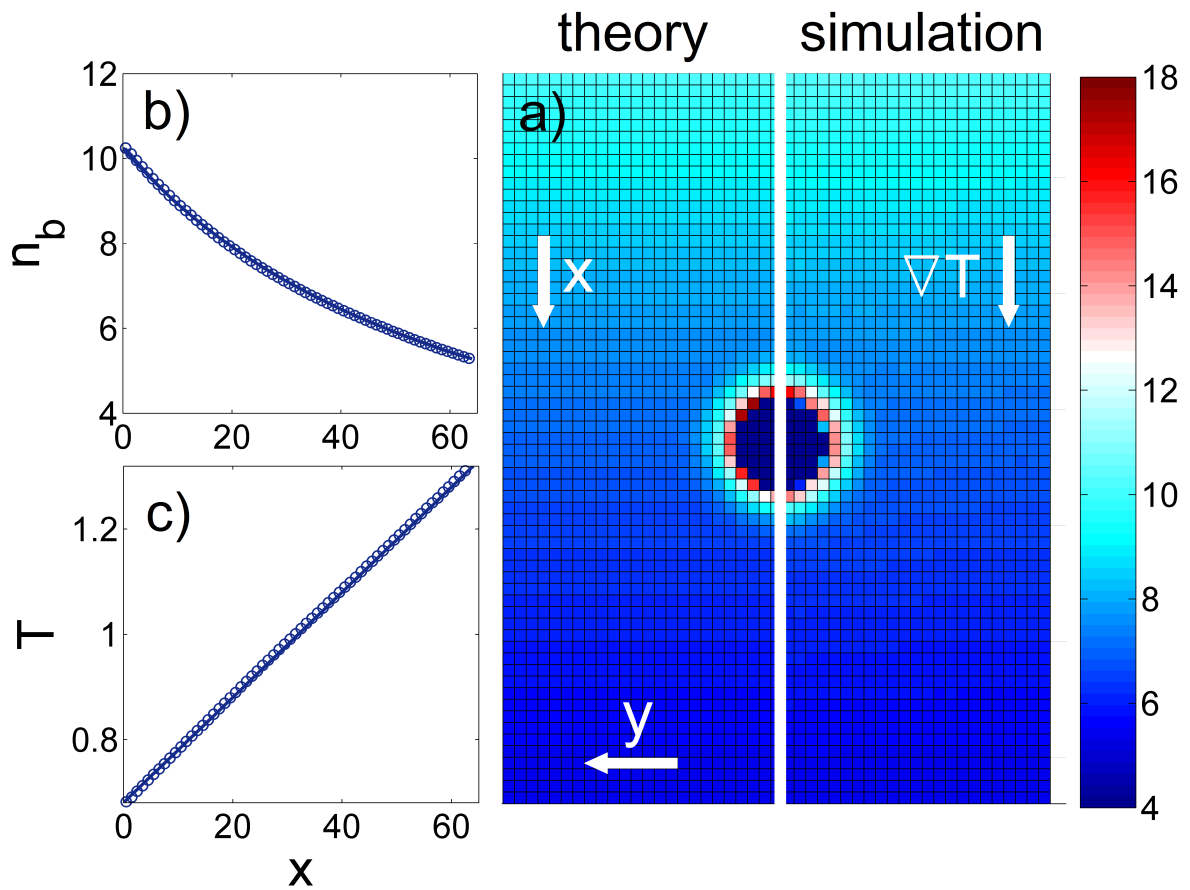


Figure 3.8: Steady-State of the MPC fluid around a colloid with a stick surface and an interfacial width $\lambda = 6$. All other parameters are set to their standard values. a) Histogram of measured fluid density profile (RHS) and theoretical prediction (LHS) in the xy -plane. b) Comparison between measured bulk density $n_b(x)$ (circles) and ideal gas equation (solid line). c) Comparison between measured bulk temperature $T(x)$ (circles) and theoretical prediction (solid line).

Under the condition that the interfacial layer is at thermodynamic equilibrium (ITE), the local density $n(\mathbf{r})$ of the MPC fluid around the colloid is further expected to follow the Boltzmann distribution

$$n(\mathbf{r}) = n_b(T(\mathbf{r})) \exp\left(-\frac{\phi(r)}{k_B T(\mathbf{r})}\right), \quad (3.20)$$

where $n_b(T(\mathbf{r})) = n_B T_0 / T(\mathbf{r})$.

If the density is assumed to be radially symmetric ($T(\mathbf{r}) = T_0$), it is easily verified that $\mathbf{F}_\phi = 0$, showing that \mathbf{F}_ϕ is a non-equilibrium component that specifically relies on the asymmetry in $n(\mathbf{r})$ induced by the local temperature variation $\delta T \sim \mathbf{r} \nabla T$. Although eq. (3.19) must be solved numerically for my choice of $\phi(r)$, it is clear that the direction of \mathbf{F}_ϕ is determined by the sign of the interaction: The colloid will feel a body force towards the colder and hence denser side of the layer ($\mathbf{F}_\phi < 0$) for attractive potentials ($\varepsilon < 0$) and a body force to the hotter and less dense side of the layer otherwise.

Unlike the body force, the thermophoretic force is evaluated to first order in the temperature gradient by assuming that the interfacial layer is radially symmetric. In view of eq. (2.44), the interfacial force density for a one-component fluid reads

$$\vec{\mathcal{F}}_\phi(r) = -q_\phi(r) \frac{\nabla T}{T} - n_\phi(r) \nabla_T \mu, \quad (3.21)$$

where μ is the ideal chemical potential of the MPC fluid. As ∇T and $\nabla_T \mu$ are independent thermodynamic forces, the condition of uniform pressure in the bulk directly implies that $\nabla_T \mu = 0$ and $H_b = \bar{H}$. For the MPC fluid, the partial molar enthalpy \bar{H} is thus equal to the total enthalpy per fluid particle in the bulk, given by $H_b = \frac{5}{2} k_B T$. It directly follows from eq. (2.45) that

$$h_\phi = h'_s = h_s - n H_b = \left(n \phi + \frac{5}{2} n k_B T \right) - \frac{5}{2} n k_B T = n \phi. \quad (3.22)$$

However, the local temperature gradient around the colloid may differ from the applied bulk gradient ∇T due to heat flows through the colloid and its interfacial layer. This issue was already briefly mentioned at the end of section 2.3.1, where the modification was said to stem from a difference between the thermal conductivities of the colloid and the fluid. In the simulated system, we are further confronted with the difficulty that the gradient can be disturbed by interfacial fluid flows and that the thermal conductivity of the MPC fluid depends on its density, resulting in a varying conductivity inside the layer. This leads to a complex modification of the local temperature profile, as evidenced in the right part of fig. 3.9a, which shows a histogram of the measured temperature around a colloid with a

slip boundary and an interfacial width of $\lambda = 6$. The blue rectangle indicates the central isothermal plane (CIP) inside the interfacial layer. The local temperature gradient $\nabla T(\mathbf{r})$ measured inside this plane as a function of radial distance from the colloid is shown in fig. 3.9b. It can be seen that $\nabla T(\mathbf{r})$ is reduced inside the layer but coincides with the imposed bulk gradient ∇T at larger distances. Local temperature modifications might be incompatible with my theoretical framework for two reasons. Firstly, the condition of ITE could be violated if the local gradient varies in both magnitude and direction. Secondly, the resulting interfacial heat density q_ϕ might not be radially symmetric and may no longer be equal to the interfacial excess enthalpy density h_ϕ . It is currently unclear how these local modifications could be properly incorporated into my theoretical framework without violating its underlying assumptions. To circumvent this issue, we shall instead evaluate eq. (2.57) using an approximate method, by defining an effectively uniform interfacial gradient ∇T_s that directly couple to the excess enthalpy density, such that

$$\vec{\mathcal{F}}_\phi(r) = -h_\phi(r) \frac{\nabla T_s}{T}. \quad (3.23)$$

More specifically, ∇T_s is determined from the simulation data by computing the average temperature gradient across the CIP inside the interfacial layer. The value of ∇T_s (red horizontal line in fig. 3.9b) lies right in-between the bulk gradient ∇T and the gradient $\nabla T(r=R)$ at the surface. Combining eqs. (3.23) and (3.22) with eq. (2.57), we obtain the final form for the thermophoretic force acting on a colloid in an MPC fluid:

$$\mathbf{F}_T = \frac{\nabla T_s}{T_0} \int_R^\infty n(r) \phi(r) \left(1 - b \frac{R}{r}\right) 4\pi r^2 dr. \quad (3.24)$$

In view of eqs. (3.24) and (3.19), both \mathbf{F}_T and \mathbf{F}_ϕ are indeed expected to scale linearly with the bulk fluid density n_B in the middle of the system. Further, a prediction for the surface force is now indirectly provided by $\mathbf{F}_S = \mathbf{F}_T - \mathbf{F}_\phi$. The theoretical prediction for \mathbf{F}_T is proportional to ∇T_s and its direction is determined by the sign of the interaction. Like the body force, the thermophoretic force is hence directed towards lower temperature for attractive potentials, corresponding to a thermophobic behaviour of the colloid. Despite the relatively simple form of $\phi(r)$, the integral in eq. (3.24) has to be solved numerically, hinting at a non-trivial dependence of \mathbf{F}_T on the parameters λ , ε and q . The numerical solutions for $\mathbf{F}_T(R)$ and $\mathbf{F}_T(\lambda)$ are displayed in fig. 3.10 for different values of q . The magnitude of \mathbf{F}_T increases with both R and λ but undergoes a steeper increase with λ than with R . Although these features are not directly visible in the graphs, it should be noted that $\mathbf{F}_T = 0$ for $\lambda = 0$ whereas $\mathbf{F}_T \neq 0$ for $R = 0$. We also see that \mathbf{F}_T decreases in magnitude with increasing q and that the magnitude for a slip boundary always exceeds the one for a stick boundary. The latter

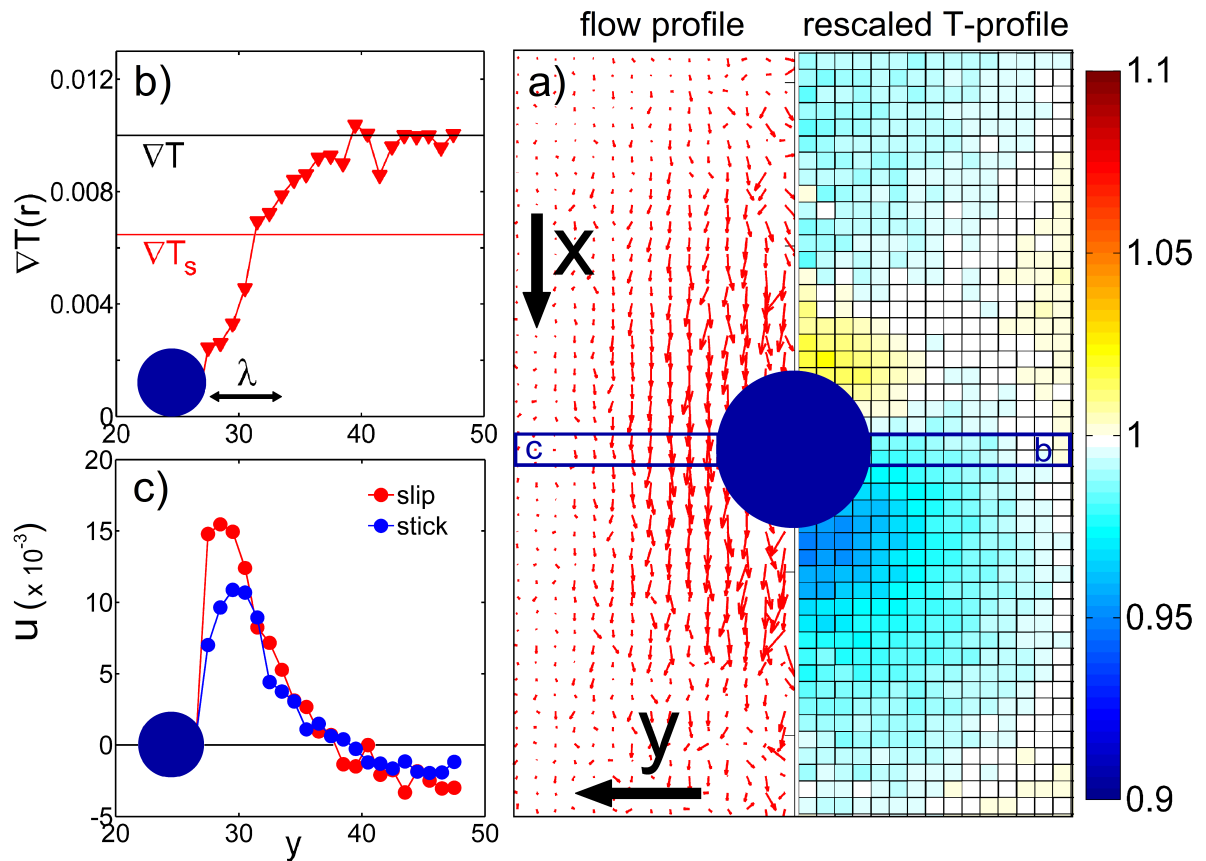


Figure 3.9: Local temperature changes and flow field around a colloid with a slip surface and an interfacial width $\lambda = 6$. All other parameters are set to their standard values. a) The right side of the symmetry axis shows the local temperature rescaled with respect to its bulk profile, whereas the left side shows the flow field. The blue rectangle designates the central isothermal plane (CIP). b) Local temperature gradient $\nabla T(r)$ inside CIP as a function of radial distance (red curve). The bulk gradient ∇T is shown by the black line and the red line indicates the value of ∇T_s obtained from averaging over the interfacial layer. c) Flow strength as a function of radial distance inside CIP, for a slip boundary (red curve) and a stick boundary (blue curve).

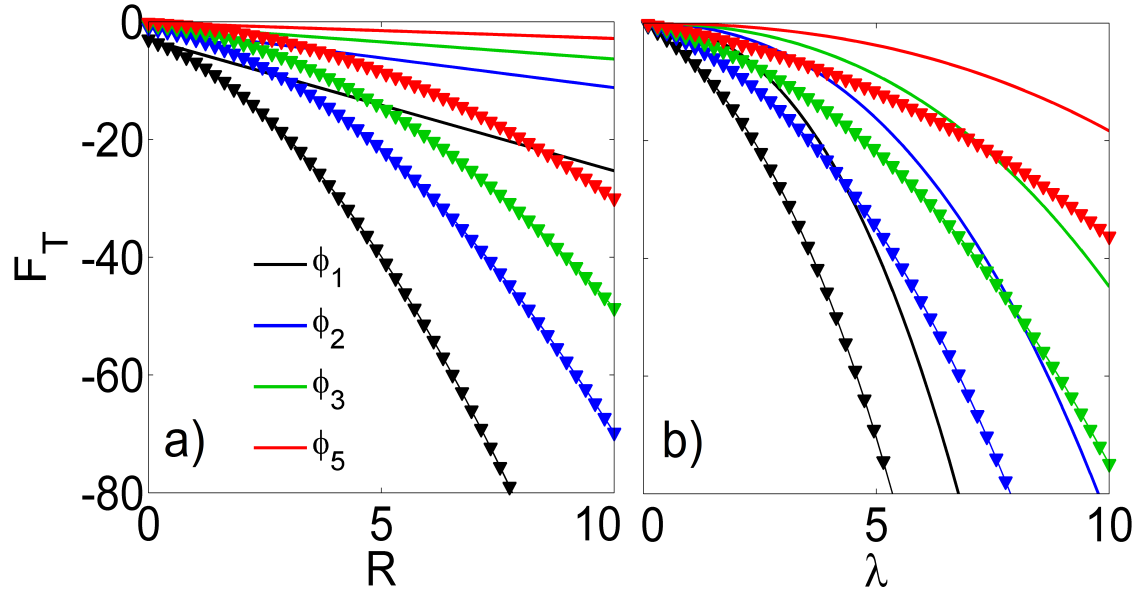


Figure 3.10: Theoretical prediction for the thermophoretic force based on eq. (3.24). a) \mathbf{F}_T vs R and b) \mathbf{F}_T vs λ for different values of q , using the standard parameter choice. Triangular symbols are used to distinguish between slip boundary (lines with triangles) and stick boundary (plain lines).

observation is evident from eq. (3.24), which shows that a switching from $b = 1$ to $b = 2/3$ results in a larger value of the hydrodynamic integral. As the potential ϕ is independent of colloidal size, \mathbf{F}_T is linear in R for all values of q when a stick boundary condition is applied, a trend that has previously been observed experimentally for charged colloids [10]. Before we may proceed to the simulation results, the range of validity of these theoretical predictions must however be addressed in more detail.

3.4 Validity of ITE: the Péclet Number

The hydrodynamic form of the thermophoretic force given by eq. (3.24) relies on interfacial thermodynamic equilibrium (ITE), which is expected to break down for excessively large temperature gradients or strong interfacial fluid flows. On one hand, ITE thus requires that the temperature variation across the colloid and its layer is small (thermal equilibrium), so that we need $d_\lambda |\nabla T| \ll T_0$, where $d_\lambda = 2(R + \lambda)$ is the effective diameter of the colloid and its layer. This condition is indeed satisfied for the standard choice of $R = 4$, $\lambda = 3$ and $\nabla T = 0.01$, but does not necessarily hold for the entire parameter space explored in the simulations. On the other hand, fluid advection can perturb both the temperature gradient and the chemical equilibrium inside the interfacial layer, resulting in a deviation of $n(\mathbf{r})$ from

its local Boltzmann distribution. A more quantitative measure for the strength of fluid flow relative to fluid diffusion is provided by the Péclet number, defined as

$$Pe = \frac{u_{\text{ad}}L}{D_s}, \quad (3.25)$$

where u_{ad} is a speed that expresses the typical flow strength of fluid advection. As a Péclet number much smaller than one is supposed to express the validity of ITE, the characteristic length scale L has to be defined carefully for our system. This can be achieved by noticing that ITE is preserved if the body force $-\nabla\phi$ that the colloid exerts on a fluid particle is much stronger than the frictional force γu_{ad} on that particle due to fluid flow. Using the Einstein relation $\gamma = k_B T_0 / D_s$ for the fluid friction coefficient γ and the value $-\nabla\phi(R) = q\varepsilon/\lambda$ as an estimate for $\nabla\phi$, we obtain the criterion:

$$Pe = \left| \frac{k_B T_0}{q\varepsilon} \frac{u_{\text{ad}}\lambda}{D_s} \right| \ll 1, \quad (3.26)$$

showing that $L = \left| \frac{k_B T_0}{q\varepsilon} \lambda \right|$ corresponds to the length over which the body force at the surface does an amount of work equal to $k_B T_0 = 1$. Being rather insensitive to fluid density, the self-diffusion coefficient D_s is evaluated from eq. (3.5) at the potential boundary $z = \lambda$ where $n = n_B$ and $T = T_0$, yielding a standard value of about $D_s \approx 0.67$. Hence, the only quantity in eq. (3.26) that needs to be determined by direct measurement is u_{ad} , which is taken to be equal to the maximal fluid flow speed inside the isothermal plane shown in fig. 3.9a. A typical flow profile around a colloid with a slip boundary is displayed in the left part of fig. 3.9a. The fluid inside the layer flows in the direction opposite to the thermophoretic force, and therefore to higher temperature for an attractive potential. Fig. 3.9c shows the flow speed as a function of radial distance inside the CIP. The maximal speed is reached close to the potential boundary and is higher for a slip boundary (red curve) than for a stick boundary (blue curve). The flow then decays away and finally changes direction at larger distances from the colloid, resulting in a weak back-flow in the bulk. As fluid advection tends to reduce the thermodynamic gradients across the layer [4], a Péclet number close to or larger than unity should always lead to a reduction of the measured force compared to its theoretical prediction.

Finally, we recall that eq. (3.24) is also based on the assumption that the fluid is incompressible. This criterion is fulfilled at small Mach number $Ma = u_{\text{ad}}/c_s$, which is defined as the ratio between the advective flow strength u_{ad} and the speed of sound c_s [38]. The speed of sound can be computed from the pressure using the relation $c_s = \sqrt{\partial P / m \partial n}$, which reduces to $c_s \sim \sqrt{k_B T / m}$ for the MPC fluid [67]. Inside the interfacial layer where $T = T_0$, the speed of sound is hence close to unity. As evidenced by fig. 3.9c, the flow

strength is usually of the order 10^{-2} , suggesting that MPC fluid flows can indeed be assumed incompressible.

3.5 Force Measurements

3.5.1 Measurement Technique

The forces on the colloid have been measured by recording the momentum transfer from fluid to colloid for each time step during the simulation. The thermophoretic force \mathbf{F}_T , the body force \mathbf{F}_ϕ and the surface force \mathbf{F}_S have all been measured independently by splitting the momentum transfer up into a potential and a collisional part, providing a consistency check for $\mathbf{F}_T = \mathbf{F}_\phi + \mathbf{F}_S$. The radial component of the surface force has also been measured separately, allowing a decomposition of \mathbf{F}_S into a pressure and shear component in the case of a stick boundary. It has further been verified that the y and z -components of all forces correctly average to zero, so that only the x -component along the temperature gradient is of interest.

The time evolutions of these forces along the temperature gradient for a stick boundary are shown in fig. 3.11, where each point corresponds to a local time average over 2×10^4 MPC steps. The weak variations in time suggest that the thermodynamic steady-state used for initialisation is close to the actual thermophoretic steady-state, allowing a rapid relaxation of the forces to their steady-state values. It can be seen that there is a difference of nearly one order of magnitude between \mathbf{F}_T (~ 10 units) and \mathbf{F}_ϕ and \mathbf{F}_S (~ 100 units). Both \mathbf{F}_T and \mathbf{F}_ϕ are negative (opposite to ∇T) whereas \mathbf{F}_S is positive (same direction as ∇T), as expected for $\varepsilon < 0$. Interestingly, \mathbf{F}_ϕ and \mathbf{F}_S seem to follow mirroring trends in time, suggesting a time correlation between body and surface forces inside the interfacial layer. We also note that the pressure and shear component have the same sign as \mathbf{F}_S . In general, the shear force is found to be smaller than the pressure force and can be switched off by changing from a stick boundary condition to a slip boundary condition at the colloidal surface. The MPC algorithm has further been tested by direct comparison to existing simulations in literature. An example of such a test simulation is shown in fig. (3.12), where I report an excellent agreement between my thermophoretic force measurement and a result obtained in [54]. The graph from [54] is less noisy because the displayed measurement is averaged over 19 independent runs, whereas my measurement has been obtained from a single run over a longer simulation time. The observed agreement is particularly astonishing considering that a different measurement technique was used in [54].

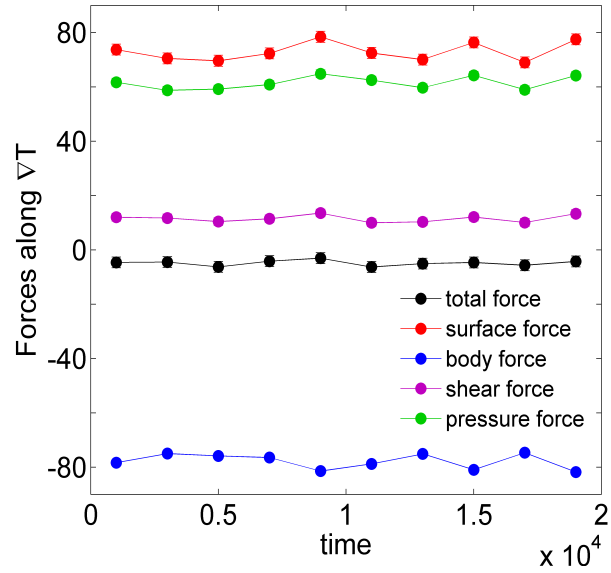


Figure 3.11: Time evolution of different force components acting on a colloid with a stick boundary, for the standard parameter choice.

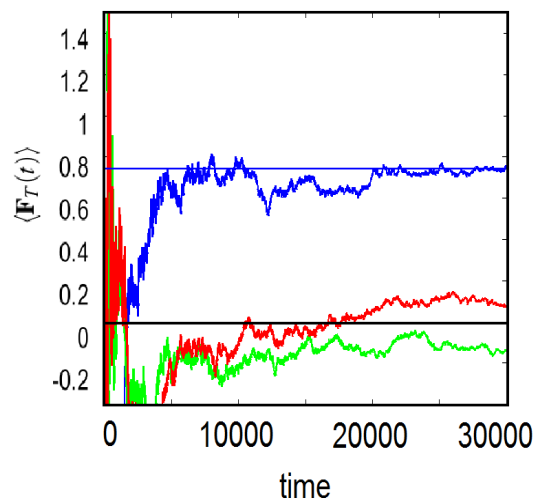


Figure 3.12: Convergence of the time-averaged thermophoretic force $\langle \mathbf{F}_T(t) \rangle$ as measured in my simulation, for the same MPC parameters as used for figure 5.6 on page 93 in [54].









	sim.		theory	
	F_T	F_ϕ	F_T	F_ϕ
stick				
slip				

Figure 3.13: Legend for main plots in figs. 3.14-3.17. Forces are distinguished by symbols, whereas boundaries conditions are distinguished by colour. Full symbols are used for simulation results and theoretical predictions are plotted with empty symbols connected by straight lines.

As eqs. (3.24) and (3.19) give precise theoretical predictions for the thermophoretic force and the body force, I will focus on the dependence of \mathbf{F}_T and \mathbf{F}_ϕ on different system parameters in the following analysis, by computing the net time-averages $\langle \mathbf{F}_{T,\phi}(t) \rangle$ of these forces over the simulation time. To facilitate the graphical presentation of my results, a separate legend for the data is shown in fig. 3.13.

3.5.2 Finite Size Effects

For an accurate comparison to theory, the force measurements have to be corrected for finite-size effects that result from hydrodynamic interactions between solid boundaries inside the system. These include the thermostats, the colloid and its mirror images due to periodic boundary conditions in y and z . Using the standard choice of system parameters, I have analysed the dependence of \mathbf{F}_T/n_B and \mathbf{F}_ϕ/n_B on the scaling factor R/L_x , which goes to zero at infinite system size. As shown previously, the bulk density n_B outside the interfacial layer tends to zero at constant ∇T when $R/L_x \rightarrow 0$. Unlike other finite-size corrections [54, 57], I have therefore chosen to study the evolution of $\mathbf{F}_{T,\phi}/n_B$ rather than $\mathbf{F}_{T,\phi}$, as increasing the system size naturally reduces the forces due to a depletion of bulk fluid in the centre of the system.

In fig. 3.14, it can be seen that the trends of $\mathbf{F}_{T,\phi}/n_B$ vs. R/L_x follow a linear relationship. Extrapolating the corresponding best-fit lines to $R/L_x = 0$ then allows the determination of $\mathbf{F}_{T,\phi}/n_B$ at infinite system size. In order to show all trends in a single graph, each data set in fig. 3.14 has been rescaled with respect to its limiting value at $R/L_x = 0$. As my simulations

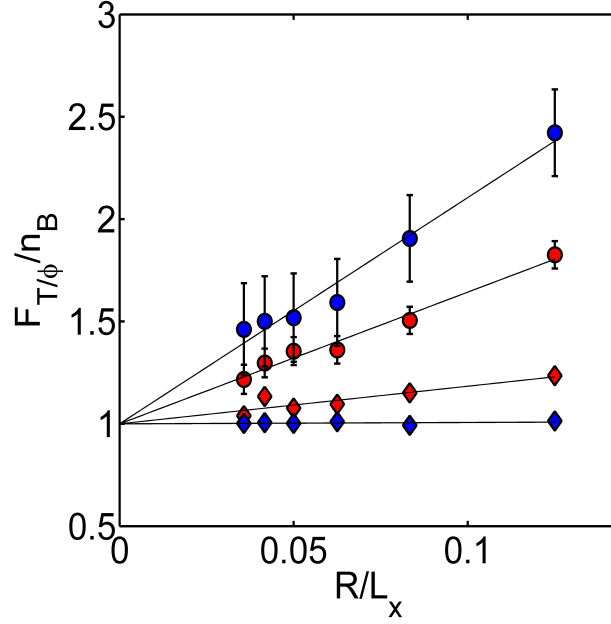


Figure 3.14: Dependence of \mathbf{F}_T/n_B and \mathbf{F}_ϕ/n_B on system size for the standard parameter choice.

have been performed with a standard scaling of $L_x = 16R$, the force $\mathbf{F}_{T,\phi}^\infty$ at infinite system size is related to the measured value $\mathbf{F}_{T,\phi}^{16}$ at $R/L_x = 1/16$ via

$$\mathbf{F}_{T,\phi}^\infty = \left(1 + \frac{\beta}{16}\right)^{-1} \mathbf{F}_{T,\phi}^{16} \quad (3.27)$$

where β are the slopes of the best-fit lines in fig. 3.14. Based on the corresponding values of β , we obtain the following scaling relations for the measured forces:

$$\mathbf{F}_T^\infty = \begin{cases} 0.59 \mathbf{F}_T^{16} & \text{stick,} \\ 0.71 \mathbf{F}_T^{16} & \text{slip,} \end{cases} \quad \mathbf{F}_\phi^\infty = \begin{cases} 1.00 \mathbf{F}_\phi^{16} & \text{stick} \\ 0.90 \mathbf{F}_\phi^{16} & \text{slip} \end{cases} \quad (3.28)$$

Hence, a measurement of forces at finite system size generally exceeds the expected value at infinite system size. It can further be seen that the correction in \mathbf{F}_T is more important for a stick boundary than for a slip boundary and that the body force \mathbf{F}_ϕ is rather insensitive to system size, showing that the above scaling relations capture the hydrodynamic character of the thermophoretic force at ITE. I now proceed to the presentation of my main simulation results, which concern the parameter dependence of \mathbf{F}_T and \mathbf{F}_ϕ and a direct comparison to my theoretical predictions. For this purpose, the force measurements have been rescaled

according to eqs. (3.28). It should however be noted that these scaling relations have been obtained for my standard choice of system parameters, corresponding to a weakly attractive potential that is reasonably short-ranged compared to the colloid size ($\lambda/q < R$). The scaling relations might therefore not be completely accurate for strongly attractive/repulsive or excessively long-ranged potentials. The theoretical predictions of \mathbf{F}_T and \mathbf{F}_ϕ have been evaluated for each simulation using the measured value of the interfacial temperature gradient ∇T_s . The trend of ∇T_s will be presented as an inset in the graph for the thermophoretic force \mathbf{F}_T , with the value of the bulk gradient ∇T indicated by a black line, and the Péclet number Pe will be shown as an inset in the graph for the body force \mathbf{F}_ϕ . Apart from the considered variable, all other parameters are set to their standard values. For convenience, I denote the theoretical prediction by $\mathbf{F}_{T,\phi}^{\text{th}}$ to distinguish it from the measured force $\mathbf{F}_{T,\phi}$.

3.5.3 Linearity in the Temperature Gradient

Let us first consider the dependence of $\mathbf{F}_{T,\phi}$ on the applied temperature gradient ∇T . The linearity of the thermophoretic force in ∇T , as predicted by NET, has recently been observed experimentally in aqueous suspensions of charged polystyrene colloids [15]. As the bulk density naturally decreases with ∇T in my simulations, I verify this linearity by considering the ratio $\mathbf{F}_{T,\phi}/n_B$, as shown in fig. 3.15 for a stick boundary. The interfacial temperature gradient ∇T_s is found to be equal to the applied gradient ∇T for the standard parameter choice. The linear increase of the Péclet number with ∇T stems from the linearity of the flow strength u_{ad} in the gradient. We notice that the theoretical predictions are proportional to ∇T_s , which is expected for \mathbf{F}_T^{th} from eq. (3.24), but which is less obvious for $\mathbf{F}_\phi^{\text{th}}$ based on eq. (3.19). Although there is a very good overall agreement between simulation and theory, deviations occur at larger gradients ($\nabla T > 0.02$), where the magnitude of the measured force exceeds the theoretical prediction. This feature can therefore not be explained by advective effects (large Pe), which should lead to a reduction of $\mathbf{F}_{T,\phi}$ compared to theory, but must be due to a departure from ITE caused by strong temperature variations across the layer. For $\nabla T = 0.03$, we find that $d_\lambda \nabla T_s \sim 0.4$, which is indeed a non-negligible temperature difference compared to the reference temperature $T_0 = 1$. A departure from the linear response regime of NET should hence be expected for excessively large temperature gradients.

3.5.4 Dependence on Colloidal Radius and Interfacial Width

The dependence of \mathbf{F}_T on colloidal radius R and interfacial width λ has attracted a lot of attention in research on thermophoresis as these parameters are relatively easy to tune

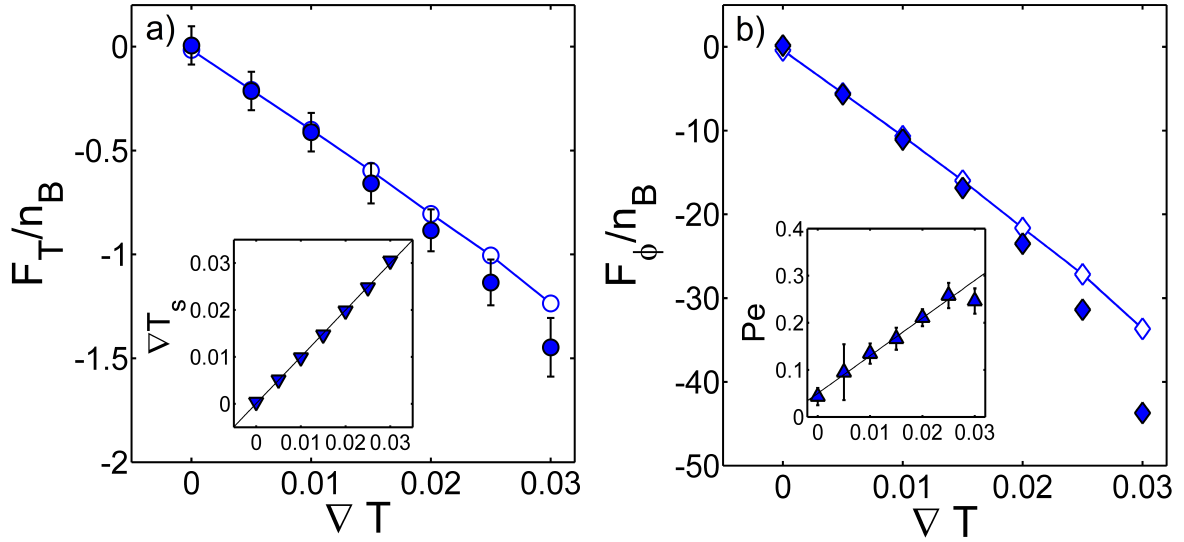


Figure 3.15: Dependence of forces on temperature gradient ∇T . a) F_T/n_B vs. ∇T and b) F_ϕ/n_B vs. ∇T . The black solid lines are linear fits to the corresponding data.

experimentally [10, 29, 70]. I have therefore carried out the simulation studies of these parameter dependences for both stick and slip boundary conditions.

As shown in fig. 3.16, I find a very good agreement between simulation and theory for both $F_T(R)$ and $F_\phi(R)$ in the case of a stick boundary. The inset in fig. 3.16a further suggests that the local temperature gradient is rather insensitive to R , such that $\nabla T_s(R) \approx \nabla T$ for stick. In particular, we note that the trend of F_T vs. R displays a linear relationship, which agrees with fig. 3.10 where I plotted the theoretical prediction for $\nabla T_s = \nabla T$, and which hence supports the linear trend reported for colloids in literature [10, 69, 90]. The excellent agreement for a stick boundary is further supported by low Péclet numbers that do not exceed 0.2. However, moderate deviations are observed for a slip boundary. Although simulation and theory still follow very similar trends, the force measurements are always slightly lower in magnitude. Moreover, we see a clear divergence between the measurements of F_ϕ for stick and slip, even though the body force should be independent of the boundary condition if the fluid is at ITE. These observations hint at a departure from ITE due to fluid advection. The Péclet number is indeed found to be higher for a slip boundary, which stems from the increase in flow strength when the boundary condition is changed from stick to slip. Furthermore, the advection of heat tends to weaken the interfacial temperature gradient compared to its bulk value, as evidenced by the trend of $\nabla T_s(R)$ for a slip boundary.

The influence of the interfacial width λ on the forces is presented in fig. 3.17. Unlike the theoretical prediction, the measured thermophoretic force is approximately linear and

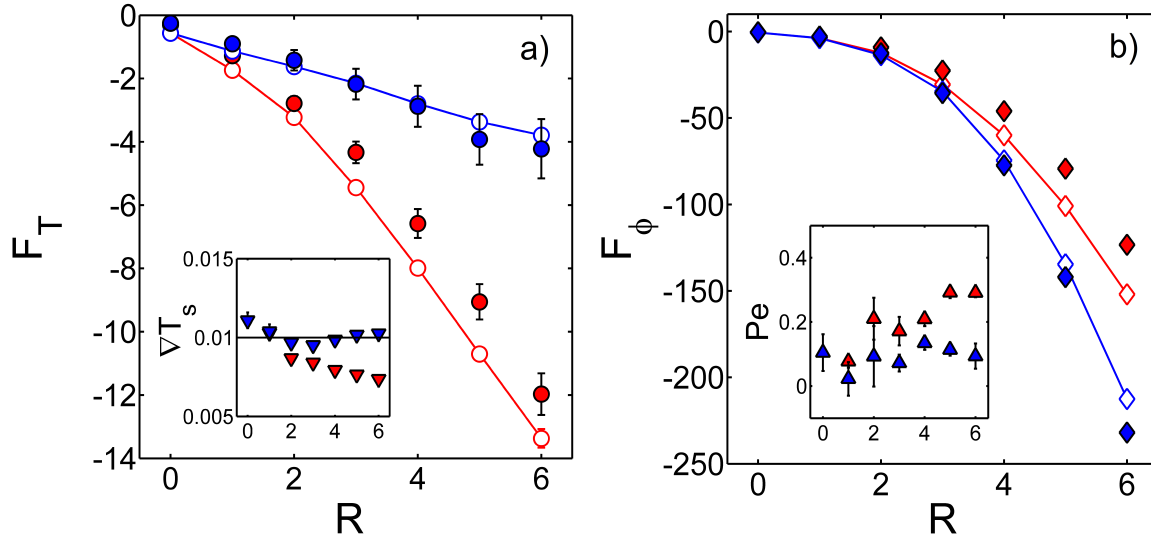


Figure 3.16: Dependence of forces on colloidal radius R . a) F_T vs. R and b) F_ϕ vs. R .

displays a reduced magnitude at larger values of λ for both stick and slip boundary conditions. This departure from the theoretical prediction is supported by increasingly large values of Pe . As the interfacial layer becomes wider, the body force acting on the fluid particles decreases and thus allows the layer to be more easily perturbed by interfacial fluid flows. Due to the drastic decrease of ∇T_s with λ , the increase in magnitude of F_T^{th} is also much slower than in fig. 3.10. Advective effects are again found to be more pronounced for slip than for stick, which agrees with my previous argument based on the change in flow strength. The deviations in the thermophoretic force occur at around $\lambda \gtrsim 5$ for stick and $\lambda \gtrsim 3$ for slip, corresponding to a Péclet number larger than 0.3. This suggests that $Pe \gtrsim 0.3$ constitutes a general limit above which advective effects become observable in F_T . We also notice that fluid advection has a stronger influence on the body force than on the thermophoretic force. The measured value of $F_\phi(\lambda)$ clearly differs from the prediction at large Péclet number and is even found to decrease in magnitude for a slip boundary. This is rather intuitively explained by the fact that the asymmetry of the layer, which gives rise to a body force, is more easily perturbed by advective flows than the radially symmetric part of the layer.

3.5.5 Influence of Potential Strength and Steepness

The dependence on potential strength is shown in fig. 3.18. A very good overall agreement between simulation and theory is confirmed by small Péclet numbers ($Pe < 0.2$). Although a stick boundary condition was applied at the colloidal surface, F_T is very well described

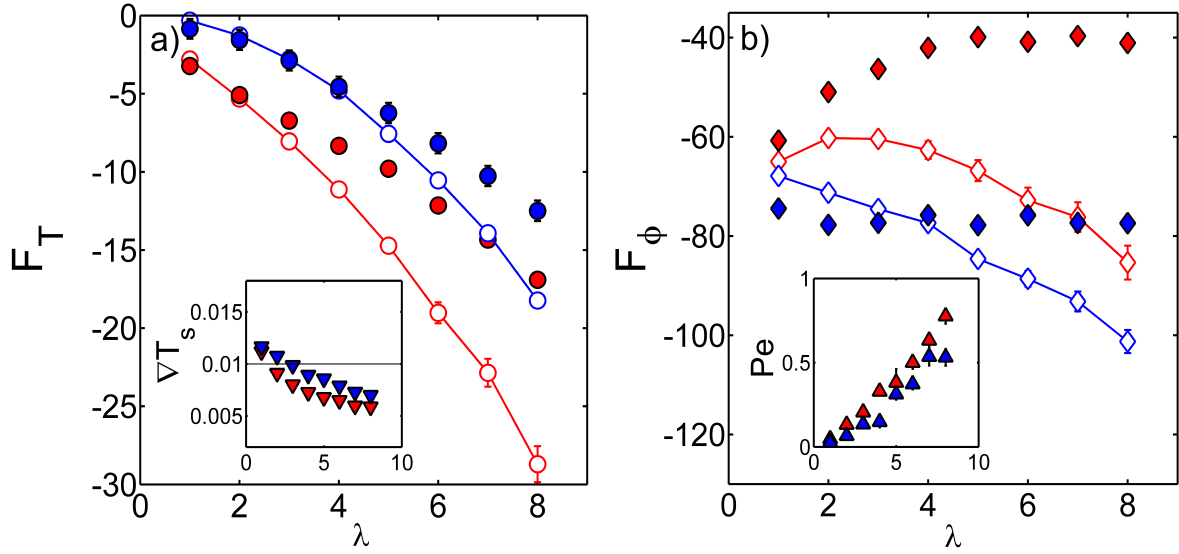


Figure 3.17: Dependence of forces on interfacial width λ . a) F_T vs. λ and b) F_ϕ vs. λ .

by the prediction for a slip boundary when $\epsilon > 0$, as an increasingly repulsive potential effectively leads to a slip boundary condition when fluid particles no longer directly collide with the colloid. I have therefore analysed the data for $\epsilon > 0$ accordingly, by evaluating $\mathbf{F}_T^{\text{th}}(\epsilon)$ with $b = 2/3$ and applying the corresponding scaling relations to the simulation results. A particularly interesting feature is the linear behaviour of the body force and interfacial temperature gradient for attractive potentials. A quasi-linear trend is also observed for the thermophoretic force in the range $-1 \leq \epsilon \leq 1$, with a sign switching from negative to positive occurring at $\epsilon = 0$ as expected.

The evolutions of the body force and surface force for increasingly repulsive potentials deserve particular attention and are therefore shown in fig. 3.19. It can be seen that the surface force vanishes beyond $\epsilon \approx 4$ due to the absence of direct collisions with the solid surface. For the body force, simulation and theory both reach a maximum at $\epsilon \approx 1.5$ followed by a slow decay, but start diverging from each other at larger ϵ despite small Péclet numbers. This suggests that the condition $Pe < 0.3$ does not guarantee the preservation of the gradient-induced asymmetry in the Boltzmann distribution that gives rise to a body force. It is also worth noting that the unscaled data conforms to $\mathbf{F}_\phi = \mathbf{F}_T$ when $\mathbf{F}_S = 0$, as required. This is however not the case for the rescaled data, implying that the finite-size correction for \mathbf{F}_ϕ is inaccurate for $\epsilon > 0$. We therefore conclude that the body force acquires a hydrodynamic character for increasingly repulsive potentials that cannot solely be described by a gradient-induced asymmetry in the local Boltzmann distribution. In this regime, the body force instead merges with the thermophoretic force, which is well described by the hydrodynamic form for

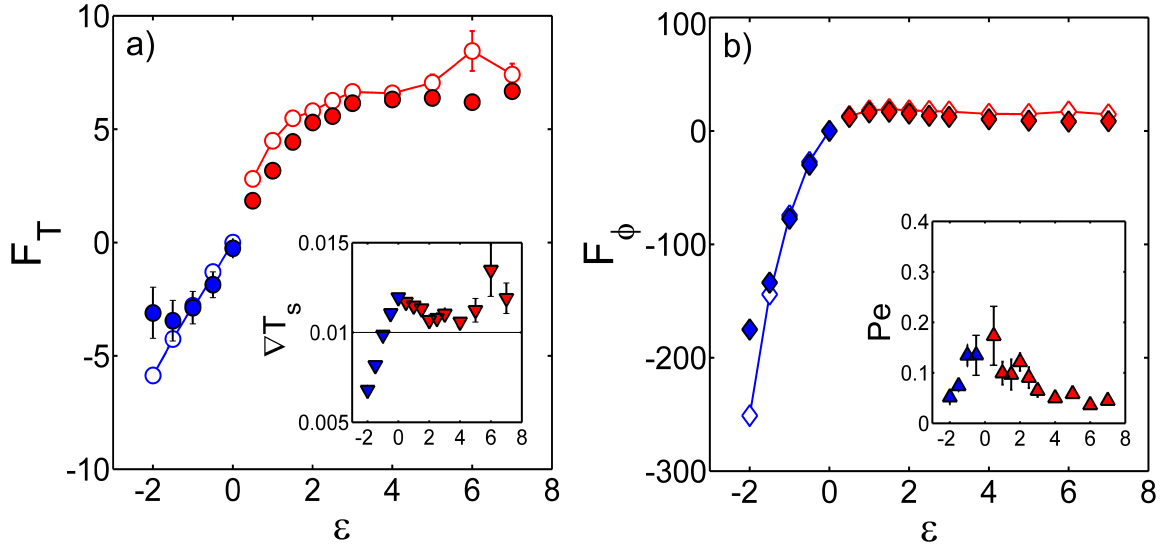


Figure 3.18: Dependence of forces on potential strength ε . a) \mathbf{F}_T vs. ε and b) \mathbf{F}_ϕ vs. ε .

a stick boundary, as given by eq. (3.24). This force is further expected to vanish in the limit $\varepsilon \rightarrow \infty$ when the potential interaction is effectively reduced to a slip-surface at a distance $r = R + \lambda$ from the colloidal centre.

The influence of potential steepness on the forces is presented in fig. 3.20. As reducing q has a similar effect on the shape of $\phi(r)$ as increasing λ , I have studied the dependence of the forces on the inverse of q . For the thermophoretic force, simulation and theory are quasi-linear and coincide within errors except for $q = 1$, where $Pe > 0.3$. The increase of the thermophoretic force with $1/q$ agrees with the trend previously observed in fig. 3.10. It can also be seen that ∇T_s decreases linearly with $1/q$ whereas Pe follows a linearly increasing trend. The body force \mathbf{F}_ϕ is found to be approximately constant and close to the theoretical prediction. However, a plot of $\mathbf{F}_\phi^{\text{th}}$ for $\nabla T_s = \nabla T$ (blue curve in 3.20b) displays a steep increase in magnitude, suggesting that the observed constancy of \mathbf{F}_ϕ is solely due to the strong reduction of ∇T_s with $1/q$. A comparison between figs. 3.20 and 3.16 shows that the parameters $1/q$ and λ indeed have similar effects on the forces, as suggested by my argument based on the shape of the potential. From these trends we thus conclude that, although the forces on the colloid are generally expected to increase with the range of the potential, an increase in the quantity λ/q also leads to stronger fluid advection that tends to reduce the magnitude of these forces.

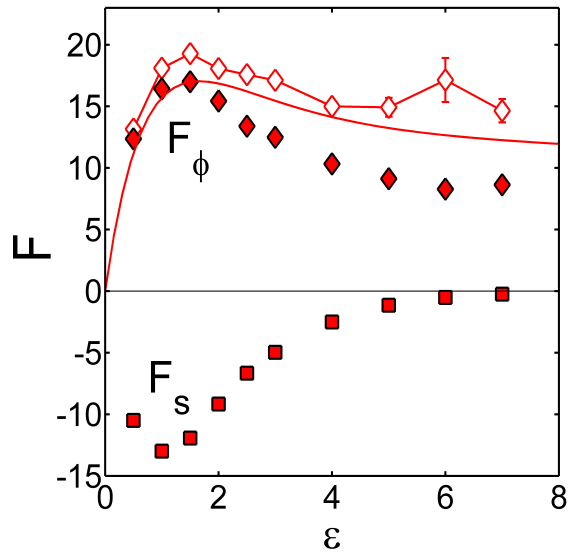


Figure 3.19: Evolution of body force \mathbf{F}_ϕ and surface force \mathbf{F}_s in the range $\varepsilon > 0$. The smooth red curve shows the theoretical prediction $\mathbf{F}_\phi^{\text{th}}$ for $\nabla T_s = \nabla T$.

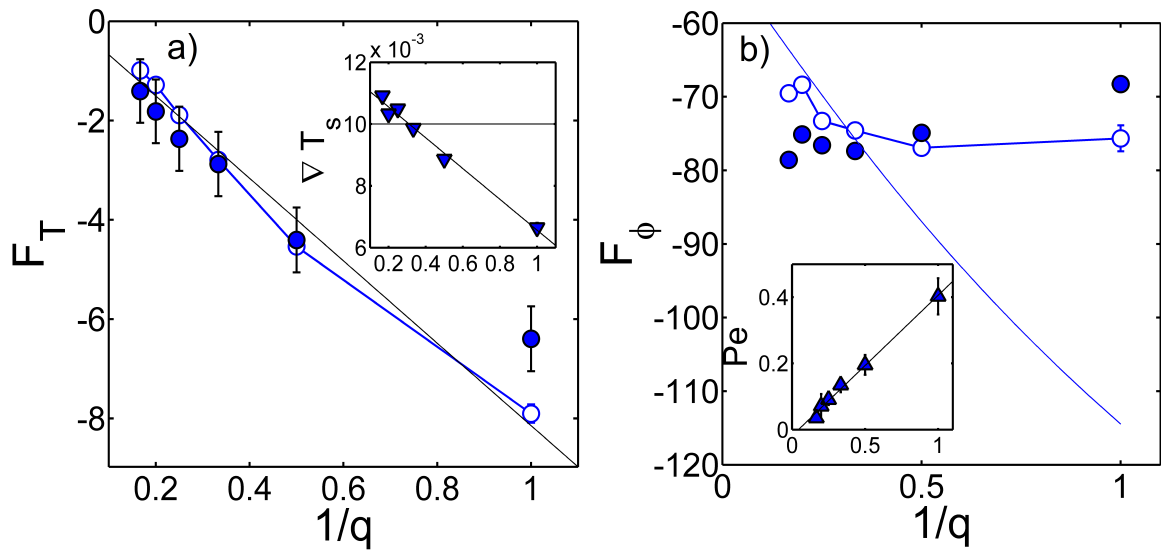


Figure 3.20: Dependence of forces on the inverse of potential steepness q . a) \mathbf{F}_T vs. $1/q$ and b) \mathbf{F}_ϕ vs. $1/q$. All solid lines are linear fits apart from the blue curve in the main plot of b), which shows $\mathbf{F}_\phi(1/q)$ for $\nabla T_s = \nabla T$.

3.6 Conclusion

In this chapter, I have used Multi-Particle Collision Dynamics to simulate colloidal thermophoresis on a mesoscopic scale, showing that a favorable comparison between simulation and theory relies on a detailed analysis of fluid properties at the colloidal interface. My simulation results show that the forces are indeed linear in the gradient as long as the temperature variation across the interfacial layer is weak. The introduction of the Péclet number has allowed me to quantify deviations from my theoretical predictions due to advective effects, showing that the criterion $Pe < 0.3$ is generally a good indicator for interfacial thermodynamic equilibrium of the MPC fluid around the colloid. The body force is particularly sensitive to fluid advection, suggesting that the asymmetry of the interfacial layer is more easily perturbed by advection than its radially symmetric part. It has further been shown that repulsive potentials lead to an effective slip boundary condition at the colloidal surface. Increasing the interfacial width and decreasing the potential steepness have similar effects, yielding larger predicted values on one hand, but reducing the force due to advection on the other hand. Most notably, the thermophoretic force has been found to scale linearly with the colloid radius for a stick boundary, a trend that conforms to my theoretical prediction and that has been observed experimentally for charged colloids in aqueous electrolyte solutions.

The excellent agreement between simulation and theory at low Péclet numbers is mainly due to the well-defined physical properties of the considered system, especially the equation of state of the MPC fluid and the simple surface properties of the spherical colloid. Although my theoretical model can in principle also be applied to more complicated colloidal suspensions encountered in real experiments, the main challenge in such experiments is to pin down all interactions that contribute to the interfacial excess enthalpy density and to identify the appropriate boundary conditions at the colloidal surface. This becomes a particularly challenging task when the colloids are coated with molecular surface groups that may change the hydrodynamic boundary conditions and whose interactions with the fluid give additional contributions to the net Soret coefficient. In my final chapter, I will therefore present experiments on functionalised colloids whose interaction with the fluid is no longer sufficient to explain the observed thermophoretic motion.

Chapter 4

Experiment

In this final chapter, I present thermophoretic measurements in aqueous suspensions of colloids with different surface coatings. Thermophoresis is commonly measured indirectly using advanced laser techniques such as Thermal Lensing [77], Beam Deflection [49], Digital Interferometry [60] or Forced Rayleigh Scattering [83], although it has been questioned to what extent these techniques may suffer from undesirable effects such as local heating or convection [71]. Recently, a direct measurement of thermophoretic forces on a single colloidal particle in confinement has further been achieved by means of evanescent light scattering [39]. Here, I employ an alternative technique based on the observation of the colloidal steady-state distribution in a closed cell, using conventional bright-field microscopy. This method avoids laser-induced convection or local heating and has the advantage of capturing all single-colloid and collective contributions to thermophoresis. Furthermore, I also study the motion of colloids during the relaxation to steady-state and propose a theoretical model to describe this relaxation more quantitatively.

4.1 Experimental Technique

4.1.1 Materials and Methods

I have performed thermophoretic measurements in aqueous suspensions using three different polystyrene (PS) particles of varying negative charge, size and surface coating, including Streptavidin (PS-STV, from microParticles GmbH), Polyethylenglycol-azide groups (PS-PEG-N₃, in house) and Polyethylenglycol-DNA (PS-PEG-DNA, in house [97]). The PS particles and their surface groups are shown in fig. (4.1). The particles are either dispersed in deionised water (ACROS Organics, Fisher Scientific), abbreviated as DiW, or custom-made Tris-EDTA (TE) buffer (10 mM Tris-HCl and 1 mM disodium EDTA at pH 8.0, in

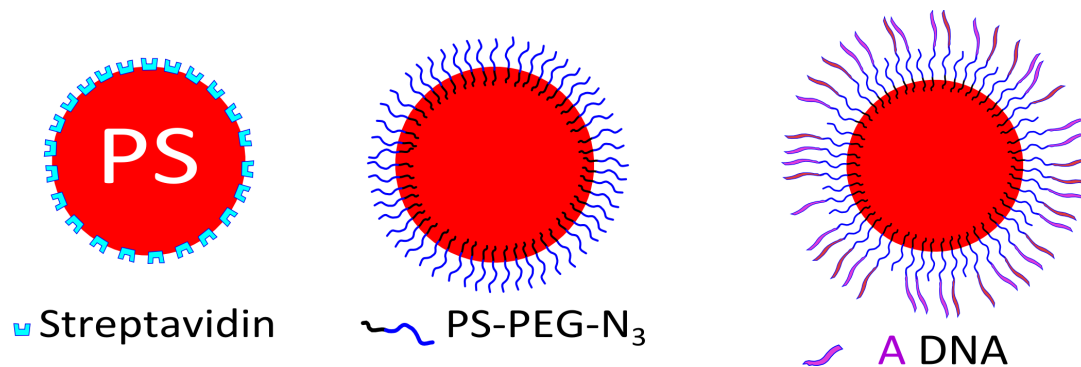


Figure 4.1: Schematic representation of the PS colloids and their surface groups.

house), and diluted down to volume fractions of about 0.01%. The reason for using PS is because it has a mass density similar to water (1040kgm^{-3}), so that micron-sized PS particles do not completely settle down due to gravitational sedimentation. Before each experiment, the suspensions were sonicated for 20 minutes to break up potential aggregates. The hydrodynamic diameters d_h and zeta potentials ζ of the PS particles have been obtained from Dynamic Light Scattering (DLS) measurements using a Zetasizer (Nano ZS, Malvern).

A schematic diagram of the setup is shown in fig. 4.2. The cell for the suspension is made of an ultra thin silicone spacer with a circular hole ($\sim 170\mu\text{m}$ thick, from Silex Silicones LTD), sandwiched between two sapphire windows ($32 \times 37 \times 0.50\text{mm}$, from UQG Optics). Sapphire is optically transparent and a very good heat conductor, thus guaranteeing a uniform temperature gradient inside the sample. Upon contact, the silicone film immediately sticks to the sapphire window due to strong adhesion forces. A droplet of the suspension ($\sim 25\mu\text{L}$) is then introduced and the second window is carefully placed on top of the spacer. Moderate pressure is exerted on the top window to squeeze out any excess liquid and to amplify the adhesion between the windows. The sample is then transferred to a Nikon Eclipse Ti-E inverted microscope, equipped with a Ximea MQ013MG-E2 camera with a E2V EV76C560 CMOS sensor. An extra-long working distance objective is used for bright-field imaging, with a numerical aperture of 0.60, corresponding to a depth of focus of about $\sim 1.3\mu\text{m}$. The sample is then mounted onto the microscope stage and sandwiched between two copper blocks. Both blocks are connected to PID (proportional integral derivative) controllers and have small central holes for the transmission of light. To avoid large-scale convection, a uniform temperature gradient is set up vertically by heating at the top and cooling at the bottom. For this purpose, the top and bottom blocks are connected to an electric heater and a water bath; and the corresponding temperatures are monitored using thermocouples. The time evolution of the colloidal concentration profile is captured by acquiring images of horizontal slices in 10 minute intervals, spanning the entire height of the cell. The slices are

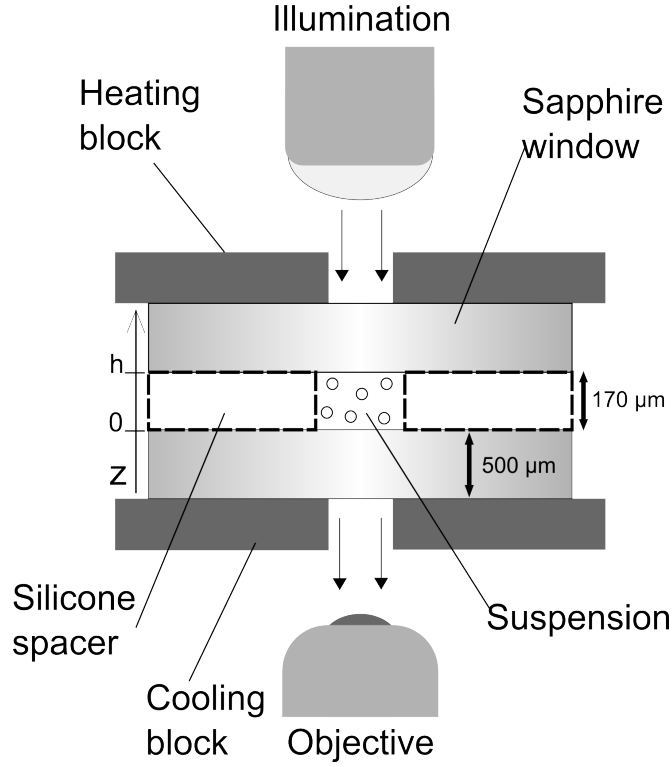


Figure 4.2: Lateral view of the experimental setup (dimensions are not to scale).

all equally spaced by a vertical distance of $\sim 10\mu\text{m}$ and averaged over multiple images to improve the accuracy of the measurement.

4.1.2 Steady-State Measurements

My experimental technique is based on eq. (1.5), which shows that the Soret coefficient S_T can be determined from the colloidal concentration profile at steady-state when the temperature gradient is known. In dilute suspensions, colloidal pair-interactions can be neglected and the Einstein relation $\xi D = k_B T$ can be used to relate the diffusion coefficient D to the friction coefficient ξ of the colloid. A single colloid is then subjected to two different forces, the thermophoretic force $\mathbf{F}_T = -k_B T S_T \nabla T$ and the gravitational pull $\mathbf{F}_g = m_r \mathbf{g}$ where $g = 9.81 \text{ m s}^{-2}$. The reduced mass m_r of the colloid is given by $m_r = V_c (\rho_c - \rho_w)$, where V_c is the volume of a colloid and ρ_c and ρ_w are the pure mass densities of the colloid (PS) and solvent (water), respectively. Taking into account the gravitational pull of the suspended particle, the colloidal distribution along the temperature gradient can hence be written as

$$\frac{\partial \ln P(z)}{\partial z} = \frac{F_g}{k_B T} - S_T \frac{\partial T}{\partial z}. \quad (4.1)$$

	PS-STV	PS-PEG-N ₃	PS-PEG-DNA
d_h (nm)	591	446	491
D ($\mu\text{m}^2\text{s}^{-1}$)	0.84	1.11	1.01
τ_D (h)	4.78	3.62	3.97

Table 4.1: The values of D are determined from the Stokes-Einstein relation at room temperature, using the values of the hydrodynamic diameters d_h .

Here, the colloidal concentration $c(z)$ has simply been replaced by its corresponding probability distribution $P(z)$.

In my experiments, I have measured the colloidal concentration profile at steady-state for different temperature gradients, keeping the bottom block at $\sim 20^\circ\text{C}$ and raising the temperature of the upper block to a maximum of $\sim 50^\circ\text{C}$. Within this narrow temperature range, the expansion of water barely effects the reduced mass of the colloid and the thermal energy $k_B T$ can be assumed constant throughout the sample. In view of eq. (4.1), the Soret coefficient S_T can then be identified as the negative slope of the curve defined by $\partial \ln P / \partial z$ vs $\partial T / \partial z$, allowing a natural elimination of the gravitational pull as a constant offset at $\partial T / \partial z = 0$. It is important to note that the colloids must be at steady-state before this measurement technique for S_T is applied. An order of magnitude estimate for the relaxation time required to reach this steady-state is given by the diffusive time scale $\tau_D \sim h^2 / 2D$, where h is the cell height set by the thickness of the silicone spacer. The diffusion coefficient can be determined from the Stokes-Einstein relation $D = k_B T / (3\pi\eta d_h)$, where the viscosity of water takes the value of $\eta = 8.9 \cdot 10^{-4} \text{Pa}\cdot\text{s}$ at room temperature. The values of d_h , D and τ_D are reported in Table 4.1, showing that all examined colloids are expected reach steady-state on a time scale of 4-5 hours.

The local concentration at each altitude is determined via image analysis using a home-developed MATLAB code, based on a binarisation method with a high pass filter for contrast and feature size. The images are acquired in bright-field and have a size of 1024^2px^2 . As shown in fig. 4.3a, the colloids appear as black blobs on a grey background. The image is inverted and split into smaller bins of 64^2px^2 inside which the background illumination can be assumed uniform. Each bin is then binarised according to a contrast parameter f , which defines the binarisation threshold B as

$$B = \min \left\{ 1, \left(1 + \frac{f}{100} \right) I \right\}, \quad (4.2)$$

where I is the mean intensity of the bin. All pixels are set to 1 (white) above this threshold and to 0 (black) otherwise. As the mean intensity of a white bin cannot exceed

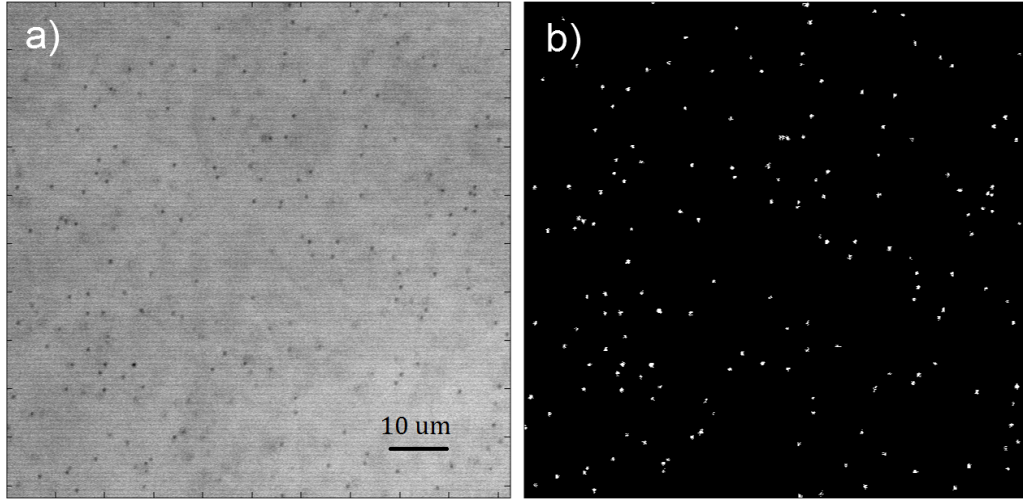


Figure 4.3: Comparison between raw and binarised image.

1, the binarisation threshold is automatically cut off at this value. The remaining features are sent through a high pass filter to eliminate background noise. The white features in the binarised image, shown in fig. 4.3b, display an excellent agreement with the colloids that are visible in the raw image (fig. 4.3a). The reason for binarising each bin rather than the entire image is that the illumination is never completely uniform over the image, even if the optics is properly aligned. This effect can be seen in fig. 4.4, which shows the area fraction of detected features in each bin before the high pass filter is applied. Direct binarisation of the whole image results in a non-uniform scatter of area fractions, whereas binarising each bin separately leads to a uniform scatter.

The complete relaxation to steady-state is verified by monitoring the time evolution of the decay parameter $\kappa(t)$, which we define as the negative slope of the best-fit line to the curve $\ln P(z)$ vs z :

$$\kappa(t) = - \left\langle \frac{\partial \ln c(z)}{\partial z} \right\rangle_z (t). \quad (4.3)$$

Examples of these time evolutions are shown in fig. (4.5), for PS-PEG-N₃ and PS-STV in DiW. For both systems, $\kappa(t)$ reaches a stable value after around 4 hours, which indeed falls into the range of values for τ_D given in Table 4.1. The local concentration $c(z)$ of colloids is further related to the area fraction $\phi_a(z)$ via $c(z) = \phi_a(z)/(A_c l)$, where A_c is the average feature size of a colloid and l is the observed depth of the image. We can thus write:

$$- \frac{\partial \ln c(z)}{\partial z} = - \frac{\partial \ln \phi_a(z)}{\partial z} + \frac{\partial \ln A_c l}{\partial z}. \quad (4.4)$$

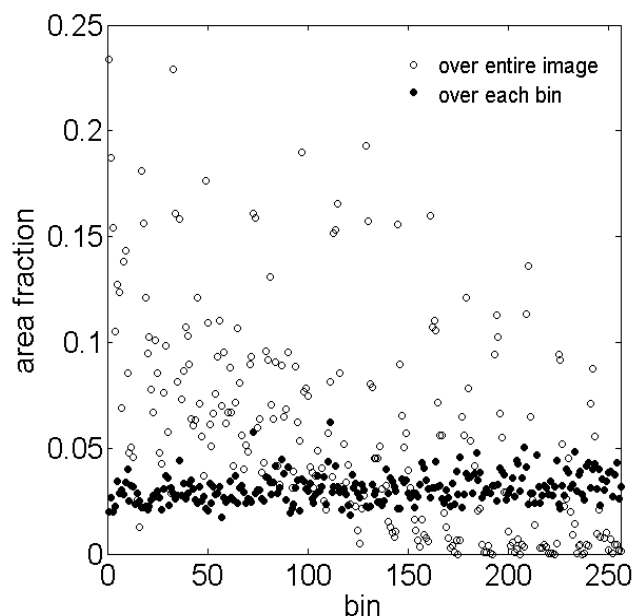


Figure 4.4: Scatter plot of detected area fraction per bin. Empty circles show the non-uniform distribution obtained by binarisation over the entire image, whereas full circles show the uniform distribution obtained by binarisation of each bin.

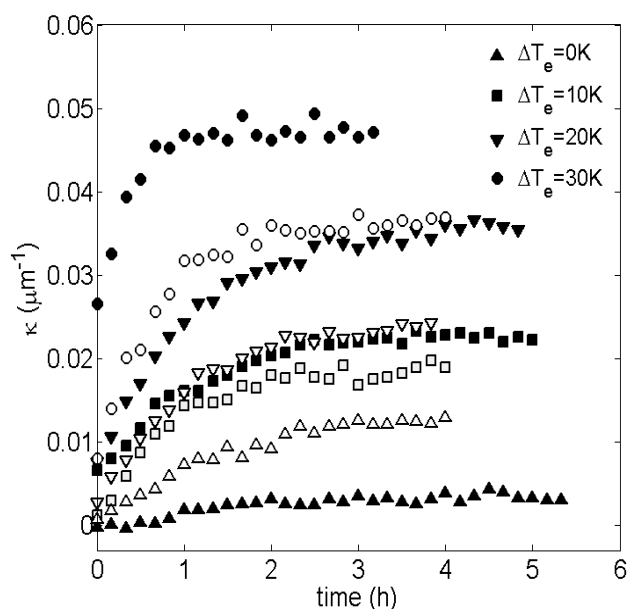


Figure 4.5: Time evolution of the decay parameter $\kappa(t)$ for PS-PEG- N_3 (full symbols) and PS-STV (empty symbols) in DiW, for varying external temperature differences ΔT_e . The time origin is not absolute, but set to zero at the start of each measurement.

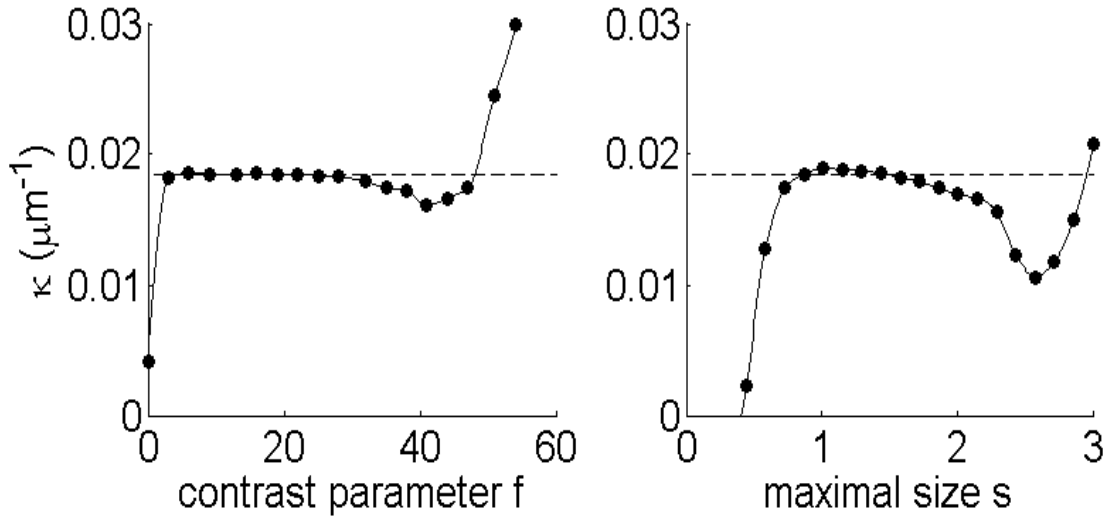


Figure 4.6: Dependence of κ on the contrast parameter f and maximal feature size s . The dashed horizontal line shows the value of κ determined with the chosen parameters.

As our examined suspensions are very dilute, the overall intensity of the image does not change with height. Although A_c and l depend on the binarisation parameters, this implies that A_c and l are independent of z , giving:

$$-\frac{\partial \ln c(z)}{\partial z} = -\frac{\partial \ln \phi_a(z)}{\partial z}, \quad (4.5)$$

so that we can directly use the measured area fraction to determine the Soret coefficient. The contrast parameter f and maximal size s for the high pass filter are calibrated by analysing the behaviour of $\kappa = \kappa(t \rightarrow \infty)$ over a physical range of these parameters. Examples of such calibration curves are shown in fig. 4.6. These curves display a stable value of κ over a wide range of parameter values. Divergences are only visible when the parameters take unphysical values, leading to a high noise level at very low f and s , and a shortage of detections for exceedingly large values of f and s . The value of κ is then determined with an optimal parameter choice within the stable range.

4.2 Steady-State Measurement Results

The rigorous image analysis technique presented in the previous section allows an accurate measurement of the colloidal concentration profile at steady-state. Fig. (4.7) shows the plots of $\ln P(z)$ vs z at steady-state for PS-PEG- N_3 and PS-STV in DiW. It can be seen

that the concentration of colloids is highest at the bottom of the cell and falls off rapidly towards the top. The lines represent best fits to the data over the range of 30-100 μm above the bottom surface. The reason for limiting the fitting to this bulk range is twofold. Apart from colloidal absorption, which tends to be stronger at the bottom due to gravity, lower concentrations give poor statistics close to the top surface. The absence of colloids tends to reduce the slope of the curves at the top of the cell, where the area fraction of detected features is mainly set by a constant level of background noise. This effect is visible in fig. 4.7 at higher altitudes and becomes more pronounced with increasing temperature difference. Although it cannot be ruled out that this systematic deviation might partly stem from a weak temperature dependence of the Soret coefficient, the curves undoubtedly show that $\ln P(z)$ is linear over a wide range inside the cell. In view of eq. (4.1), this linearity implies that the Soret coefficient S_T is approximately constant throughout the suspension, meaning that the colloids are subjected to a uniform thermophoretic force. At steady-state, the decay parameter κ can thus be related to the Soret coefficient via

$$\kappa = S_T \nabla T + \kappa_g, \quad (4.6)$$

where $\kappa_g = -F_g/(k_B T)$.

Knowing the cell height and the internal temperature difference ΔT_i inside the suspension, S_T can hence be determined from

$$S_T = h \frac{\partial \kappa}{\partial \Delta T_i}, \quad (4.7)$$

where h is the cell height. The internal temperature difference ΔT_i differs from the externally applied difference ΔT_e due to the finite thermal conductivity of sapphire. By treating the sapphire windows and suspension as conducting elements in series, it can be shown that (see appendix D):

$$\Delta T_i = \frac{1}{1 + 2 \frac{\sigma_w h_s}{\sigma_s h}} \Delta T_e, \quad (4.8)$$

where $h_s = 0.5 \text{ mm}$ is the thickness of a sapphire window and $\sigma_s = 27.21 \text{ Wm}^{-1}\text{K}^{-1}$ and $\sigma_w = 0.6 \text{ Wm}^{-1}\text{K}^{-1}$ are the thermal conductivities of sapphire and water, respectively. Using these values, we obtain the relation

$$\Delta T_i = 0.88 \Delta T_e. \quad (4.9)$$

The plots of κ vs ΔT_i are shown in fig. 4.8 for all studied systems. It should be noted that the measurements on PS-STV were performed on different samples, explaining the higher

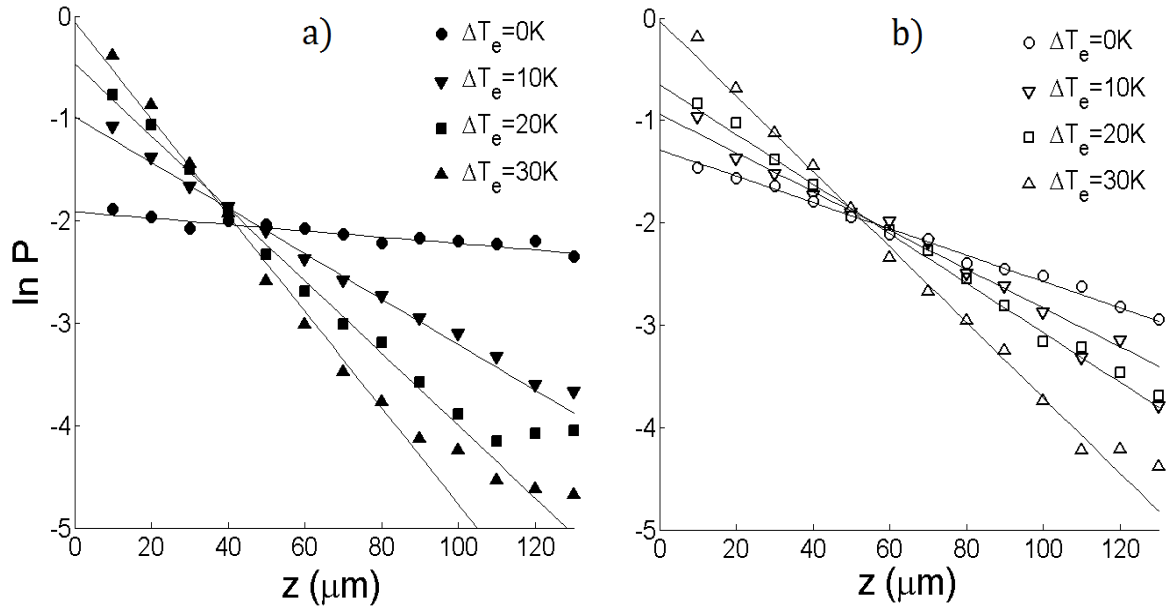


Figure 4.7: Natural logarithm of probability $P(z)$ vs altitude z for varying external temperature differences ΔT_e , for a) PS-PEG- N_3 and b) PS-STV, in DiW. The probability $P(z)$ is normalised according to $P(z_i) = c(z_i)/\sum_i c(z_i)$, where z_i are the discrete altitudes inside the bulk range.

noise level in fig. 4.8a. The relative sample error associated with these measurements is 7% and is likely due to a fluctuating pH in DiW. It can be seen that $\kappa(\Delta T_i)$ is approximately linear for each system, indicating that the thermophoretic force is linear in ∇T and that the Soret coefficient is rather insensitive to temperature. The values of S_T obtained from eq. (4.7) are also displayed in fig. 4.8 and are exclusively positive, corresponding to a thermophobic behaviour of all studied PS particles. The values of S_T measured in DiW deserve particular attention, as they do not conform with existing theoretical predictions for charged colloids in aqueous electrolyte solutions [68, 90]. These models are based on eq. (2.113) and only account for the electric double layers around the colloids, yielding a scaling $S_T/d_h \propto \zeta^2/3 + \zeta V_T/e$, where e is the elementary charge. The first term stems from the interfacial excess enthalpy whereas the second term accounts for a thermoelectric potential V_T . For comparison, the measured values of S_T/d_h and ζ in DiW are given in Table 4.2. Although the value of ζ may fluctuate in DiW ($\pm 5\text{mV}$), these measurements show that PS-PEG- N_3 clearly has the weakest zeta potential. This is mainly due to the azide (N_3) groups on the colloidal surface. Unlike DNA, which carries a net negative charge, the azide groups are neutral and therefore reduce the zeta potential by shifting the hydrodynamic slip plane away from the charged surface. Nonetheless, the ratio S_T/d_h has been found to

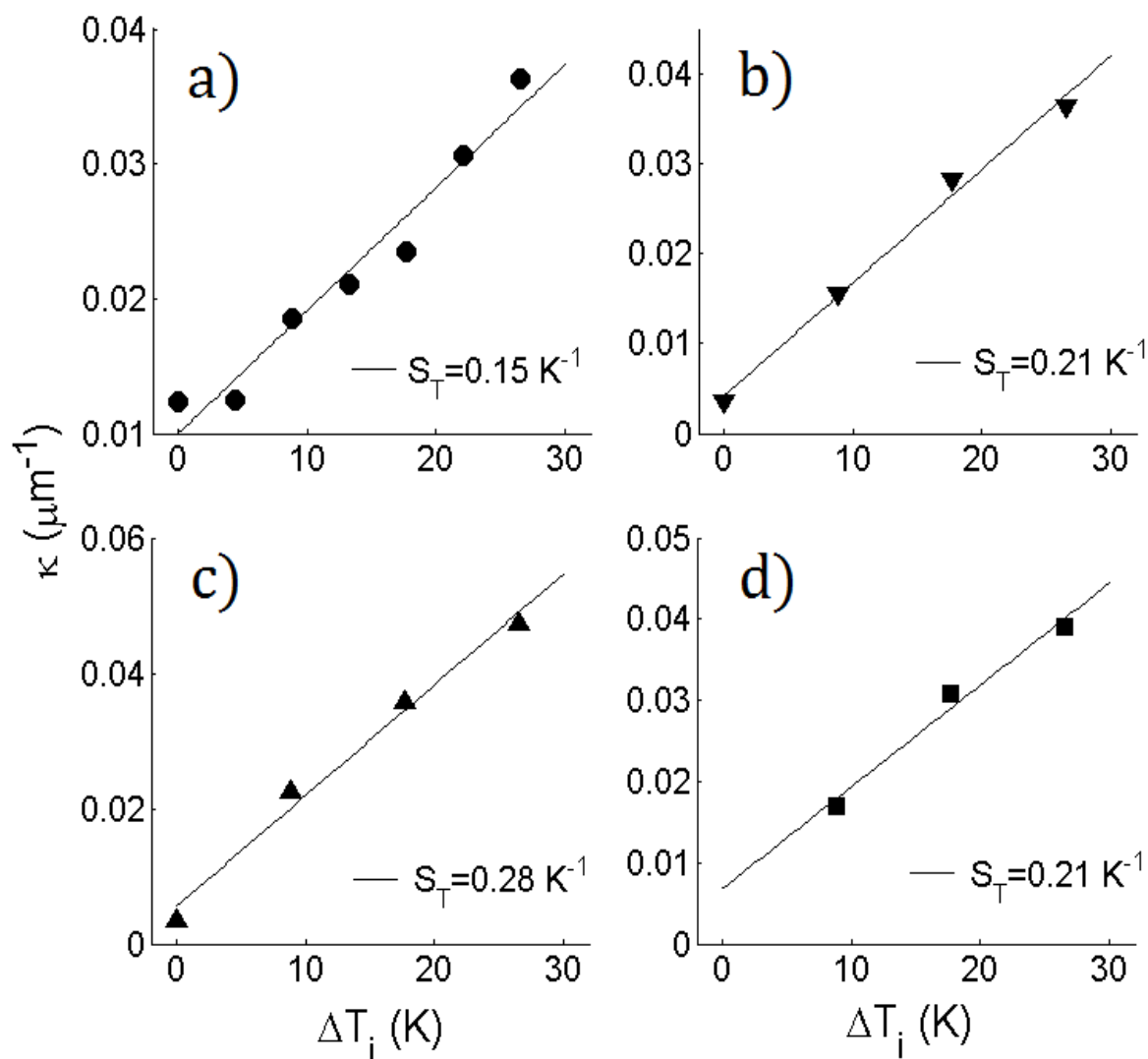


Figure 4.8: Decay parameter κ vs internal temperature difference ΔT_i , for a) PS-STV in DiW, b) PS-PEG-DNA in DiW, c) PS-PEG- N_3 in DiW and d) PS-PEG- N_3 in TE. The values of κ are averages over the last 5 measures at steady-state. The corresponding standard errors and propagated errors on ΔT_i due to an uncertainty in sapphire conductivity are relatively small and therefore not shown.

in DiW	PS-STV	PS-PEG-N ₃	PS-PEG-DNA
S_T/d_h (K ⁻¹ μm ⁻¹)	0.25 ± 0.02	0.63 ± 0.04	0.43 ± 0.03
ζ (mV)	-29.5	-18.9	-30.6

Table 4.2: The errors on S_T/d_h are calculated from the relative sample error of 7%.

be highest for PS-PEG-N₃, which could only be explained by the scaling if ζ and V_T have opposite signs. However, this would still not provide an explanation for the difference in S_T/d_h for PS-STV and PS-PEG-DNA, whose zeta potentials are nearly equal. Therefore, my measurements clearly suggest that surface functionality leads to an additional contribution to S_T that is not accounted for by the aforementioned ζ -model.

4.3 Thermophoretic Relaxation to Steady-State

Although the colloidal steady-state distribution has previously been exploited to determine S_T , very little is known about the relaxation process behind this steady-state. The diffusive time scale τ_D yields a rough estimate for the relaxation time but provides no further insight into the underlying relaxation dynamics. In biological processes however, we are often interested in how a collection of confined particles or molecules relaxes to steady-state under the action of a weak thermodynamic force, the accumulation of biomolecules in out-of-equilibrium pores being an important example [5]. A theoretical model is therefore required that allows a more quantitative description of this collective relaxation. Here, I propose the colloidal centre of mass (CoM) as a natural candidate for this description, defined by

$$Z = \frac{\sum_i z_i P(z_i)}{\sum_i P(z_i)}, \quad (4.10)$$

which, in the continuous limit, can equivalently be written as

$$Z = \int z P_z(z) dz, \quad (4.11)$$

where $P_z(z)$ is the linear probability density in the z -direction, satisfying $\int P_z(z) dz = 1$. From eq. (4.11), we see that the motion of the CoM is related to the evolution of $P_z(z)$, which is governed by the continuity equation for an effectively one-dimensional, closed system in the absence of particle generation

$$\frac{\partial P_z}{\partial t} + \frac{\partial j}{\partial z} = 0. \quad (4.12)$$

The corresponding probability flux j is simply given by

$$j = -D \frac{\partial P_z}{\partial z} + \frac{F}{\xi} P_z, \quad (4.13)$$

where $F = F_g + F_T$ is the total force on a colloid. Due to the temperature dependence of the water viscosity [2], it should be noted that the friction coefficient drops to half its value between 20°C and 50°C whereas the diffusion coefficient doubles in this range. For the sake of simplicity, we shall nonetheless assume that D and ξ can be taken as approximately constant. This is a reasonable assumption for the CoM dynamics as the colloids close to the top surface will be rapidly driven away from that surface by an increasingly large thermophoretic force at higher gradients, so that the majority of the colloids will be located in lower temperature regions during most the relaxation process. With the expression for j given by eq. (4.13), the continuity equation (4.12) can then be rewritten in terms of rescaled variables

$$\frac{\partial P_z}{\partial t'} + \frac{\partial P_z}{\partial z'} - \frac{\partial^2 P_z}{\partial z'^2} = 0, \quad (4.14)$$

where $t' = \kappa^2 D t$ and $z' = \kappa z$. Here, I compare my experimental data to numerical solutions of eq. (4.14), using a standard PDE-solver (MATLAB). By assuming perfectly reflecting boundaries at $z = 0$ and $z = h$, eqs. (4.12) and (4.13) can further be used to derive the following equation of motion for the colloidal CoM (see appendix E):

$$F + \Pi - \xi V_Z = 0, \quad (4.15)$$

where V_Z is the CoM velocity. The term Π has an entropic nature and is given by

$$\Pi = -k_B T (P_z(h) - P_z(0)). \quad (4.16)$$

As $P_z(z', t')$ only has a simple stationary solution at steady-state, there is no straightforward analytical prediction for the time evolution of Π .

Let us now consider the case where the system is at steady-state. The colloidal CoM has reached a stable position ($V_Z = 0$) and the force balance is given by $F + \Pi = 0$. The system is then suddenly subjected to a constant perturbation δF at time $t = 0$, *e.g.* by increasing the temperature gradient. The resulting CoM shift δZ will induce an entropic response $\delta \Pi$ that opposes the external perturbation until a new steady-state is reached. It follows that $\delta \Pi$ acts as a restoring force, satisfying $\delta \Pi(\delta Z = 0) = 0$. To make progress in quantifying the CoM relaxation, I examine the weak perturbation limit by assuming a linear response relation of the form $\delta \Pi \propto \delta Z$. Eq. (4.15) can then be solved analytically, giving:

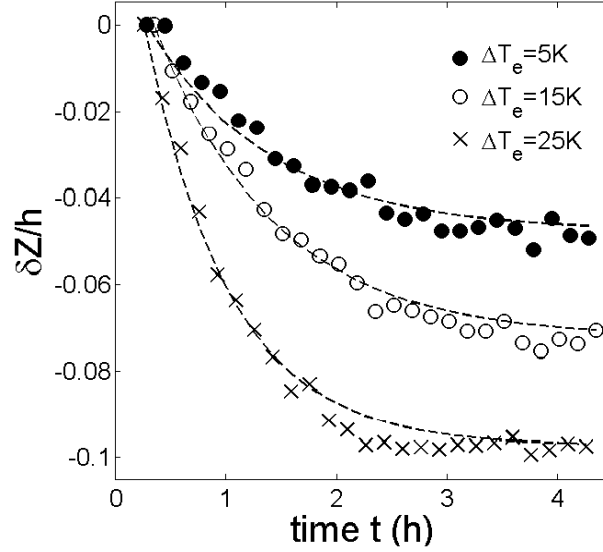


Figure 4.9: Observed time evolution of the CoM shift δZ of PS-STV in DiW, rescaled with respect to the cell height h , for three different values of ΔT_e . The dashed lines are exponential fits from which the values of ω are determined. The time offset at $\delta Z = 0$ is due to the fact that the time origin coincides with the moment when the colloidal concentration is uniform, whereas δZ is defined with respect to the first CoM position measured during the observation.

$$\delta Z(t) = \delta Z_f (1 - \exp(-\omega t)), \quad (4.17)$$

where δZ_f is the final CoM shift over the entire system, in response to the perturbation δF . Following eq. (4.17), I therefore propose that the temporal decay constant ω can be used to quantify the speed of the relaxation to steady-state. In view of eq. (4.15), ω should further satisfy the relation

$$\xi \omega \sim \left| \frac{\delta F}{\delta Z_f} \right|. \quad (4.18)$$

As eq. (4.17) relies on reflecting boundaries, it must be noted that some of my colloids suffered from weak surface absorption to the sapphire windows, in particular PS-STV in DiW. Although the number of absorbed colloids saturates during the relaxation, absorption can temporarily perturb the free evolution of the CoM. Furthermore, the system boundaries have to be excluded from the data analysis due to the previously mentioned reasons, leading to deviations from eq. (4.18) when the CoM is only tracked over a limited bulk range of the system. Nonetheless, the CoM relaxation of PS-STV in DiW is found to be well fitted by

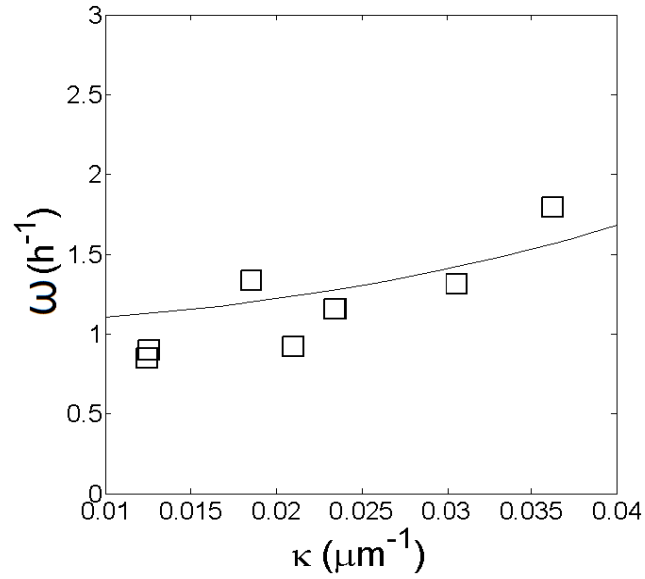


Figure 4.10: Relaxation speed ω vs decay parameter κ for PS-STV in DiW (squares). The solid line shows the trend of $\omega(\kappa)$ obtained from numerical solutions of eq. (4.14), based on reflecting boundaries and using the value of D given for PS-STV in Table 4.1.

an exponential decay. For this system, each relaxation was studied in a separate experiment where an initially uniform distribution of colloids was subjected to a thermophoretic force F_T fixed by the externally applied temperature difference ΔT_e . Three of these relaxations are displayed in fig. 4.9, together with their exponential fits from which the relaxation speed ω is determined. In fig. 4.10, these values of ω are plotted against the corresponding values of κ , which are directly related to the magnitude of F_T via eq. (4.6). It can be seen that ω tends to increase with κ , corresponding to shorter relaxation times for stronger thermophoretic forces. The same conclusion is drawn from the trend of $\omega(\kappa)$ as obtained from numerical solutions of eq. (4.14). Although assuming reflecting boundaries, the numerical curve (full line) displays a good agreement with the experimental data. The observed trend of $\omega(\kappa)$ can clearly not be explained by the diffusive time scale τ_D , which just gives $\omega = \tau_D^{-1} \propto D$, with no allowance for a dependence on κ .

Fig. (4.11) shows the relaxation of PS-PEG-N₃ in TE, for which no surface absorption was observed. The CoM shifts are again very well fitted by my exponential model (dashed lines). This system was measured in a single experiment, so that the initial concentration was uniform for the relaxation at $\Delta T_e = 10$ K and subsequently fixed by the previously reached steady-states for the relaxations at $\Delta T_e = 20$ K and $\Delta T_e = 30$ K. For each relaxation, the perturbation δF is thus fixed by the difference between the values of κ at the final and initial

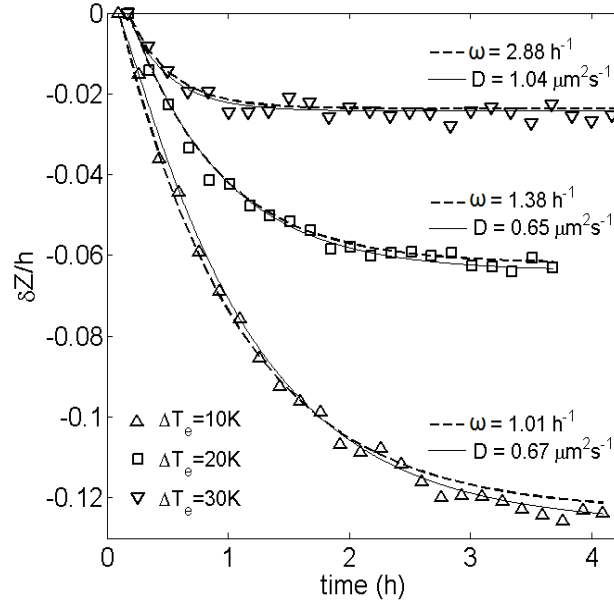


Figure 4.11: Observed time evolution of δZ for PS-PEG- N_3 in TE (symbols), for varying external temperature differences ΔT_e . Full lines correspond to numerical solutions of eq. (4.14). The legend above each curve shows the value of ω obtained from the exponential fit (dashed line) and the optimal value of D used for fitting of the numerical solution.

steady-state. In units of κ , these are given by $\delta F = 0.017 \mu\text{m}^{-1}$, $\delta F = 0.014 \mu\text{m}^{-1}$ and $\delta F = 0.011 \mu\text{m}^{-1}$ in order of increasing ΔT_e . The corresponding values of ω are reported in fig. 4.11 and indicate that the relaxation speed increased rapidly with the incremental increase of ΔT_e . As the magnitude of δF barely changed from one relaxation to the next, the observed increase of ω with ΔT_e in this experiment is mainly related to the initial condition, showing that the CoM relaxes faster when the distance to steady-state δZ_f is reduced.

Due to the absence of absorption, the CoM shift of PS-PEG- N_3 can be directly compared to numerical solutions of eq. (4.14). For this purpose, the solutions (full lines in fig. 4.11) were obtained by using the diffusion coefficient D as a fitting parameter to reproduce the measured value of ω most accurately. This is achieved by extracting D from a curve of ω vs D based on eq. (4.14), for each perturbation δF and corresponding initial condition. These curves are shown in fig. 4.12 and display a linear relationship $\omega \propto D$ for each relaxation. Interestingly, the thus determined optimal value of D is always smaller than the value of $1.11 \mu\text{m}^2\text{s}^{-1}$ for PS-PEG- N_3 obtained from the Einstein relation, the difference being particularly large for the relaxations at $\Delta T_e = 10\text{K}$ and $\Delta T_e = 20\text{K}$, where the optimal value is roughly $0.66 \mu\text{m}^2\text{s}^{-1}$. A possible reason for this discrepancy might be the existence of hydrodynamic effects such as temporary convective flows, giving rise to an additional time-

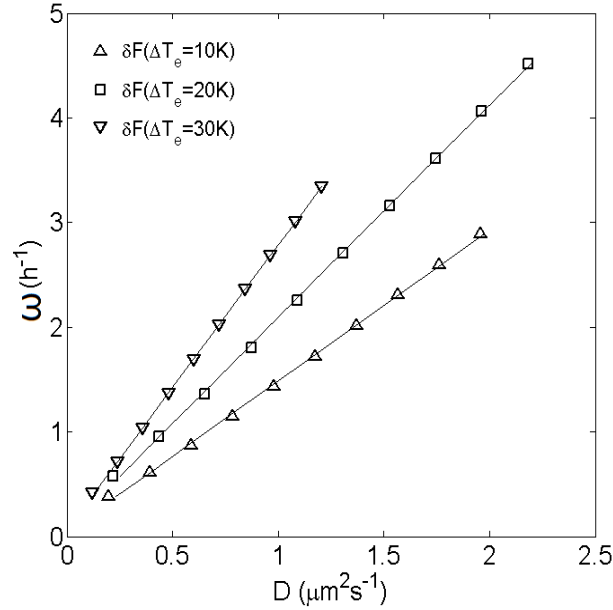


Figure 4.12: Numerical simulation of ω vs D (symbols) based on eq. (4.14), for the given perturbations and initial conditions of PS-PEG- N_3 in TE. The full lines are best linear fits.

dependent term in eq. (4.13) that slows down the relaxation and disappears at steady-state. However, fig. 4.13 suggests that these effects do not influence the z' -dependence of eq. (4.14), as the observed shape of the concentration profile $P(z', t')$ of PS-PEG- N_3 is always well fitted by a corresponding numerical solution.

4.4 Conclusion

I have introduced a measurement technique for thermophoresis that is based on observing the change of the colloidal steady-state concentration profile with the applied temperature gradient. This method automatically eliminates the gravitational pull and is free of any other external influences, allowing a clean and direct measurement of the Soret coefficient. My measurements show that the Soret coefficient is rather insensitive to temperature for charged PS particles in aqueous suspensions. Further, the measured thermophoretic force varies linearly with the temperature gradient, supporting the linear-response assumption of the theory of non-equilibrium thermodynamics. The colloids with the weakest zeta potential exhibit the strongest thermophoretic effect, suggesting that the Soret coefficient has a more intricate dependence on surface functionality than predicted by existing theoretical models. I have also investigated the relaxation to steady-state by studying the CoM motion of the colloids. The observed CoM motion is in agreement with a theoretical model that predicts an

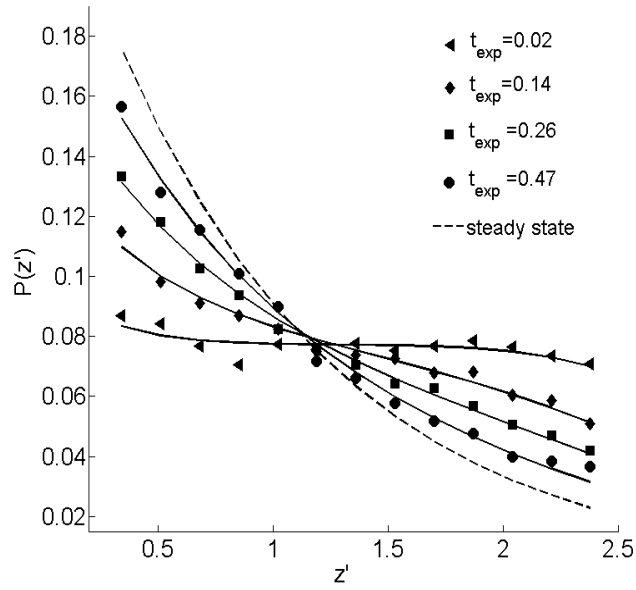


Figure 4.13: a) Probability distribution $P(z')$ vs rescaled altitude z' for PS-PEG- N_3 in TE (symbols), at different instants t_{exp} during the relaxation to steady-state for $\Delta T_e = 10$ K. The full lines are best fits obtained from eq. (4.14), based on least square fitting. t_{exp} is rescaled w.r.t the total relaxation time.

exponential decay to steady-state. The decay speed ω has been found to depend on both the initial condition and the thermophoretic force, with a tendency to increase with the magnitude of the force. This insight cannot be gained from an estimate based on the diffusive time scale, which only predicts a linear dependence on the diffusion coefficient.

Chapter 5

General Conclusion and Outlook

As I have shown in this work, colloidal thermophoresis is an exciting and yet intricate physical phenomenon that clearly deserves to be the subject of current research.

From a theoretical point of view this is evidenced by the fact that, to my knowledge, the theoretical approach presented in chapter 2 represents the first complete description of thermophoresis within the framework of non-equilibrium thermodynamics. A likely reason why this has not been achieved before is that the application of NET requires a very careful set of assumptions for the evaluation of transport coefficients, which in colloidal suspensions derives from the dynamic length and time scale separation between the colloid and the fluid. Correctly identifying these assumptions is a challenging task in soft matter physics as they strongly depend on the physical properties of the considered system. This has lead many to avoid NET and instead base their approaches on seemingly intuitive arguments adopted from other transport phenomena at uniform temperature, such as sedimentation or diffusion. I have shown that such approaches are incomplete as thermophoresis has a hydrodynamic character that requires a full treatment within the framework of NET. Most importantly, the application of Onsager's reciprocal relations has not only allowed me to determine the transport coefficients for thermophoresis, but has also shown that these coefficients account for any colloidal transport phenomenon, including diffusiophoresis, electrophoresis or sedimentation. My theoretical description therefore paves the way to a general and thorough understanding of the physical mechanisms behind colloidal motion. Chapter 3 was dedicated to simulations of thermophoresis based on multi-particle collision dynamics, providing a means to test my theoretical predictions and explore the range of validity of the underlying assumptions. A valuable insight gained from these simulations is that strong temperature variations and fluid flows can perturb the local equilibrium structure of the interfacial layer around a colloid, suggesting that the assumption of interfacial thermodynamic equilibrium should be questioned when studying thermophoresis. As mentioned in section 1.2,

the Soret coefficients of micron-sized colloids are usually found to be of the order $\sim 1 \text{ K}^{-1}$. As applied temperature gradients do not exceed $\sim 1 \text{ K}\mu\text{m}^{-1}$, the relative temperature variation $R|\nabla T|/T$ across the colloids is indeed negligible. Given that the solvent is non-ideal in real experiments, the more general form of the introduced Péclet number $Pe = |\gamma u_{\text{ad}}/\nabla\phi|$ should be used to quantify advective effects in dilute colloidal suspensions. An estimate of u_{ad} is provided by $u_{\text{ad}} \sim |\mathbf{F}_T/\xi|$ based on momentum conservation and the ratio between the friction coefficients of the fluid and colloid $r_s = \gamma/\xi$ is mainly set by the ratio of the corresponding sizes, giving $r_s \sim R/R_s$ where R_s is the radius of a fluid particle. Using $\nabla\phi \sim \varepsilon/\lambda$ and assuming that $\varepsilon \sim k_B T$, we obtain the criterion $|S_T \nabla T| \ll R/(\lambda R_s)$, which is indeed satisfied for typical values of $|S_T \nabla T| \sim 1 \mu\text{m}^{-1}$ in the colloidal regime where both R_s and λ are much smaller than the radius of a colloid. As a result, advective distortions should be negligible in most colloidal suspensions, but are expected to be more pronounced in molecular mixtures where Soret coefficients tend to be higher and where particle sizes and interaction ranges are of the same order of magnitude.

However, applying the theoretical predictions to more complex experimental systems is less trivial, as it is in practise often impossible to precisely define the interfacial interactions and hydrodynamic boundary conditions at the colloidal surface, or to exactly pin down all contributions related to the fluid steady-state. Some of these difficulties are encountered in my experiments presented in chapter 4, where the measured Soret coefficient of functionalised colloids in aqueous electrolyte solutions is influenced by different molecular surface groups in a way that is hard to predict theoretically. On a positive note, the sensitivity of the Soret coefficient to surface functionality suggests that a more efficient separation of different species of particles could be achieved with functionalisation. In analogy to a recently developed technique for determining binding affinities of proteins in biological systems [87, 47, 79], thermophoresis could also be used to quantify the surface coverage of functionalised colloids in reversible adsorption processes. As such techniques often rely on the observation of the colloidal distribution at steady-state, I have studied the corresponding relaxation dynamics, showing that the relaxation speed depends on both the diffusion coefficient and the applied thermophoretic force.

Although I have managed to answer many of the unresolved questions that I was confronted with at the beginning of my PhD, my work has also raised some new questions that offer a fruitful ground for future research. For instance, one could try to find a more quantitative link between fluid advection and the resulting distortion of the interfacial layer, to understand more precisely how the observed deviations depend on the Péclet number. As my simulations considered a stationary colloid, these advective distortions could instead be analysed in the case where the colloid is freely moving. Another open question concerns the

effect of local distortions in the gradient due to fluid advection or conduction through the colloid and its layer. It is currently rather unclear to what extent a locally modified gradient violates the assumption of ITE upon which my theoretical framework is based. After all, it must be remembered that the condition of ITE sets the length scale over which local thermodynamic equilibrium must hold in order to treat the colloids as a thermodynamic component within the framework of NET, thus allowing the use of the Onsager reciprocal relations. Therefore, it would be very interesting to examine whether the motion of self-phoretic (Janus) particles can still be described with my theoretical approach, as these particles create strong, locally varying gradients around their surfaces.

Appendix

A. Evaluation of the Orientational Average over the Fluid Flow

Here, I evaluate the orientational average $\langle \mathbf{u}_s \hat{\mathbf{y}} \rangle$, defined by

$$\langle \mathbf{u}_s \hat{\mathbf{y}} \rangle = \frac{1}{2} \int_0^\pi u_y(r, \theta) \sin \theta d\theta, \quad (5.1)$$

where $u_y(r, \theta)$ is the component of the flow velocity along the direction $\hat{\mathbf{y}}$ of the bulk flow. The solution for the fluid flow velocity \mathbf{u}_s in the spherical basis $(\hat{\mathbf{r}}, \hat{\boldsymbol{\theta}})$ is given by

$$u_r = u_\infty \cos \theta \left[1 - 2 \left(\frac{3}{4} - a \right) \frac{R}{r} + 2 \left(\frac{1}{4} - a \right) \left(\frac{R}{r} \right)^3 \right] \quad (5.2)$$

$$u_\theta = -u_\infty \sin \theta \left[1 - \left(\frac{3}{4} - a \right) \frac{R}{r} - \left(\frac{1}{4} - a \right) \left(\frac{R}{r} \right)^3 \right], \quad (5.3)$$

where the parameter a takes the value $a = 0$ for stick and $a = 1/4$ for slip. The component u_y can hence be computed:

$$u_y = u_r \cos \theta - u_\theta \sin \theta \quad (5.4)$$

$$= u_\infty \cos^2 \theta \left[1 - 2 \left(\frac{3}{4} - a \right) \frac{R}{r} + 2 \left(\frac{1}{4} - a \right) \left(\frac{R}{r} \right)^3 \right] \quad (5.5)$$

$$+ u_\infty \sin^2 \theta \left[1 - \left(\frac{3}{4} - a \right) \frac{R}{r} - \left(\frac{1}{4} - a \right) \left(\frac{R}{r} \right)^3 \right]. \quad (5.6)$$

Using the trigonometric identity $\cos^2 \theta = 1 - \sin^2 \theta$, this can be rearranged into

$$u_y = u_\infty \left[1 - 2 \left(\frac{3}{4} - a \right) \frac{R}{r} + 2 \left(\frac{1}{4} - a \right) \left(\frac{R}{r} \right)^3 + \sin^2 \theta \left(\left(\frac{3}{4} - a \right) \frac{R}{r} - 3 \left(\frac{1}{4} - a \right) \left(\frac{R}{r} \right)^3 \right) \right]. \quad (5.7)$$

Knowing that the orientational average over $\sin^2 \theta$ takes the value

$$\frac{1}{2} \int_0^\pi (\sin^2 \theta) \sin \theta d\theta = \frac{1}{2} \int_0^\pi \sin^3 \theta d\theta = \frac{2}{3}, \quad (5.8)$$

the orientational average $\langle \mathbf{u}_s \hat{\mathbf{y}} \rangle$ takes the form

$$\langle \mathbf{u}_s \hat{\mathbf{y}} \rangle = u_\infty \left[1 - \left(1 - \frac{4}{3} a \right) \frac{R}{r} \right] = \begin{cases} u_\infty \left(1 - \frac{R}{r} \right) & \text{for stick} \\ u_\infty \left(1 - \frac{2}{3} \frac{R}{r} \right) & \text{for slip.} \end{cases}$$

I have thus recovered the result used in eq. (2.52) to obtain eq. (2.56), which allows the determination of the interfacial transport coefficient X_{cs} .

B. The Partial Enthalpy of a Point-Like Component

We consider a component k of point-like particles that do not interact with each other. The component is embedded in a solvent and the particles are therefore surrounded by solvation layers due to the specific interaction with the solvent molecules. In this case, the chemical potential of component k just comprises an ideal part μ_{id} and an interfacial part μ_{ks} , such that $\mu_k = \mu_{id} + \mu_{ks}$. The ideal contribution μ_{id} is given by [12]

$$\mu_{id} = k_B T \ln n_k^b - \frac{3}{2} k_B T \ln T + K, \quad (5.9)$$

where K is a constant. As the solvent is incompressible, there is no interfacial excess of solvent molecules and the Gibbs adsorption equation for the solvation layer reduces to

$$-d\mu_{ks} = -H_\phi^k \frac{dT}{T}, \quad (5.10)$$

where $H_\phi^k = TS_\phi^k$ is the enthalpy of solvation. Based on eq. (2.4), the partial molar enthalpy of component k can then be computed:

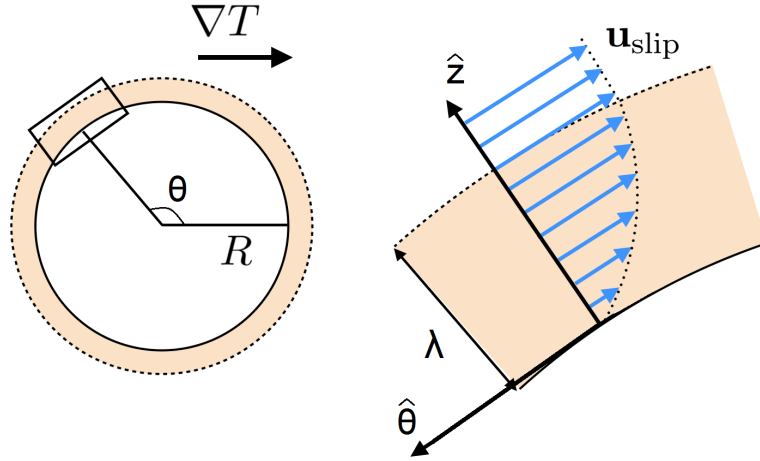


Figure 5.1: Schematic diagram of the boundary layer approximation. The blue arrows show the interfacial fluid flow as observed in the rest frame of the colloid, reaching a maximal slip velocity \mathbf{u}_{slip} at the boundary of the interfacial layer.

$$\bar{H}_k = -T^2 \frac{\partial}{\partial T} \left(\frac{\mu_k}{T} \right)_{P,n_j} \quad (5.11)$$

$$= -T^2 \frac{\partial}{\partial T} \left(\frac{\mu_{id}}{T} \right)_{P,n_j} - T^2 \frac{\partial}{\partial T} \left(\frac{\mu_{ks}}{T} \right)_{P,n_j} \quad (5.12)$$

$$= \frac{3}{2} k_B T + \left(T S_\phi^k + \mu_{ks} \right) \quad (5.13)$$

$$= \frac{3}{2} k_B T + \bar{H}_k^0, \quad (5.14)$$

where $\bar{H}_k^0 = T S_\phi^k + \mu_{ks}$ is the contribution to \bar{H}_k stemming from the solvation layer. For ions in water, \bar{H}_k^0 hence corresponds to the partial molar enthalpy due to hydration.

C. Würger's derivation of \mathbf{F}_{cs} in the boundary layer approximation

In my derivation of \mathbf{F}_{cs} , I used Onsager's reciprocal relations by considering the fluid flow induced by a colloid moving through a homogeneous fluid at uniform temperature. However, Würger's derivation of \mathbf{F}_{cs} involves the interfacial fluid flow induced in the rest frame of the colloid when a temperature gradient is applied across the interfacial layer [33, 90]. Here, the direction of the temperature gradient is specified by the unit vector $\hat{\mathbf{y}}$. In the boundary layer

approximation, the colloidal surface is locally treated as a flat wall and the corresponding flow is parallel to the surface. As shown in fig. 5.1, the hydrodynamic problem can be described in the spherical basis $(\hat{\mathbf{r}}, \hat{\boldsymbol{\theta}})$ by using the coordinates $z = r - R$ and θ , where θ is the angle between $\hat{\mathbf{y}}$ and $\hat{\mathbf{r}}$. For simplicity, I will assume that the thermal conductivities of the colloid and the fluid are the same.

Let us write the interfacial force density as $\vec{\mathcal{F}}_\phi = \mathcal{F}_\phi \hat{\mathbf{y}}$ and let $\mathcal{F}_\theta = -\mathcal{F}_\phi \sin \theta$ be the component of $\vec{\mathcal{F}}_\phi$ parallel to the surface. The Navier-Stokes equation for the interfacial flow can then be written as

$$\mathcal{F}_\theta + \eta \frac{\partial^2 u_\theta}{\partial z^2} = 0. \quad (5.15)$$

Knowing that the flow reaches a maximal slip velocity $\mathbf{u}_{\text{slip}} = u_{\text{slip}} \hat{\boldsymbol{\theta}}$ at the boundary of the interfacial layer ($z \rightarrow \infty$), a first integration from the boundary into the layer yields

$$\left[\frac{\partial u_\theta}{\partial z} \right]_\infty^z = \frac{\partial u_\theta}{\partial z} = \int_z^\infty \frac{\mathcal{F}_\theta}{\eta} dz'. \quad (5.16)$$

By applying a stick boundary condition at the surface ($u_\theta = 0$ at $z = 0$), a second integration from the surface ($z = 0$) to the boundary gives

$$[u_\theta]_0^\infty = u_{\text{slip}} = \int_0^\infty \left(\int_z^\infty \frac{\mathcal{F}_\theta^{cs}}{\eta} dz' \right) dz'', \quad (5.17)$$

which, with integration by parts, can be simplified to

$$u_{\text{slip}} = \left[z \int_z^\infty \frac{\mathcal{F}_\theta}{\eta} dz' \right]_0^\infty + \int_0^\infty z \frac{\mathcal{F}_\theta}{\eta} dz = -\sin \theta \int_0^\infty z \frac{\mathcal{F}_\phi}{\eta} dz. \quad (5.18)$$

Due to momentum conservation, the reciprocal theorem for the Stokes flow problem can be applied outside the boundary layer [4, 9], showing that the colloid moves along the temperature gradient with a steady-state velocity $\mathbf{v} = v \hat{\mathbf{y}} = -\langle \mathbf{u}_{\text{slip}} \hat{\mathbf{y}} \rangle \hat{\mathbf{y}}$, where the orientational average $\langle \mathbf{u}_{\text{slip}} \hat{\mathbf{y}} \rangle$ is given by

$$\langle \mathbf{u}_{\text{slip}} \hat{\mathbf{y}} \rangle = \frac{1}{2} \int_0^\pi (\mathbf{u}_{\text{slip}} \hat{\mathbf{y}}) \sin \theta d\theta = \frac{1}{2} \int_0^\infty z \frac{\mathcal{F}_\phi}{\eta} dz \int_0^\pi \sin^3 \theta d\theta = \frac{2}{3} \int_0^\infty z \frac{\mathcal{F}_\phi}{\eta} dz \quad (5.19)$$

The interfacial force \mathbf{F}_{cs} is simply related to the velocity \mathbf{v} via $\mathbf{F}_{cs} = \xi \mathbf{v}$, where the friction coefficient takes the value $\xi = 6\pi\eta R$ for a stick boundary. Assuming that the viscosity of the fluid is constant, it follows that

$$\mathbf{F}_{cs} = -4\pi R \int_0^\infty z \vec{\mathcal{F}}_\phi(z) dz. \quad (5.20)$$

Eq. (5.20) constitutes Würger's final result, which is in agreement with my expression for a stick boundary given in eq. (2.63).

D. External and Internal Temperature Difference

Due to the finite thermal conductivities of the sapphire windows, the externally applied temperature difference ΔT_e will not be equal to the internal temperature difference ΔT_i inside the cell. This system is made of an aqueous colloidal suspension sandwiched between two sapphire windows. As the suspension is very dilute, its thermal conductivity is simply equal to that of water. At thermal steady-state, the heat current q through the system Sapphire-Water-Sapphire (sws) must be the same as the current through each element. The thermal conductance is defined as

$$C = \frac{\sigma S}{d}, \quad (5.21)$$

where σ is the thermal conductivity of the considered element, S is the surface area of the element and d is its thickness. For the heat current through the entire system (sws), we thus have

$$q = C_{sws} \Delta T_e. \quad (5.22)$$

Similarly, the heat current through the suspension reads

$$q_w = C_w \Delta T_i. \quad (5.23)$$

Using the relation $q = q_w$, the internal temperature difference can hence be written as

$$\Delta T_i = \frac{C_{sws}}{C_w} \Delta T_e. \quad (5.24)$$

Given that the suspension is sandwiched between the sapphire windows, these three conducting elements are in series, so that we have

$$\frac{1}{C_{sws}} = \frac{1}{C_w} + \frac{2}{C_s}, \quad (5.25)$$

which can be rearranged into

$$\frac{C_{sws}}{C_w} = \frac{1}{1 + 2\frac{C_w}{C_s}} = \frac{1}{1 + 2\frac{\sigma_w h_s}{\sigma_s h}} \quad (5.26)$$

Substituting eq. (5.26) into eq. (5.24) then allows the recovery of the expression for ΔT ; used in section 4.2.

E. Equation of Motion of the Colloidal CoM

As stated in section (4.3), the 1D probability flux j of colloids takes the form

$$j = -D \frac{\partial P_z}{\partial z} + \frac{F}{\xi} P_z. \quad (5.27)$$

The derivation of the equation of motion for the colloidal CoM starts from the definition of the CoM velocity $V_Z = dZ/dt$, where Z is given by

$$Z = \int z P_z(z) dz. \quad (5.28)$$

Using the continuity equation, the CoM velocity can hence be written as:

$$V_Z = \int z \frac{\partial P_z}{\partial t} dz = - \int z \frac{\partial j(z)}{\partial z} dz. \quad (5.29)$$

With reflecting boundaries ($j(z=0) = 0$ and $j(z=h) = 0$), integration by parts then directly yields

$$V_Z = \int j(z) dz. \quad (5.30)$$

Assuming that D , ξ and F are approximately uniform inside the system, substituting eq. (5.27) for j into eq. (5.30) gives

$$V_Z = -D \int \frac{\partial P_z}{\partial z} dz + \frac{F}{\xi} \int P_z dz = -D (P_z(h) - P_z(0)) + \frac{F}{\xi}. \quad (5.31)$$

Multiplying eq. (5.31) by ξ , using $\xi D = k_B T$ and rearranging, we obtain the equation of motion of the colloidal CoM

$$F + \Pi - \xi V_Z = 0, \quad (5.32)$$

where $\Pi = -k_B T (P_z(h) - P_z(0))$ is the entropic restoring force.

Bibliography

- [1] Agar, J. N., Mou, C. Y., and Lin, J. L. (1989). Single-ion heat of transport in electrolyte solutions: a hydrodynamic theory. *The Journal of Physical Chemistry*, 93(5):2079–2082.
- [2] Al-Shemmeri, T. (2012). *Engineering fluid mechanics*. Bookboon.
- [3] Allahyarov, E. and Gompper, G. (2002). Mesoscopic solvent simulations: Multiparticle-collision dynamics of three-dimensional flows. *Phys. Rev. E - Stat. Nonlinear, Soft Matter Phys.*, 66(3):1–9.
- [4] Anderson, J. L. (1989). Colloid Transport by Interfacial Forces. *Annual Review of Fluid Mechanics*, 21(1):61–99.
- [5] Baaske, P., Weinert, F. M., Duhr, S., Lemke, K. H., Russell, M. J., and Braun, D. (2007). Extreme accumulation of nucleotides in simulated hydrothermal pore systems. *Proceedings of the National Academy of Sciences of the United States of America*, 104(22):9346–51.
- [6] Barber, R. and Emerson, D. (2000). Analytical solution of low Reynolds number slip flow past a sphere. *Laboratory Technical Report*.
- [7] Batchelor, G. K. (1967). *An Introduction to Fluid Dynamics*. Cambridge University Press.
- [8] Batchelor, G. K. (1976). Brownian diffusion of particles with hydrodynamic interaction. *Journal of Fluid Mechanics*, 74:1.
- [9] Brady, J. F. (2011). Particle motion driven by solute gradients with application to autonomous motion: continuum and colloidal perspectives. *Journal of Fluid Mechanics*, 667:216–259.
- [10] Braibanti, M., Vigolo, D., and Piazza, R. (2008). Does Thermophoretic Mobility Depend on Particle Size? *Physical Review Letters*, 100(10):108303.

- [11] Braun, D. and Libchaber, A. (2002). Trapping of DNA by Thermophoretic Depletion and Convection. *Physical Review Letters*, 89(18):188103.
- [12] Bringuier, E. and Bourdon, A. (2003). Colloid transport in nonuniform temperature. *Physical Review E*, 67(1):011404.
- [13] Burelbach, J., Brückner, D. B., Frenkel, D., and Eiser, E. A Mesoscopic Study of Thermophoretic Forces : Theory and Simulation (in preparation).
- [14] Burelbach, J., Frenkel, D., Pagonabarraga, I., and Eiser, E. A Unified Description of Colloidal Thermophoresis. *European Physical Journal E* (submitted).
- [15] Burelbach, J., Zupkauskas, M., Lamboll, R., Lan, Y., and Eiser, E. (2017). Colloidal Motion under the Action of a Thermophoretic Force. *The Journal of Chemical Physics*, 147(1).
- [16] Chavanis, P. H. (2004). Generalized Fokker-Planck equations and effective thermodynamics. *Physica A: Statistical Mechanics and its Applications*, 340(1-3):57–65.
- [17] Crocker, J. C. and Grier, D. G. (1996). Methods of Digital Video Microscopy for Colloidal Studies. *J. Colloid Interface Sci.*, 179(179):298–310.
- [18] de Groot, S. and Mazur, P. (1969). *Non-equilibrium Thermodynamics*. North-Holland.
- [19] Debye, P. and Hückel, E. (1923). The theory of electrolytes. I. Lowering of freezing point and related phenomena. *Physikalische Zeitschrift*.
- [20] Derjaguin, B., Churaev, N., and Muller, V. (1987). *Surface Forces*. New York.
- [21] Dhont, J. K. G. (2004a). Thermodiffusion of interacting colloids. I. A statistical thermodynamics approach. *The Journal of chemical physics*, 120(3):1632–41.
- [22] Dhont, J. K. G. (2004b). Thermodiffusion of interacting colloids. II. A microscopic approach. *The Journal of chemical physics*, 120(3):1642–53.
- [23] Dhont, J. K. G. and Briels, W. J. (2008). Single-particle thermal diffusion of charged colloids: double-layer theory in a temperature gradient. *The European physical journal. E, Soft matter*, 25(1):61–76.
- [24] Dhont, J. K. G., Wiegand, S., Duhr, S., and Braun, D. (2007). Thermodiffusion of Charged Colloids: Single-Particle Diffusion. *Langmuir*, (11):1674–1683.

- [25] Dominguez, G., Wilkins, G., and Thiemens, M. H. (2011). The Soret effect and isotopic fractionation in high-temperature silicate melts. *Nature*, 473(7345):70–73.
- [26] Duhr, S., Arduini, S., and Braun, D. (2004). Thermophoresis of DNA determined by microfluidic fluorescence. *The European physical journal. E, Soft matter*, 15(3):277–86.
- [27] Duhr, S. and Braun, D. (2006a). Optothermal Molecule Trapping by Opposing Fluid Flow with Thermophoretic Drift. *Physical Review Letters*, 97(3):038103.
- [28] Duhr, S. and Braun, D. (2006b). Thermophoretic Depletion Follows Boltzmann Distribution. *Physical Review Letters*, 96(16):168301.
- [29] Duhr, S. and Braun, D. (2006c). Why molecules move along a temperature gradient. *Proceedings of the National Academy of Sciences of the United States of America*, 2006(15).
- [30] Einstein, A. (1905). Über die von der molekularkinetischen Theorie der Wärme geforderte Bewegung von in ruhenden Flüssigkeiten suspendierten Teilchen. *Ann. d. Phys.*, 322:549–560.
- [31] Ermak, D. L. and McCammon, J. a. (1978). Brownian dynamics with hydrodynamic interactions. *Journal of Physical Chemistry*, 69(1978):1352.
- [32] Fayolle, S., Bickel, T., Le Boiteux, S., and Würger, A. (2005). Thermodiffusion of Charged Micelles. *Physical Review Letters*, 95(20):208301.
- [33] Fayolle, S., Bickel, T., and Würger, A. (2008). Thermophoresis of charged colloidal particles. *Physical Review E - Statistical, Nonlinear, and Soft Matter Physics*, 77(April):1–8.
- [34] Felderhof, B. U. (2003). Diffusion in binary mixtures and osmotic pressure gradient. *The Journal of Chemical Physics*, 118(October):11326.
- [35] Galliero, G. and Montel, F. (2009). Understanding Compositional Grading in Petroleum Reservoirs thanks to Molecular Simulations. *Society of Petroleum Engineers, EUROPEC/EAGE Conference and Exhibition, 8-11 June, Amsterdam, The Netherlands*.
- [36] Galliero, G. and Volz, S. (2008). Thermodiffusion in model nanofluids by molecular dynamics simulations. *J. Chem. Phys.*, 128(6).
- [37] Giddings, J., Shinudu, P. M., and Semenov, S. N. (1995). Thermophoresis of Metal Particles in a Liquid. *Journal of Colloid and Interface Science*, 176:454–458.

- [38] Gompper, G., Ihle, T., Kroll, D. M., and Winkler, R. G. (2009). *Advanced Computer Simulation Approaches for Soft Matter Sciences III*, chapter Multi-Part, pages 1–87. Springer Berlin Heidelberg, Berlin, Heidelberg.
- [39] Helden, L., Eichhorn, R., and Bechinger, C. (2015). Direct measurement of thermophoretic forces. *Soft Matter*, 11:2379–2386.
- [40] Hinch, E. J. and Nitsche, L. C. (1993). Nonlinear drift interactions between fluctuating colloidal particles: oscillatory and stochastic motions. *Journal of Fluid Mechanics*, 256:343.
- [41] Iacopini, S., Rusconi, R., and Piazza, R. (2006). The "macromolecular tourist": universal temperature dependence of thermal diffusion in aqueous colloidal suspensions. *The European physical journal. E, Soft matter*, 19(1):59–67.
- [42] Ihle, T. and Kroll, D. M. (2001). Stochastic rotation dynamics: A Galilean-invariant mesoscopic model for fluid flow. *Phys. Rev. E - Stat. Nonlinear, Soft Matter Phys.*, 63(2 I):0202011–0202014.
- [43] Ihle, T. and Kroll, D. M. (2003a). Stochastic rotation dynamics. I. Formalism, Galilean invariance, and Green-Kubo relations T. *Phys. Rev. E*, 67(6):66705.
- [44] Ihle, T. and Kroll, D. M. (2003b). Stochastic rotation dynamics. {II}. Transport coefficients, numerics, and long-time tails. *Phys. Rev. E*, 67(6):66706.
- [45] Ihle, T., Tüzel, E., and Kroll, D. M. (2005). Equilibrium calculation of transport coefficients for a fluid-particle model. *Phys. Rev. E - Stat. Nonlinear, Soft Matter Phys.*, 72(4).
- [46] Jeon, S. J., Schimpf, M. E., and Nyborg, A. (1997). Compositional effects in the retention of colloids by thermal field-flow fractionation. *Analytical chemistry*, 69(17):3442–50.
- [47] Jerabek-Willemsen, M., Wienken, C. J., Braun, D., Baaske, P., and Duhr, S. (2011). Molecular Interaction Studies Using Microscale Thermophoresis. *ASSAY and Drug Development Technologies*, 9(August):342–353.
- [48] Joshi, D., Bargteil, D., Caciagli, A., Burelbach, J., Xing, Z., Nunes, A. S., Pinto, D. E. P., Araujo, N. a. M., Brujic, J., and Eiser, E. (2016). Kinetic control of the coverage of oil droplets by DNA-functionalized colloids. *Science Advances*, 2(August):e1600881–e1600881.

- [49] Königer, A., Meier, B., and Köhler, W. (2009). Measurement of the Soret, diffusion, and thermal diffusion coefficients of three binary organic benchmark mixtures and of ethanol–water mixtures using a beam deflection technique. *Philosophical Magazine*, 89(July 2017):907–923.
- [50] Lamura, A., Gompper, G., Ihle, T., and Kroll, D. M. (2001). Multi-particle collision dynamics: Flow around a circular and a square cylinder. *Europhys. Lett.*, 56(3):319–325.
- [51] Landau, L. D. and Lifshitz, E. M. (1960). *Electrodynamics of Continuous Media*, volume 8. Pergamon Press.
- [52] Landau, L. D. and Lifshitz, E. M. (1987). Fluid mechanics.
- [53] Ludwig, C. (1856). *Sitzber. Akad. Wiss. Wien, Math.-Nat. Wiss. Kl.* 20, 539.
- [54] Lüsebrink, D. (2011). *Colloidal suspensions in temperature gradients with mesoscopic simulations*. PhD thesis, Universität zu Köln.
- [55] Lüsebrink, D. and Ripoll, M. (2012a). Collective thermodiffusion of colloidal suspensions. *J. Chem. Phys.*, 137(19).
- [56] Lüsebrink, D. and Ripoll, M. (2012b). Temperature inhomogeneities simulated with multiparticle-collision dynamics. *J. Chem. Phys.*, 136(8).
- [57] Lüsebrink, D., Yang, M., and Ripoll, M. (2012). Thermophoresis of colloids by mesoscale simulations. *J. Phys. Condens. Matter*, 24:284132.
- [58] Majee, A. and Würger, A. (2011). Collective thermoelectrophoresis of charged colloids. *Physical Review E*, 83(6):061403.
- [59] Malevanets, A. and Kapral, R. (1999). Mesoscopic model for solvent dynamics. *J. Chem. Phys.*, 110(17):8605.
- [60] Mialdun, A. and Shevtsova, V. (2011). Measurement of the Soret and diffusion coefficients for benchmark binary mixtures by means of digital interferometry. *Journal of Chemical Physics*, 134(2011).
- [61] Mori, A. and Suzuki, Y. (2013). Grand potential formalism of interfacial thermodynamics for critical nucleus. *Natural Science*, 5(5):631–639.
- [62] Morthomas, J. and Würger, A. (2008). Thermoelectric effect of charged colloids in the Huckel limit. *European Physical Journal E*.

- [63] Mortimer, R. G. and Eyring, H. (1980). Elementary transition state theory of the Soret and Dufour effects. *Proceedings of the National Academy of Sciences of the United States of America*, 77(4):1728–1731.
- [64] Murphy, T. and Aguirre, J. (1972). Brownian Motion of N Interacting Particles. I. Extension of the Einstein Diffusion Relation to the N-Particle Case. *The Journal of Chemical Physics*, 57(May 2015):2098–2104.
- [65] Onsager, L. (1931a). Reciprocal Relations in Irreversible Processes. I. *Physical Review Letters*, 37.
- [66] Onsager, L. (1931b). Reciprocal Relations in Irreversible Processes. II. *Physical Review Letters*, 38.
- [67] Padding, J. T. and Louis, a. a. (2006). Hydrodynamic interactions and Brownian forces in colloidal suspensions: Coarse-graining over time and length scales. *Physical Review E - Statistical, Nonlinear, and Soft Matter Physics*, 74:1–29.
- [68] Parola, A. and Piazza, R. (2004). Particle thermophoresis in liquids. *The European physical journal. E, Soft matter*, 15(3):255–63.
- [69] Piazza, R. (2003). Thermal diffusion in ionic micellar solutions. *Philosophical Magazine*, 83(17-18):2067–2085.
- [70] Piazza, R. and Guarino, A. (2002). Soret Effect in Interacting Micellar Solutions. *Physical Review Letters*, 88(20):208302.
- [71] Piazza, R. and Parola, A. (2008). Thermophoresis in colloidal suspensions. *Journal of Physics: Condensed Matter*, 20(15):153102.
- [72] Putnam, S. A. and Cahill, D. G. (2005). Transport of nanoscale latex spheres in a temperature gradient. *Langmuir : the ACS journal of surfaces and colloids*, 21(12):5317–23.
- [73] Reichl, M. (2014). Ionic Thermophoresis and Its Application in Living Cells.
- [74] Ripoll, M., Mussawisade, K., Winkler, R. G., and Gompper, G. (2005). Dynamic regimes of fluids simulated by multiparticle-collision dynamics. *Phys. Rev. E - Stat. Nonlinear, Soft Matter Phys.*, 72(1):1–14.

- [75] Rubí, J. and Mazur, P. (1998). Simultaneous Brownian motion of N particles in a temperature gradient. *Physica A: Statistical Mechanics and its Applications*, 250:253–264.
- [76] Ruckenstein, E. (1981). Can phoretic motions be treated as interfacial tension gradient driven phenomena? *Journal of Colloid and Interface Science*, 83(1):77–81.
- [77] Rusconi, R., Isa, L., and Piazza, R. (2004). Thermal-lensing measurement of particle thermophoresis in aqueous dispersions. *Journal of the Optical Society of America B*, 21(3):605.
- [78] Schimpf, M. E. and Giddings, J. C. (1987). Characterization of Thermal Diffusion in Polymer Solutions by Thermal Field-Flow Fractionation: Effects of Molecular Weight and Branching. *Macromolecules*, pages 1561–1563.
- [79] Seidel, S. a. I., Wienken, C. J., Geissler, S., Jerabek-Willemsen, M., Duhr, S., Reiter, A., Trauner, D., Braun, D., and Baaske, P. (2012). Label-free microscale thermophoresis discriminates sites and affinity of protein-ligand binding. *Angewandte Chemie - International Edition*, 51:10656–10659.
- [80] Shendruk, T. (2014). *Theoretical and Computational Studies of Hydrodynamics-based Separation of Particles and Polymers in Microfluidic Channels*. PhD thesis, University of Ottawa.
- [81] Slater, G. W., Holm, C., Chubynsky, M. V., de Haan, H. W., Dubé, A., Grass, K., Hickey, O. A., Kingsburry, C., Sean, D., Shendruk, T. N., and Zhan, L. (2009). Modeling the separation of macromolecules: A review of current computer simulation methods. *Electrophoresis*, 30(5):792–818.
- [82] Soret, C. (1879). *Arch. Sci. Phys. Nat. Genève* 2, 48.
- [83] Syshchyk, O., Afanasenkau, D., Wang, Z., Kriegs, H., Buitenhuis, J., and Wiegand, S. (2016). Influence of temperature and charge effects on thermophoresis of polystyrene beads. *European Physical Journal E*, 39.
- [84] Tüzel, E., Strauss, M., Ihle, T., and Kroll, D. M. (2003). Transport coefficients for stochastic rotation dynamics in three dimensions. *Phys. Rev. E. Stat. Nonlin. Soft Matter Phys.*, 68(3 Pt 2):036701.
- [85] van Roij, R., Dijkstra, M., and Hansen, J.-P. (1999). Phase diagram of charge-stabilized colloidal suspensions: van der Waals instability without attractive forces. *Physical Review E*, 59(2):2010–2025.

- [86] Vladkov, M. and Barrat, J.-L. (2006). Modeling Transient Absorption and Thermal Conductivity in a Simple Nanofluid. *Nano Lett.*, 6(6):1224–1228.
- [87] Wienken, C. J., Baaske, P., Rothbauer, U., Braun, D., and Duhr, S. (2010). Protein-binding assays in biological liquids using microscale thermophoresis. *Nature communications*, 1(7):100.
- [88] Würger, A. (2006). Heat capacity-driven inverse Soret effect of colloidal nanoparticles. *Europhysics Letters (EPL)*, 74(4):658–664.
- [89] Würger, A. (2009). Temperature dependence of the Soret motion in colloids. *Langmuir*, 25(32):6696–6701.
- [90] Würger, A. (2010). Thermal non-equilibrium transport in colloids. *Reports on Progress in Physics*, 73(12):126601.
- [91] Würger, A. (2013). Is Soret equilibrium a non-equilibrium effect? *Comptes Rendus - Mecanique*, 341(4-5):438–448.
- [92] Würger, A. (2014). Do thermal diffusion and Dufour coefficients satisfy Onsager's reciprocity relation? *European Physical Journal E*, 37(10):96.
- [93] Würger, A. (2014). Thermodiffusion in binary liquids: the role of irreversibility. *Journal of Physics: Condensed matter*, 26:035105.
- [94] Yang, M. and Ripoll, M. (2013). Thermophoretically induced flow field around a colloidal particle. *Soft Matter*, 9:4661–4671.
- [95] Yang, M., Wysocki, A., and Ripoll, M. (2014). Hydrodynamic simulations of self-phoretic microswimmers. *Soft Matter*, 10:6208–18.
- [96] Zhang, K. J., Briggs, M. E., Gammon, R. W., Sengers, J. V., and Douglas, J. F. (1999). Thermal and mass diffusion in a semidilute good solvent-polymer solution. *The Journal of Chemical Physics*, 111(5):2270.
- [97] Zupkauskas, M., Lan, Y., Joshi, D., Ruff, Z., and Eiser, E. (2017, accepted). Optically Transparent Dense Colloidal Gels. *Chem. Sci.*